The Milky Way in SDSS and in N–body Models

Sarah R. Loebman

A dissertation submitted in partial fulfillment of the
requirements for the degree of

Doctor of Philosophy

University of Washington

2013

Reading Committee:

Željko Ivezić, Chair

Thomas Quinn

Victor Debattista

Program Authorized to Offer Degree:
Astronomy

University of Washington

Abstract

The Milky Way in SDSS and in N–body Models

Sarah R. Loebman

Chair of the Supervisory Committee:
Professor Željko Ivezić
Astronomy

In this thesis, I present a comparison between recent Sloan Digital Sky Survey (SDSS) Galactic studies and N–body simulations to aid in the interpretation of observed structural features. I investigate the origin of the Galactic thin/thick disk system and the contents of the Galactic halo by drawing comparisons to two high resolution simulations produced using GASOLINE (Wadsley et al., 2004). My aim is twofold: (1) to assess the plausibility of radial migration as a main driver for shaping the thick disk, and (2) to evaluate via Jeans equations properties of the Galactic potential within the SDSS volume.

I arrive as several key findings:

- Radial migration can produce on a global scale a physically reasonable thin/thick disk system in an N–body simulation.

- Secular evolution via radial migration could be the source of spatial, chemical and kinematic disk trends observed in the solar cylinder by SDSS.

- Jeans equations can meaningfully recover mean accelerations from a non steady-state, non axisymmetric cosmologically derived N–body simulation.

- The morphology of the acceleration maps generated using Jeans equations applied to SDSS data is consistent with the presence of dark matter and inconsistent with a baryon only model of the Milky Way.

- An analytic technique utilizing Jeans equations can meaningfully recover an N–body simulation's mean dark matter axis ratio.

- The same analytic technique applied to SDSS Galactic halo data indicates the Milky Way dark matter axis ratio within the SDSS volume is $q_{DM} = 0.47 \pm 0.14$.

Breakthroughs such as these were enabled by recent rapid progress in both observational surveys and simulation science. This thesis demonstrates the emergent and informative value of direct comparison between the two.

TABLE OF CONTENTS

Page

LIST OF FIGURES

LIST OF TABLES

ACKNOWLEDGMENTS

The author wishes to express sincere appreciation to the University of Washington Astronomy Department.

DEDICATION

To my family, especially Rose Autumn Bayne: you make it all worthwhile.

Chapter 1

INTRODUCTION

The historical pursuit of the natural sciences has largely been aimed at classifying and categorizing objects with common morphological features (Linnaeus, 1735); whether it be birds with similar beak shapes or stars of a like color, we group objects by commonality in appearance first and analyze second. The underlying motivation for this exercise is the premise that the appearance or structure of an object can be used to constrain what it is composed of and how it formed. And the ubiquity of a given type of object or structure in the universe can then constrain commonality of a given evolutionary path.

In the case of complicated objects, such as the Milky Way (MW), we simplify the investigation of its content, origin and evolution by breaking down its appearance into constituent structural parts. Through the study of individual components, we narrow the parameter space of possible evolutionary paths the entire MW could have traversed. Our understanding and appreciation of any given structural component is then limited by the quality, depth and scope of our observational data.

The goal of this thesis is to leverage unprecedented observations of the MW structure to constrain the origins and content of that structure. To aid in this analysis, I utilize state-of-the-art N–body simulations of sufficient resolution that I can draw direct comparison between the simulations and observations. My investigative approach – dividing the MW into separate morphological components to consider individually – simplifies and distills the most essential arguments here: to first order, can I discard any theories of how the MW formed and what matter it contains? This thesis aims to answer that question. But first, I present the Galactic data that is the benchmark for this comparison.

1.1 SDSS Galactic Data

Several key structural elements of the MW have long been known to exist: the bulge, the thin/thick disk system, and the halo. However, with the advent of the Sloan Digital Sky Survey (SDSS) (York et al., 2000), the observational data associated with two of these components, thin/thick system and halo, has dramatically improved. In particular, several recent studies based on the SDSS data have provided strong observational constraints on the structural, kinematic and chemical properties of stars associated with the thin/thick disk system and halo structure within the solar cylinder.

Jurić et al. (2008, hereafter J08) used a photometric parallax method on SDSS data to estimate distances to ∼48 million stars to study their spatial distribution. Because SDSS provides accurate photometry, which enables reasonably robust distances (10–15%, Sesar et al. 2008), as well as faint magnitude limits ($r < 22$) and a large sky coverage (6,500 deg^2 in J08 study; the latest SDSS Data Release 9 includes imaging data for about 15,000 deg^2), J08 were able to strongly constrain the parameters of a model for the thin/thick disk and halo spatial distribution of stars in the MW.

Ivezić et al. (2008a, hereafter I08) further extended the J08 analysis of the SDSS data by developing a photometric metallicity estimator; I08's analysis found characteristic metallicities and trends associated with both the thin/thick disk system and halo structure. Following this, Bond et al. (2010, hereafter B10) performed a detailed analysis of available kinematic data for the SDSS stellar sample by combining radial velocities from the SDSS spectroscopic survey and proper motions distilled from the SDSS astrometry and the Palomar Observatory Sky Survey astrometry (Munn et al., 2004).

A synopsis of the J08, I08 and B10 observational findings for the MW thin/thick disk system and the MW halo structure is outlined below:

1.1.1 The Milky Way Disks

J08 found that the disk system can be modeled as a sum of two exponential disks; their model is qualitatively similar to previous work (*e.g.* Bahcall & Soneira 1980) which identifies a clear change of slope in the counts of disk stars as a function of distance from the Galactic

plane. This change in slope is usually interpreted as the transition from the thin to thick disk (Gilmore & Reid, 1983; Siegel et al., 2002). After correcting for biases due to unresolved binary stars, J08's best-fit double exponential profile for the 4.6 million stars found in four bins of r-i > 1 is a thin and thick disk scale height of 300 pc and 900 pc, with a local thick disk to thin disk normalization of $\sim$0.12.

I08 studied the dependence of the metallicity, [Fe/H], and rotational velocity, V_ϕ, of disk stars and detected smooth gradients of both quantities over the distance ranging from several hundred parsecs to several kiloparsecs. Such gradients would be expected in a thin/thick disk decomposition where the thick disk stars are a separate population defined by a bulk rotational velocity lag and a lower metallicity compared to those of the thin disk. However, such a model would also predict a strong correlation between the metallicity and the velocity lag, which is excluded ($\sim 7\sigma$ level) by the I08 analysis.

1.1.2 The Milky Way Halo

For the MW halo, J08's best-fit model was an oblate bi-axial (cylindrically symmetric) power-law distribution described by

$$\nu_H(R,Z) = \nu_D(R_\odot, 0)\, \epsilon_H \left(\frac{R_\odot^2}{R^2 + (Z/q_H)^2} \right)^{n_H/2}, \tag{1.1}$$

where $\nu_D(R_\odot, 0)$ is the local Solar neighborhood density of tracer stars, and ϵ_H measures the local fractional contribution of halo stars. The J08 best fit parameters for this model is $\epsilon_H = 0.0051$, $q_H = 0.64$, and $n_H = 2.77$, with estimated uncertainties of 25%, $\lesssim$0.1, and $\lesssim$0.2, respectively.

I08 studied the metallicity distribution of halo stars and found that a fairly simple selection, $[Fe/H] = -1$, clearly separates disk and halo components. B10 found velocity ellipsoid for halo stars is invariant in spherical coordinates within the volume probed by the SDSS data (galactocentric distances of $\lesssim$20 kpc). They concluded the SDSS stellar halo kinematics are well fit by a simple triaxial velocity ellipsoid with σ_{RR}=141 km s^{-1}, $\sigma_{\phi\phi}$=85 km s^{-1}, and $\sigma_{\theta\theta}$=75 km s^{-1}, with uncertainties of about 5 km s^{-1} per component.

1.2 N–body Simulations

To try to understand how the thin/thick disk system could have formed and what the halo is made of, this thesis utilizes N–body simulation data. Until recently, simulations did not posses sufficient resolution nor adequate observational properties to draw meaningful comparisons to the MW. However, within the last 5 years, simulations have improved to the point that we can observe the processes (internal and external) that shape the structure as a function of time. While simulation data cannot give us definitive knowledge that *this* is how the MW formed (that is, simulations can be consistent with observation but still prescriptively incorrect), if a simulation is inconsistent with observations, then we can throw that model out. And if a simulation is indeed consistent with observations, we can use it as a starting place to make further predictions to test the model, which in turn can be tested with additional observations.

I utilized two types of N–body simulations in the course of this research: an isolated simulation designed to investigate the role of a secular process (radial migration) in building the thin/thick disk system and a cosmological simulation with sufficient resolution to test Jeans equations in a non-equilibrium system. Both simulations were generated using the using the parallel N–body+SPH code GASOLINE (Wadsley et al., 2004), which contains realistic gas, cooling and stellar feedback (Stinson et al., 2006; Shen et al., 2009).

1.2.1 Theories & Techniques

There are two theories/techniques that my thesis specifically investigates: can radial migration create a realistic thin/thick disk system and can Jeans equations provide evidence for the presence of dark matter within the SDSS Galactic volume?

1.2.1.1 Radial Migration

Radial migration due to transient spirals was first described by Sellwood & Binney (2002). In this model energy and angular momentum changes in stellar orbits occur from interactions with transient spiral arms, which move stars at corotation resonance inward or outward in radius while preserving the near circularity of their orbits. Using a semi-analytic approach,

Schönrich & Binney (2009a,b) demonstrated that the MW's thick disk could result from radial migration. Roškar et al. (2008a,b, R08ab hereafter) studied radial migration in N–body+SPH simulations of disk formation, and showed that migrations are possible on short timescales. They explored the implications of radial mixing for stellar populations for a variety of stellar systems, including the solar neighborhood. Here I extend their work by studying the vertical evolution that occurs as a result of migration within one of their simulations.

1.2.1.2 Jeans equations

One of the great mysteries of astronomy today is constraining the nature of dark matter. An old technique for inferring its existence that has experienced a recent resurgence of interest is applying Jeans equations to stars to infer the underlying mass distribution (Jeans, 1915; Oort, 1932). Although it is hard to measure stellar acceleration, which would directly constrain the gravitational potential, it is possible to estimate it statistically from stellar kinematics using Jeans equations.

Jeans equations follow from the collisionless Boltzmann equation; for detailed derivation see Binney & Tremaine (1987). Assuming an axisymmetric and steady-state system, mean acceleration can be expressed in terms of observable quantities: the stellar number density distribution, ν, the mean azimuthal (rotational) velocity $\overline{v_\phi}$, and four velocity dispersions, $\sigma_{\phi\phi}$, σ_{RR}, σ_{ZZ}, and σ_{RZ}. These quantities all are accessible in the MW SDSS halo data set, and thus in principle, Jeans equations can be applied to the sample to infer information about the existence of dark matter.

If the MW halo was perfectly axisymmetric and steady-state, Jeans equations would exactly predict mean accelerations. However, because we expect the MW halo to deviate from these assumptions (e.g., due to stellar streams and other substructure), the effectiveness of Jeans equations as a technique to predict the underlying mass distribution must be quantitatively tested against known accelerations from realistic simulations. If the results are consistent with expectations, then, in the limit that the test system is a reasonable approximation for the MW halo, the same technique can be applied to the MW halo data.

1.3 Brief Thesis Outline

Chapter 2 describes the role radial migration plays in building a thin/thick disk system in an isolated N–body simulation. I compare and contrast the spatial, kinematic and chemical properties of a simulated solar cylinder to the observational findings of J08, I08 and B10. I find that radial migration naturally produces all the qualitative trends seen within the thin/thick disk system; in particular, Chapter 2 shows that radial migration reproduces the V_ϕ vs $[Fe/H]$ relationship observed in the thin/thick disk transition zone that is not reproduced in other models.

In Chapter 3, I test the validity of applying Jeans equations to a non-equilibrium cosmologically derived N–body simulation, and I show that Jeans equations return reasonable accelerations. I use the same simulation to demonstrate that the accelerations predicted by Jeans equations when applied to a synthetic MW halo data set point toward the existence of dark matter within the volume. I further explore an analytic application of Jeans equations to assess a global property – the dark matter axis ratio – within the SDSS volume with the simulation, and generate predictions for the MW halo using this technique.

Chapter 4 summaries the results presented in Chapter 2 and Chapter 3. In this section I summarize recent work that others have produced as a natural extension of the work presented in Chapter 2 and Chapter 3. I also discuss future work that I will undertake to expand the research presented here.

Chapter 2

BUILDING THE MILKY WAY THICK DISK THROUGH RADIAL MIGRATION

This chapter has been published as Loebman et al. 2011, ApJ, 737, 8, and is reproduced by permission of the AAS.

2.1 Chapter Summary

We compare the spatial, kinematic and metallicity distributions of stars in the Milky Way disk, as observed by SDSS and GCS, to predictions made by N-body simulations that naturally include radial migration as proposed by Sellwood & Binney (2002). In these simulations, stars that migrate radially outward feel a decreased restoring force, consequentially they reach larger heights above the midplane. We find this model is in qualitative agreement with observational data and can explain the disk's double-exponential vertical structure and other characteristics as due to internal evolution. In particular, the model reproduces observations of stars in the transition region between exponential components, which do not show a strong correlation between rotational velocity and metallicity. Although such a correlation is present in young stars because of epicyclic motions, radial migration efficiently mixes stars and weakens the correlation. Classifying stars as members of the thin or thick disk by either velocity or metallicity leads to an apparent separation in the other property, as observed. We find a much stronger separation when using [α/Fe], which is a good proxy for stellar age. The model success is remarkable because the simulation was not tuned to reproduce the Galaxy, hinting that the thick disk may be a ubiquitous galactic feature generated by stellar migration. Nonetheless, we cannot exclude that some fraction of the thick disk is a fossil of a past more violent history, nor can radial migration explain thick disks in all galaxies, most strikingly those which counter-rotate with respect to the thin disk.

2.2 Background

In the years since Gilmore & Reid (1983) first proposed a two component structure to the Milky Way disk, a large body of observational work has provided supporting evidence for contrasting thin and thick disk attributes. Structurally, the thin disk scale height is shorter than thick disk scale height (for reviews see Majewski, 1993; Buser et al., 1999; Norris, 1999, and references therein), and the thick disk may have a longer scale length than the thin disk (Robin et al., 1996; Ojha, 2001; Chen et al., 2001; Larsen & Humphreys, 2003). Kinematically, thick disk stars have larger velocity dispersions and lag the net rotation of the disk (Nissen, 1995; Chiba & Beers, 2000; Gilmore et al., 2002; Soubiran et al., 2003; Parker et al., 2004; Wyse et al., 2006). Additionally, thick disk stars are older and metal poor relative to their thin disk counterparts (*e.g.* Majewski, 1993; Chiba & Beers, 2000; Bochanski et al., 2007) and at a given iron abundance thick disk stars are α-enhanced (Fuhrmann, 1998; Prochaska et al., 2000; Tautvaišienė et al., 2001; Bensby et al., 2003; Feltzing et al., 2003; Mishenina et al., 2004; Brewer, 2004; Bensby et al., 2005). Moreover, the presence of both a thin and a thick disk is not unique to the Milky Way but a ubiquitous feature of late type galaxies (Burstein, 1979; van der Kruit & Searle, 1981; Abe et al., 1999; Neeser et al., 2002; Yoachim & Dalcanton, 2005, 2006; Yoachim, 2007).

Recently, several studies based on the Sloan Digital Sky Survey (SDSS) have provided further strong observational constraints on the structural, kinematic and chemical properties of stars in the solar cylinder. Jurić et al. (2008, hereafter J08) used a photometric parallax method on SDSS data to estimate distances to $\sim$48 million stars and studied their spatial distribution. Because SDSS provides accurate photometry, which enables reasonably robust distances (10–15%, Sesar et al. 2008), as well as faint magnitude limits ($r < 22$) and a large sky coverage (6500 deg^2), J08 were able to strongly constrain the parameters of a model for the global spatial distribution of stars in the Milky Way. The J08 model is qualitatively similar to previous work (*e.g.* Bahcall & Soneira 1980) which identifies a clear change of slope in the counts of disk stars as a function of distance from the Galactic plane; this change in slope is usually interpreted as the transition from the thin to thick disk (Gilmore & Reid, 1983; Siegel et al., 2002).

Ivezić et al. (2008a, hereafter I08) further extended this global analysis of SDSS data by developing a photometric metallicity estimator and by utilizing a large proper motion catalog based on SDSS and Palomar Observatory Sky Survey data (Munn et al., 2004). I08 studied the dependence of the metallicity, [Fe/H], and rotational velocity, V_ϕ, of disk stars on the distance from the Galactic plane and detected gradients of both quantities over the distance ranging from several hundred parsecs to several kiloparsecs. Such gradients would be expected in a thin/thick disk decomposition where the thick disk stars are a separate population defined by a bulk rotational velocity lag and a lower metallicity compared to those of the thin disk. However, such a model would also predict a strong correlation between the metallicity and the velocity lag, which is excluded ($\sim 7\sigma$ level) by the I08 analysis[1] (see Figure 17, I08). In this work we turn to a more sophisticated Galactic description — an N–body model — to characterize stars within the SDSS volume.

Over the past few decades, N–body simulations have been used to provide supporting evidence for three distinct theories of thick disk formation: violent relaxation (Jones & Wyse, 1983), substructure disruption (Statler, 1988), and heating by satellites (Quinn et al., 1993). Several works have recently revisited these ideas. Brook et al. (2004) formed a thick disk in situ at high redshift during gas-rich mergers, where star formation is triggered by the rapid accretion of gas; this result is consistent with the thick disk forming through violent relaxation of the galactic potential. Bournaud et al. (2009) further studied the effect of violent relaxation and found internal disk instabilities rather than mergers generates a thick disk with proper morphology. Abadi et al. (2003) showed that by tidally stripping/accreting satellites, the majority of the oldest stars in the thick disk could have formed externally. Kazantzidis et al. (2008), Villalobos & Helmi (2008), and Villalobos et al. (2010) investigated substructure disruption by using a cosmologically derived satellite accretion history to perturb a Milky Way-like disk; subhalo-disk encounters increased the scale height of this disk at all radii effectively forming a thick disk.

In this work, we study a different mechanism of thick disk formation: radial migration

[1] A recent claim that a correlation between the metallicity and the velocity lag does exist for [Fe/H]< -0.5 by Spagna et al. (2010) is discussed in Appendix A. Even if their results are taken at face value, the drop in rotational velocity is only $\sim$20 km s^{-1} between [Fe/H]$=-1$ and [Fe/H]$=-0.5$.

(Schönrich & Binney, 2009a,b; Sales et al., 2009; Loebman et al., 2008; Caruana, 2009). Radial migration due to transient spirals was first described by Sellwood & Binney (2002). In this model energy and angular momentum changes occur from interactions with transient spiral arms, which move stars at the corotation resonance inward or outward in radius while preserving their nearly-circular orbits. Other authors have in recent years studied radial migration, both due to the corotation scattering (**?**) as well as bar-spiral resonant interactions (Minchev & Famaey, 2010). Using a semi-analytic approach, Schönrich & Binney (2009a,b) demonstrated the Milky Way's thick disk could result from radial migration. Roškar et al. (2008a,b, R08ab hereafter) studied radial migration in N–body + Smooth Particle Hydrodynamic (SPH) simulations of disk formation, and explored the implications of radial mixing for stellar populations for a variety of stellar systems, including the solar neighborhood. Here we extend their work by highlighting the vertical evolution that occurs as a result of migration.

We note that in this paper, we are not testing the validity of the other models of formation. However, recently, Sales et al. (2009) proposed using the eccentricity of orbits of stars in the thick disk to constrain the thick disk's formation mechanism; they presented the eccentricity distributions that result from four N–body simulations: Abadi et al. (2003), Villalobos & Helmi (2008), R08b, and Brook et al. (2004). They found that the distributions that result from heating, radial migration and mergers all had a strong peak at low eccentricity ($\epsilon \sim 0.2 - 0.3$), while the distribution that results from accretion is centered at higher orbital eccentricities ($<\epsilon> \sim 0.5$). Building on this, Wilson et al. (2010) studied the eccentricity of orbits of stars in the thick disk observed in the Radial Velocity Experiment (RAVE) (Steinmetz et al., 2006) and found these results to be inconsistent with expectations for the pure accretion simulation (but see also Di Matteo et al., 2011). Ruchti et al. (2010) also utilized α measurements from RAVE to conclude that the α-enhancement of the metal-poor thick disk implies that direct accretion of stars from dwarf galaxies did not play a major role in the formation of the thick disk. Using SDSS DR7, Dierickx et al. (2010) showed that the eccentricity of stellar orbits in the thick disk implies the thick disk is unlikely to be fully populated by radially migrated stars. We note that we cannot exclude that some fraction of the thick disk is a fossil of a past more violent history, nor can this

scenario explain thick disks in all galaxies. However, in what follows, we show that a large fraction of the stars in the thick disk could have formed within the disk at smaller radii and arrived at their present location via radial migration.

The outline of this paper is as follows: in §2.3, we present our adopted simulation, which contains substantial migration; we also present a contrasting control case, which has little migration relative to the disk scale-length. When we compare these two simulations we show that migration can build a thick disk as first defined by Gilmore & Reid (1983): a component with a scale-height larger than that of the thin disk. In §2.4, we qualitatively compare the adopted simulation with SDSS observations to show that they match each other sufficiently well to pursue further comparison. In §2.5, we present a detailed comparison between the simulation and the local SDSS volume focusing on the reason for the absence of a strong correlation between V_ϕ and [Fe/H]. In §2.6, we use the simulation as a proxy for the Milky Way to show that classifying stars as members of the thin or thick disk by either velocity or metallicity leads to an apparent separation in the other property as observed. In §2.7, we compare our results to recent theoretical work that used semi-analytics to investigate how the solar neighborhood could have been shaped by radial migration and chemical evolution effects. In §2.8 we explore the correlation between [α/Fe] and age to highlight the diagnostic power of [α/Fe] as a stand-in for age. In §2.9 we summarize our results and conclusions, and in Appendix 2.10, we reconsider recent observational claims concerning the lack of correlation between V_ϕ and [Fe/H].

2.3 Numerical Simulations

We analyze the results of an N–body + SPH simulation designed to mimic the quiescent formation and evolution of a Milky Way–mass galaxy following the last major merger. The system is initialized as in Kaufmann et al. (2007) and R08ab and consists of a rotating, pressure–supported gas halo embedded in an NFW (Navarro et al., 1997) dark matter halo. This simulation was evolved for 10 Gyr using the parallel N–body+SPH code, GASOLINE (Wadsley et al., 2004). As the simulation proceeds, the gas cools and collapses to the center of the halo, forming a thin disk from the inside–out. Gas is continually infalling from the hot halo onto the disk for the duration of the simulation. Star formation and stellar feedback

are modeled with subgrid recipes as described in Stinson et al. (2006). Importantly, the stellar feedback prescriptions include SN II, SN Ia and AGB metal production, as well as injection of supernova energy which impacts the thermodynamic properties of the disk interstellar medium (ISM). Metal diffusion is calculated from a subgrid model of eddy turbulence based on the local smoothing length and velocity gradients (Smagorinsky, 1963; Wadsley et al., 2008). The simulation we utilize is nearly identical to R08ab (see R08ab for further details), but with the addition of metal diffusion between gas particles (Shen et al., 2009). We experimented with a few values of the diffusion coefficient and settled on a diffusion parameter D=0.05, which we find to yield reasonable metallicity distributions in the solar neighborhood.

No *a priori* assumptions about the disk's structure are made — its growth and the subsequent evolution of its stellar populations are completely spontaneous and governed only by hydrodynamics/stellar feedback and gravity. Although we do not account for the full cosmological context, merging in the ΛCDM paradigm is a higher order effect at the epochs in question (Brook et al., 2005). Thus, our model galaxy lacks some structural components such as a stellar halo, which in ΛCDM is built up primarily during the merging process (*e.g.* Bullock & Johnston, 2005; Zolotov et al., 2009). Our focus here, however, is disk evolution; by simplifying our assumptions, we are able to use much higher resolution and more easily study the impact of key dynamical effects on observational properties of stellar populations within the disk.

The gas disk in our model grows spontaneously from quiescent accretion of condensing halo gas. Once the baryons are arranged in the disk, they reach densities high enough for star formation, which proceeds according to our sub-grid prescriptions (see Stinson et al. 2006). During most of the evolution, the stellar disk is marginally stable, with Toomre Q values ranging from 2-3 in the main part of the disk (Q is higher for $R < 2$ kpc where velocity dispersion is high and in the outskirts where the density drops quickly). This marginal (in)stability allows for the continuous triggering of transient spirals.

To quantify the spirals, we expand the density distribution in a Fourier series and extract pattern speeds and amplitudes of the dominant patterns at different radii. We find that multiple spirals are always present in the disk, each with a different pattern speed domi-

nating a different part of the disk. The m=2 spirals are always the dominant component, although spirals of higher multiplicity are also present. Figure 2.1 shows the time evolution of the m=2 Fourier amplitude in four different radial bins. The amplitude of m=2 spirals varies from 0.1-0.4, though there are not many instances where the Fourier amplitude exceeds 0.2. Further details regarding the nature of spirals in our simulations are beyond the scope of this paper, but will be presented in a forthcoming publication.

Based on their simulations, R08ab presented the implications of stellar radial migration resulting from the interactions of stars with transient spiral arms (Sellwood & Binney, 2002) on the observable properties of disk stellar populations. Radial migration efficiently mixes stars throughout the disk into the solar neighborhood, resulting in a flattened age-metallicity relation, a broader metallicity distribution function (R08ab), and significantly altered kinematics (Sales et al., 2009). Figures 2.2 and 2.3 illustrate the basic premise of this paper — stars that presently occupy the solar neighborhood were not all born there, but have come from a wide range of radii. As the stars migrate radially outward, their vertical motions carry them to much larger heights; because the disk midplane potential is shallower at the new location, the amplitude of stars' vertical oscillations increase. This effect is clearly seen in Figure 2.3 - as we consider distributions of formation radius and age at increasing heights above the plane, the stars are predominantly old and have originated in the inner disk. Previous studies have shown (Schönrich & Binney, 2009a,b; Sales et al., 2009; Loebman et al., 2008; Caruana, 2009) that the vertical evolution resulting from radial migration can influence the characterization of the thick disk.

In this paper we use an improved version of the simulation utilized by R08ab because the simulation has roughly the same mass and size as the Milky Way (MW). As such we often refer to it, for brevity, as the MW simulation, to distinguish it from the second simulation we present below. We stress however that the MW simulation is not meant to represent the Milky Way in detail – the simulated galaxy is slightly more massive ($V_{circ} \sim 250\ \ \mathrm{km\,s^{-1}}$) and only has a weak oval whereas the MW is barred.

In order to further illustrate the importance of radial migration, we repeated much of our analysis on a control case. The control simulation is a system with the same initial conditions as the MW simulation except for having a higher angular momentum content

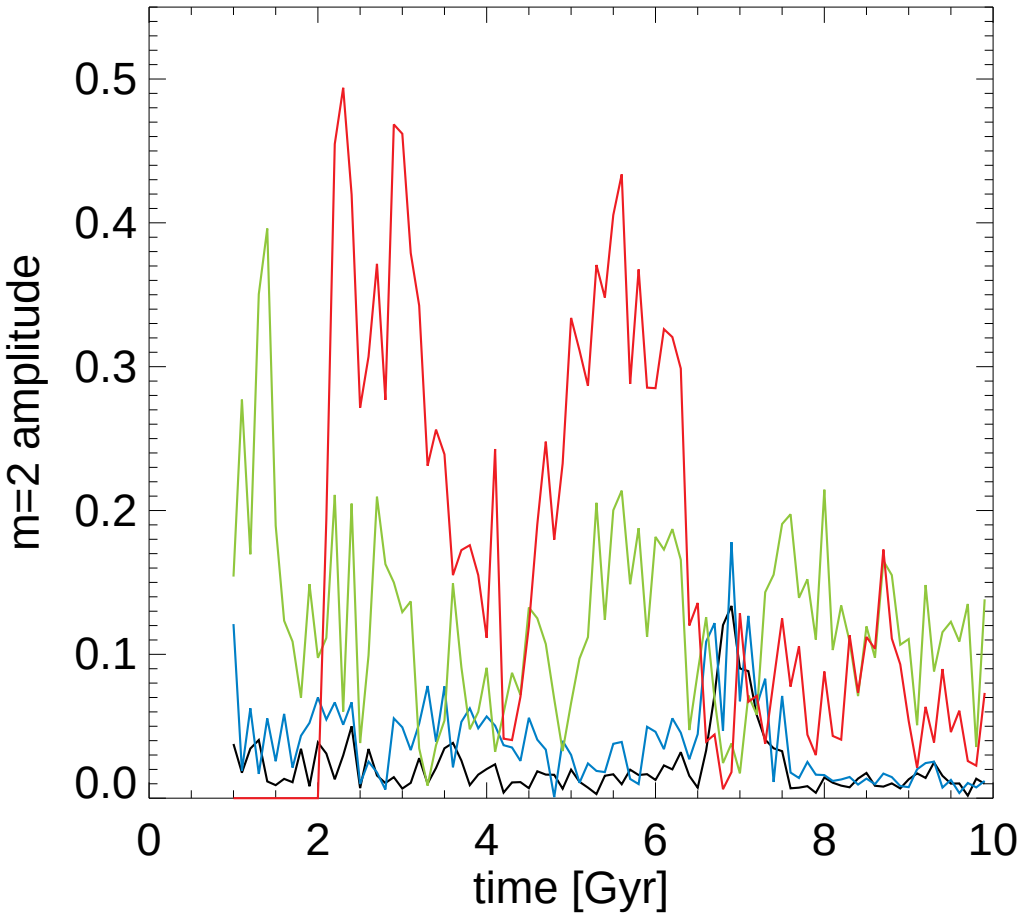

Figure 2.1 Time evolution of the m=2 Fourier amplitude for the MW run. Black, blue, green, and red lines correspond to radial bins centered on 1.2, 2.4, 4.5 and 9.0 kpc respectively. The bins are 0.3 kpc wide.

with a dimensionless spin parameter $\lambda = 0.1$ (Bullock et al., 2001). This results in a more extended disk (final disk scale-length = 3.71 kpc, versus 2.54 kpc for the MW simulation), possibly similar to a low surface brightness galaxy; we therefore refer to this simulation as the LSB simulation. Due to its lower surface density, the disk forms weaker spirals and as a result the stellar populations at all radii are less affected by radial mixing. When we compare migration as a function of scale-lengths, we find that there is significantly less migration in the LSB galaxy than in the MW galaxy. This can be seen in Figure 2.2: the dotted lines show the distribution of formation radii for stars in the LSB simulation (versus the MW simulation shown in solid lines); the LSB distribution shows a much smaller offset from the stars' present radius, highlighted in gray, than the MW's. Thus, the weaker spirals of the LSB simulation cause significantly less radial migration than in the MW model.

We checked explicitly that the weaker spiral structure in the LSB case is not a result of numerical suppression due to limited spatial resolution. Calculating the ratio of the softening length to $\lambda_{crit} = 4\pi^2 G\Sigma_s/\kappa^2$, where G is the gravitational constant, Σ_s is the stellar surface density and κ is the epicyclic frequency, we find that for the LSB case it is $\ll 1$ at all radii of interest. For the fiducial simulation, the ratio only approaches unity beyond 15 kpc. Because λ_{crit} is indicative of the spatial scale of expected spirals, this test argues that we are adequately resolving the structure in our simulated disks.

The distribution of stellar mass away from the midplane is strongly affected by radial migration; this can be seen in Figure 2.4, which contrasts the MW simulation against the LSB case. Here the normalized mass density distribution within four analogous cylindrical volumes drawn from a variety of radii are presented. At larger radii, the steepness of the profiles are quite different; the LSB simulation has a constant slope while the MW simulation shows a transition from a steep to a shallow density distribution. Thus the MW simulation cannot be characterized by a single exponential or sech^2 component in the vertical direction, as we show explicitly in the following Section and Figure 2.6. It is this double-component nature which first led to the identification of the thick disk (Gilmore & Reid, 1983); we have thus shown that internal evolution may also give rise to this important feature.

Not only do the two models yield very different vertical density profiles, but the resulting stellar population properties are also drastically different in the model with little migration.

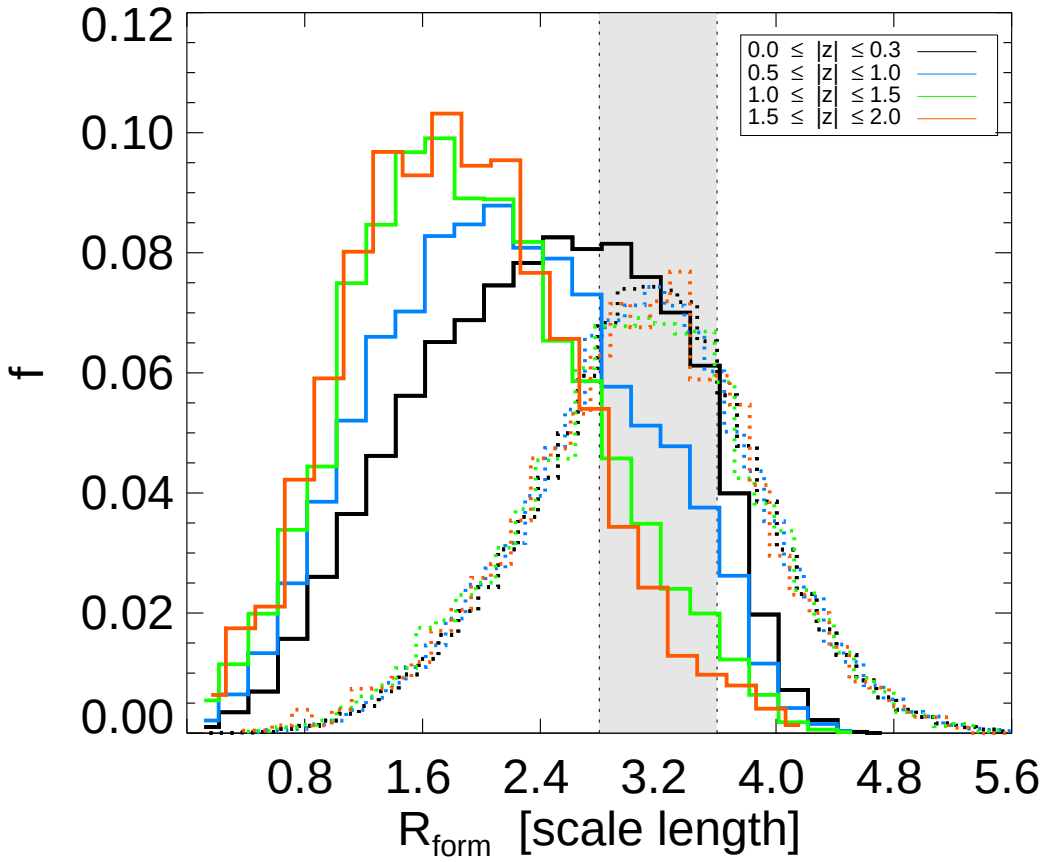

Figure 2.2 Star particles that fall within the solar cylinder at the end of the simulation are considered here. These stars are broken into four volumes by distance away from the mid-plane, $|z|$, with low to medium to high given by black to blue to green to red. For comparison, four similar volumes from the LSB simulation with little relative radial migration are over-plotted (dotted lines). For each volume, the formation radius of stars is shown; in the MW simulation, away from the mid-plane, a large fraction of the stars formed significantly interior to their final location. For reference, the solar cylinder is indicated in the shaded gray region: galactocentric radius = 2.8–3.6 scale lengths. In the MW simulation this corresponds to 7 kpc $\leq R \leq$ 9 kpc while in the LSB simulation it corresponds to 10 kpc $\leq R \leq$ 13 kpc.

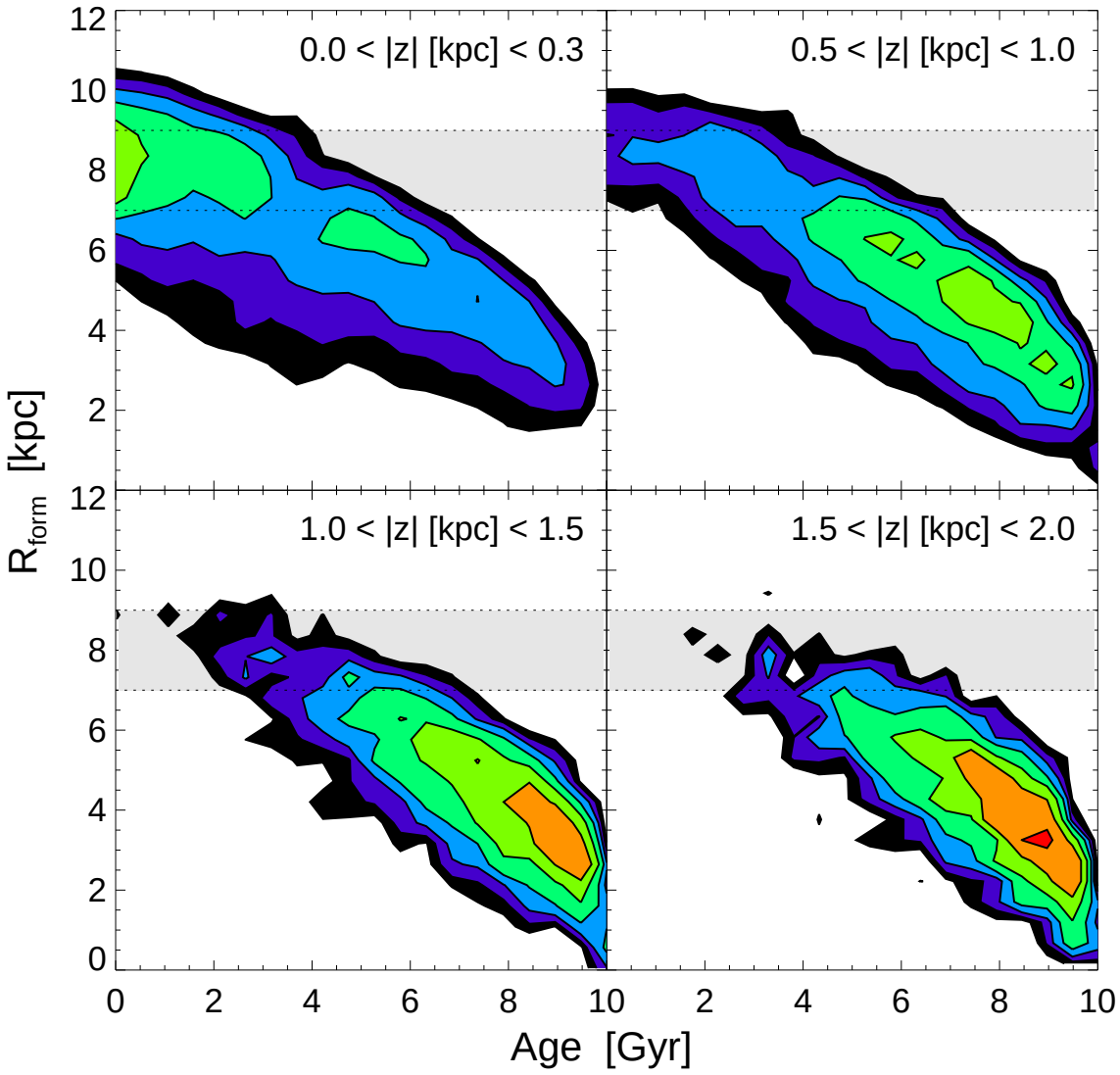

Figure 2.3 Contour plots of the MW simulation showing the distribution of R_{form} *vs. Age* for the four volumes considered in Figure 2.2 with solar cylinder shaded in gray. For all z, older stars formed significantly interior to their final location; this net outward movement of stars over time is due to radial migration. Volumes sampling the thick disk ($|z| \geq 1$ kpc) are dominated by older stars that have migrated to the solar radius from interior radii.

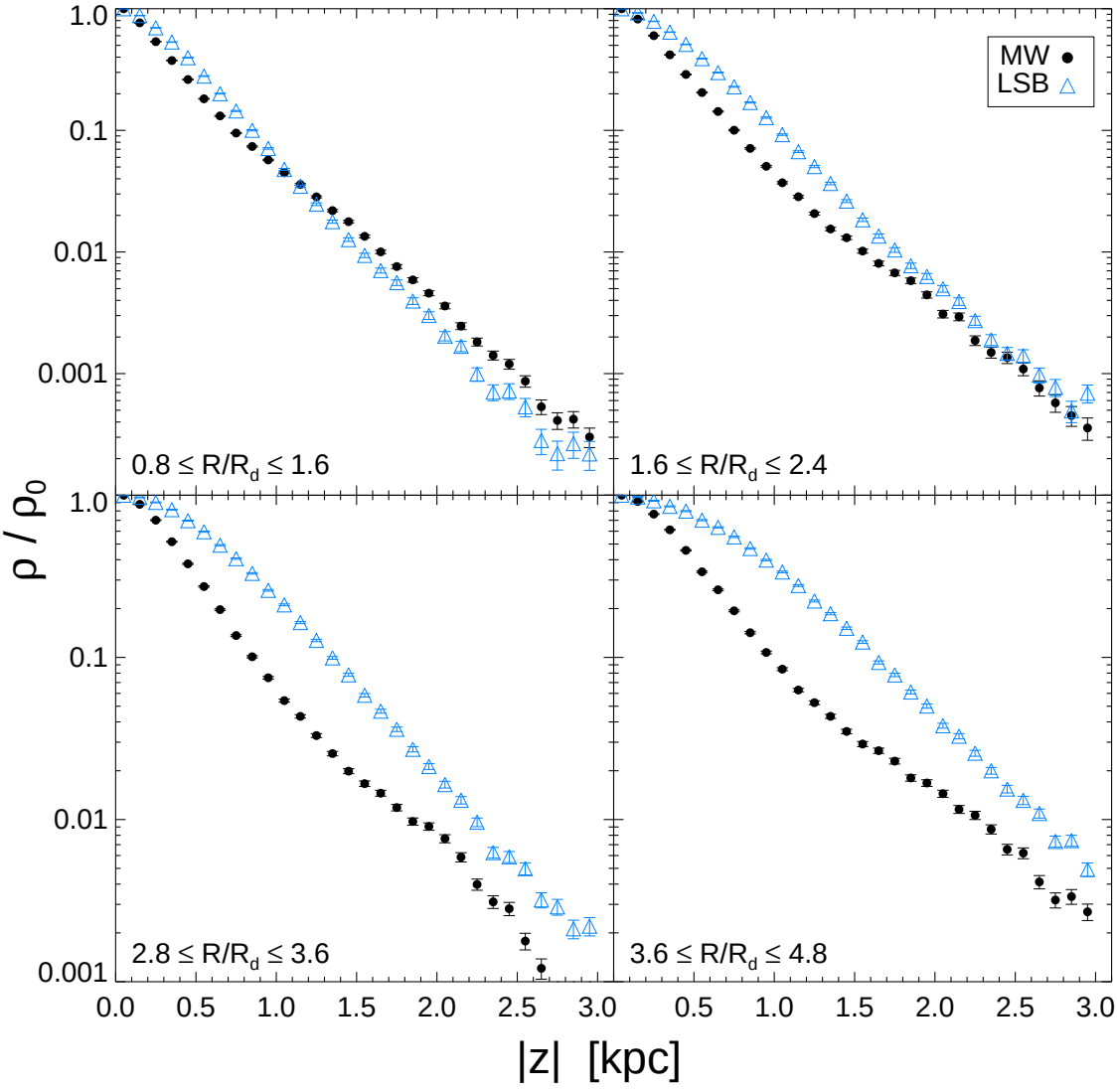

Figure 2.4 Density profiles drawn from analogous regions within the MW and LSB simulations. At larger radii, the LSB simulation has a fairly flat (pure exponential) profile whereas the MW simulation has a transition between a steep and shallow profile.

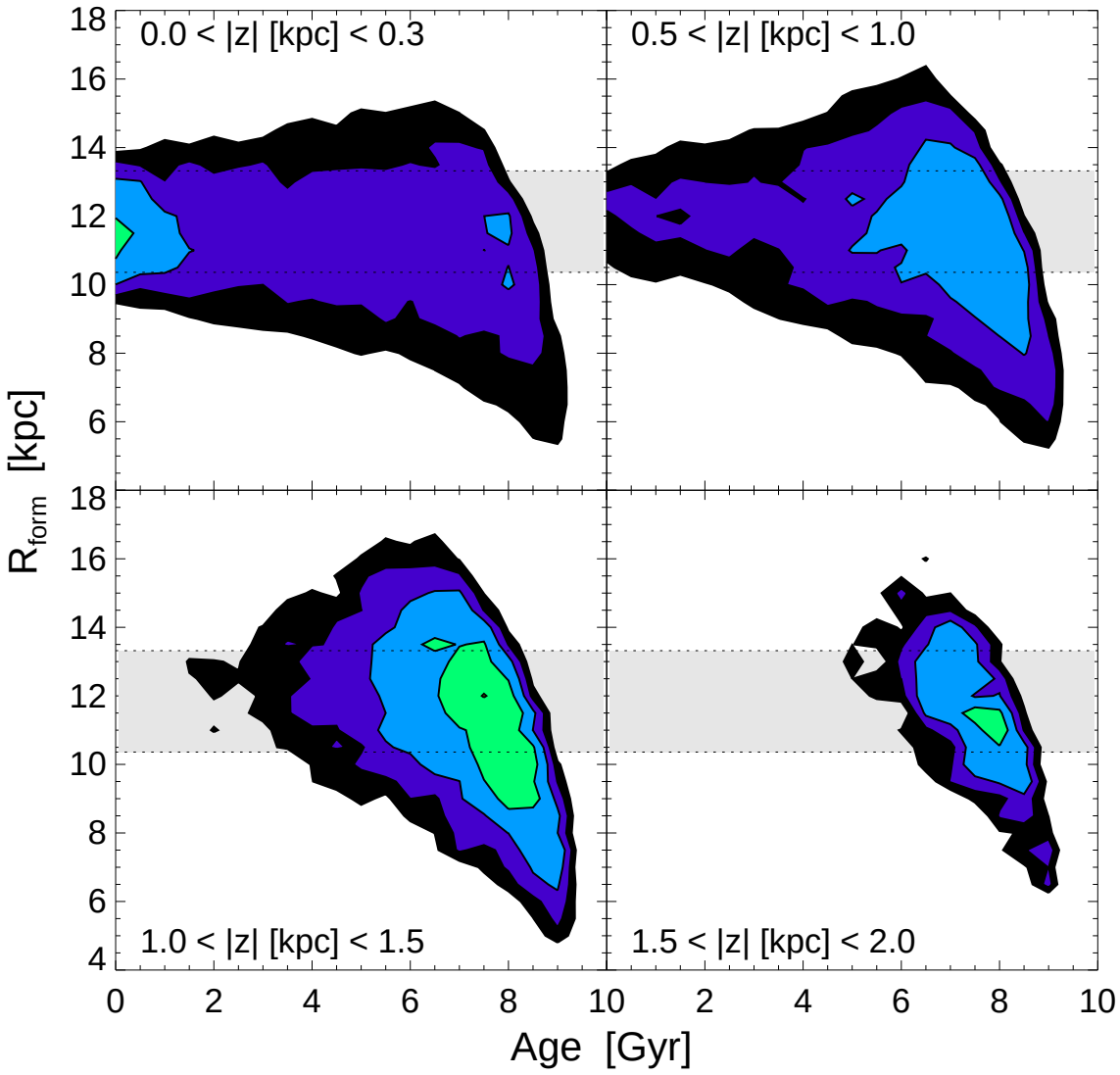

Figure 2.5 Same as Figure 2.3 but for the LSB simulation which has relatively little radial migration. Regardless of distance away from the midplane, all stars originate from a roughly symmetric distribution centered at the midpoint of the cylindrical volume. While volumes sampling the thick disk ($|z| \geq 1$ kpc) are dominated by older stars, these stars are largely uninfluenced by radial migration.

R [kpc]	N1 [$M_\odot/pc^3$]	h1 [pc]	N2 [$M_\odot/pc^3$]	h2 [pc]
$2-4$	0.638	239	1.000	266
$4-6$	0.237	316	0.044	763
$7-9$	0.098	381	0.014	913
$9-12$	0.035	444	0.004	1197

Table 2.1 Best fit parameters to radial bins sampled in Figure 2.6 given by: thin disk normalization ($N1$), thin disk scale height ($h1$), thick disk normalization ($N2$), & thick disk scale height ($h2$).

Comparing Figure 2.5 with Figure 2.3, it is clear that unlike in the MW model, where virtually all stars found at significant heights above the plane come from the inner disk, most stars in the LSB disk simply stay put over time. The properties of stars away from the midplane in the MW model discussed in the forthcoming sections are therefore a unique consequence of the radial migration process.

2.4 Comparison of Simulations with SDSS

In the following section, we compare SDSS observations with the MW simulation to demonstrate its usefulness as a model for understanding the Milky Way thick disk. Here we study the stellar mass distribution, rotational velocity and metallicity as functions of distance from the Galactic plane, $|z|$, and galactocentric cylindrical radius, R. We draw qualitative comparisons between the datasets by examining their mass-weighted metallicity and kinematic distributions in this R–$|z|$ space.

The observed Milky Way disk is best fit by a 2-component model that is exponential both in the R and z directions (see Table 10, bias-corrected results, J08). The top panel of Figure 2.7 shows the mass-weighted density distribution of the entire MW simulation at its final timestep. This distribution is in qualitative agreement in both the R and z directions with J08 for up to $\sim$2.5 kpc above the disk's plane and $\sim$15 kpc from the galactic center.

Figure 2.6 shows our best fits to the vertical density profiles for the MW simulation for radial bins $R = 2-4$ kpc, $R = 4-6$ kpc, $R = 7-9$ kpc and $R = 9-12$ kpc. As in

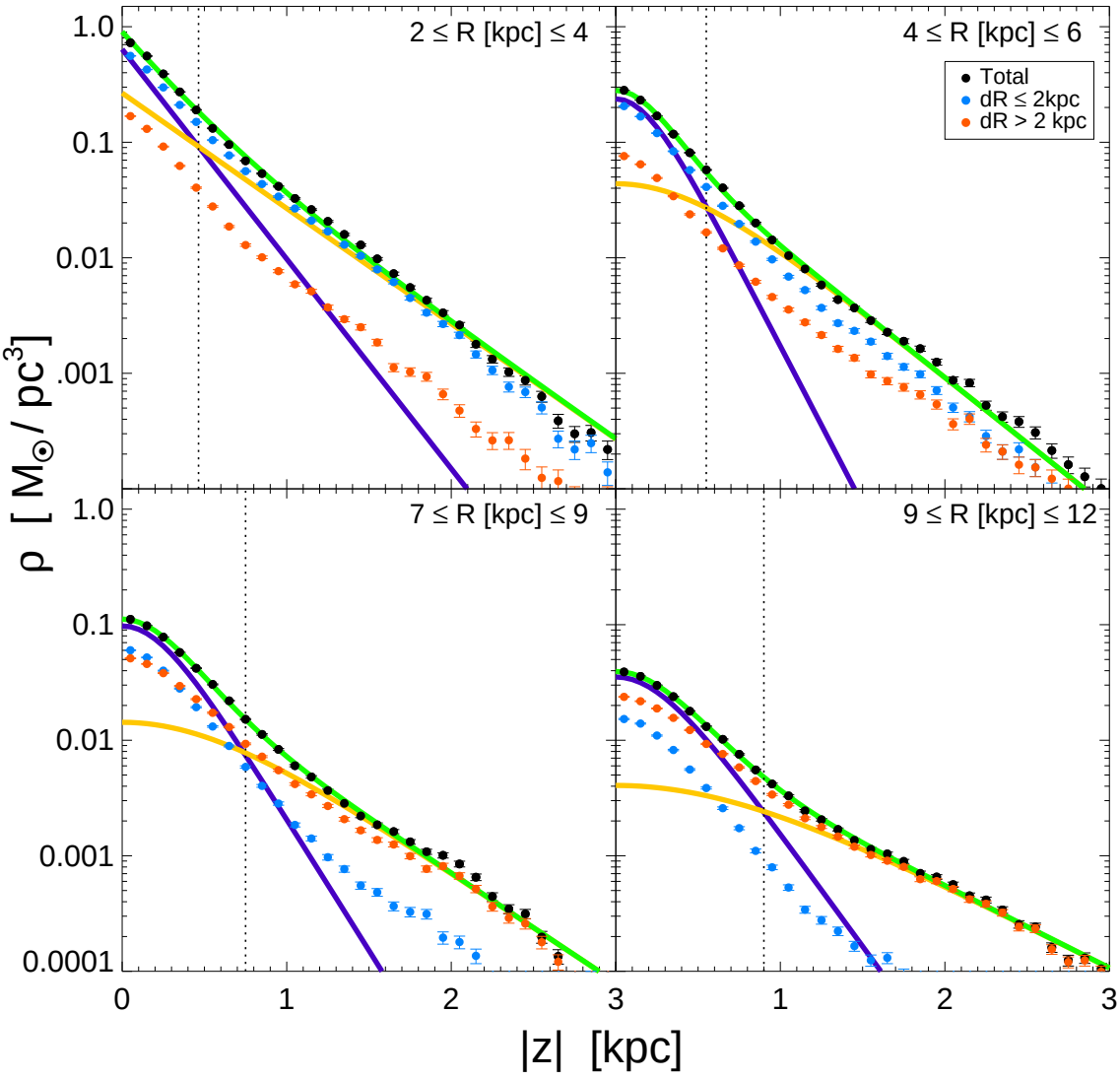

Figure 2.6 Simultaneous fits to the vertical density profile in the MW simulation for radial bins: $R = 2 - 4$ kpc, $R = 4 - 6$ kpc, $R = 7 - 9$ kpc, $R = 9 - 12$ kpc. While the radial bin sampling the smallest radii is best fit by a double exponential function, all other bins are better fit by a double sech^2 function. Best fit parameters are given in Table 2.1. Thin, thick, and total curves shown in purple, orange and green respectively; the vertical dotted line marks the intersection between thin and thick disk components. Red and cyan points represent stellar mass density that has migrated more than 2 kpc or less than 2 kpc respectively from radius of formation.

J08, the innermost radial bin is best fit by a double exponential function; however, all other bins are better fit by the sum of two double sech^2 profiles, which is in agreement with the theoretical work by Spitzer (1942) and observational results for other galaxies by Yoachim & Dalcanton (2006). Despite the small discrepancy between sech^2 vs. exponential fits, the simulation is in good qualitative agreement with the SDSS-based analysis of the Milky Way (J08).

In addition, Figure 2.6 shows the vertical density profiles as divided into two populations: stars that have migrated greatly ($|R - R_{form}| > 2$ kpc, blue dots) and stars that have not migrated much ($|R - R_{form}| \leq 2$ kpc, red dots). Note, we have plotted error bars reflecting Poisson noise for each bin. We note the second component fit for radial bins $R = 7 - 9$ kpc and $R = 9 - 12$ kpc is entirely dominated by star particles that have migrated. We expect that stars that moved from elsewhere combined with stars that were born locally should not naturally conspire to produce a single sech^2 profile.

For the solar cylinder, $R = 7 - 9$ kpc, we find that the model distribution of stars as a function of $|z|$ resembles a double sech^2 profile, with the "transition" height of $|z| \sim 0.75$ kpc, comparable to $\sim$1 kpc found by J08 for the Galactic disk. We have found the best-fit scale heights to be 381 pc and 913 pc, in qualitative agreement with the best-fit scale heights of 270 pc and 1200 pc for the SDSS data (J08). The scale height ratio suggested by the simulation is slightly low — $\sim$2.4, instead of $\sim$3 from the data. Moreover, the simulation's thick disk to thin disk normalization is slightly discrepant — $\sim$0.14, rather than $\sim$0.12 suggested by the SDSS data. Overall, we find that the thick disk in the MW simulation, formed through the process of radial migration, is qualitatively very similar to the observed Galactic thick disk. In contrast, as Figure 2.4 shows, this conclusion does not apply to the LSB simulation.

The median metallicity of the Milky Way disk exhibits a clear vertical gradient (see bottom two panels of Figure 9 in I08). Notably, the spatial variation of the median metallicity does not follow the distribution of the stellar number density (I08). The middle panel of Figure 2.7 shows that the MW simulation reproduces a qualitatively similar metallicity distribution; we note that a constant additive offset of 0.1 dex has been applied to [Fe/H] throughout the simulation so that the median metallicity in the plane of the disk in the

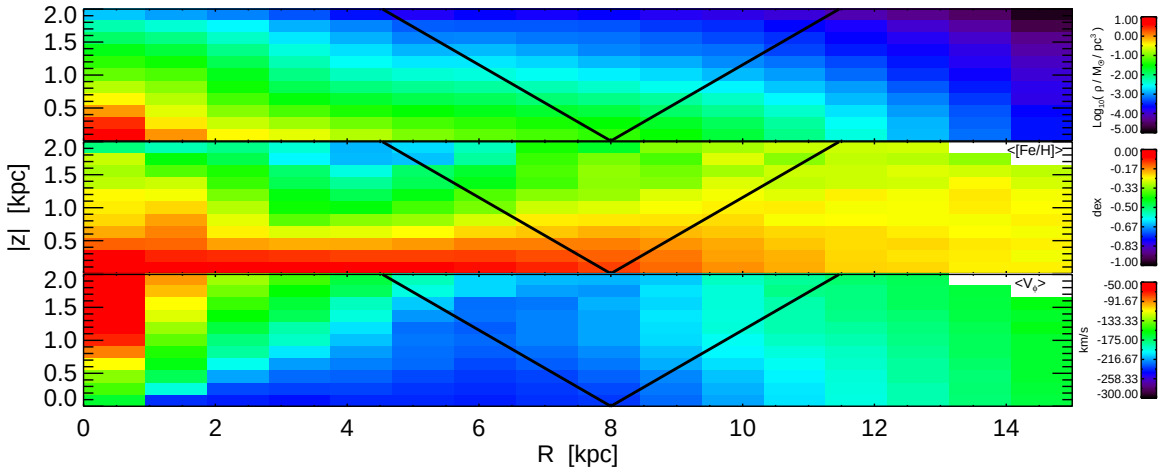

Figure 2.7 Top: Mass density distribution in galactocentric coordinates of the entire MW simulation. The colors scale logarithmically with density in each bin. Overplotted is the SDSS field of view ($|b| > 30°$). Middle & Bottom: Mass-weighted mean [Fe/H] and V_ϕ values as mapped onto the R–$|z|$ plane. For a color box to be plotted in the bottom two panels, we required a minimum of 50 star particles.

solar cylinder matches observations (see metallicity distribution function in R08b). As expected, at low galactic latitudes and small radii, the volume is dominated by high (near solar) metallicities. At higher latitudes the volume is increasingly metal poor.

As with metallicity, previous studies have found a gradient in the median V_ϕ with respect to z in the Milky Way (see Figures 5, 8, and 9 in Bond et al. (2010, hereafter B10), and references therein). These authors concluded that V_ϕ is also well characterized by a non-Gaussian distribution (see Binney, 2010, for the implied distribution function). The bottom panel of Figure 2.7 shows that the MW simulation reproduces qualitatively similar V_ϕ properties, including a $|z|$ gradient.

Thus on a gross scale the MW simulation qualitatively matches patterns observed in mass density, metallicity and rotational velocity in the Milky Way disk. We now look at the solar cylinder in greater detail.

2.5 Effects of Radial Migration on the Solar Cylinder

2.5.1 Vertical Gradients

Here we study in detail the distributions of age, stellar density, rotational velocity and metallicity as functions of $|z|$ for the solar cylinder. To be consistent with the analysis of high galactic latitude SDSS data by J08 and I08, we select model particles from an annulus with 7 kpc $\leq R \leq$ 9 kpc. This radial cut spans 2.8–3.6 scale lengths from the center of the model (scale length 2.5 kpc), and covers the Sun's location of $\sim$3 disk scale lengths from the Milky Way center (scale length $\sim$2.6 kpc) (see bias-corrected value, Table 10, J08).

The behavior of the MW simulation in this particular volume is illustrated in Figure 2.8. The top panel shows the age distribution as a function of $|z|$. As expected, near the midplane, the population is dominated by young stars, and the mean age monotonically increases with increasing distance from the midplane. Only very old stars are found at large $|z|$: by $|z|$ $\sim$0.5 kpc the mean age is already $\sim$5 Gyr. Recall that Figure 2.3 shows that with increasing distance from the midplane, the stellar population becomes dominated by older stars that formed closer to the center of the disk. These two figures taken together give a coherent picture of the net dynamic effect on the system: *on average stars move both radially outward and away from the midplane over time.*

Radial migration is able to change the extent of a star's vertical oscillation, as well as its rotational velocity (middle panel, Figure 2.8). In the MW simulation we find the rotational velocity slows by 18 $\mathrm{km\,s^{-1}}$ for every kpc. (roughly comparable to the gradient of -30 $\mathrm{km\,s^{-1}\,kpc^{-1}}$ found by I08). Note that stars which significantly lag the rotation of the disk in the midplane have traditionally been regarded as members of the thick disk.

Another observed trend that is physically well motivated by the net outward and upward movement of stars over time is the decline of metallicity with increased height (bottom panel, Figure 2.8). In the MW simulation, the metallicity distribution changes with $|z|$ with a best-fit gradient of $\sim$0.18 $\mathrm{dex\,kpc^{-1}}$, again in qualitative agreement with the measured value for the Milky Way of $\sim$0.30 $\mathrm{dex\,kpc^{-1}}$ (I08).

To understand how this trend arises, recall that the top panel of Figure 2.8 shows that the stellar population away from the plane is dominated by old stars. As Figure 2.3 shows,

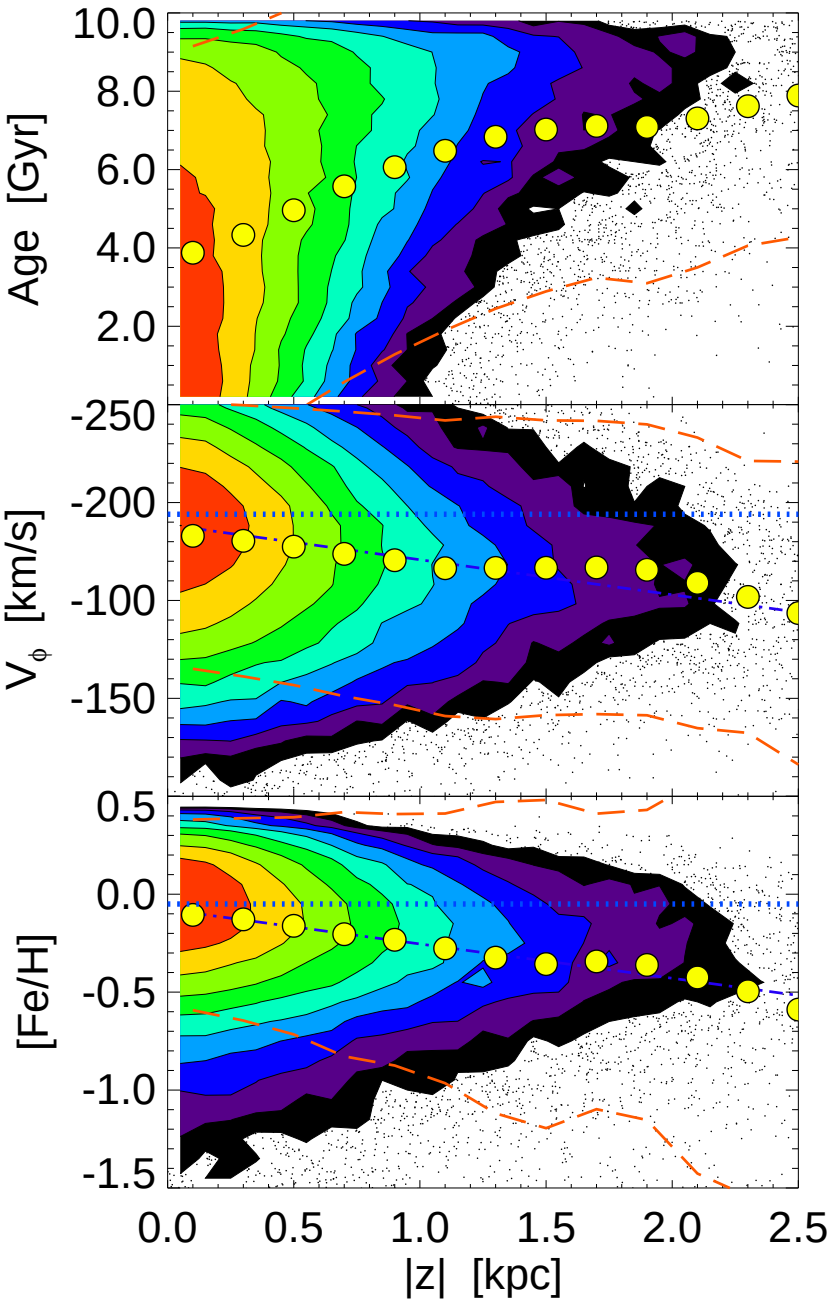

Figure 2.8 The properties of $\sim$200,000 model particles selected from a galactocentric cylindrical annulus with 7 kpc $< R <$ 9 kpc. Age, rotational velocity, and metallicity are shown as a function of height in the top, middle, and bottom panels respectively. The data are represented by color-coded contours (low to medium to high: black to green to red) in the regions of high density, and as individual points otherwise. The large symbols show the weighted mean values in $|z|$ bins, and the dashed lines show a 2σ envelope around the weighted means. The dot-dashed line shows the best linear fit to these means. Overplotted for reference in a dotted blue line is the mean rotational velocity and mean metallicity at $z = 0$ in the MW simulation.

the oldest stars at large $|z|$ mostly formed in the inner $2-4$ kpc. Moreover, at early times, the radial metallicity gradient was steep (see Figure 2 in R08b); stars that are now in the thick disk in the solar cylinder in the MW simulation were once at the outer edge of the forming thin disk and hence formed at a low metallicity. As a result, stars that formed at a radius of $2-4$ kpc early on in the galactic history are necessarily metal poor. These stars have been subsequently moved out and up over time. At later times, the metallicity gradient flattened out as the disk grew. Again, looking at Figure 2.2 (top right panel), one can see a significant fraction of young stars (*i.e.* less than 4 Gyr old) formed at R $\sim$6 kpc where there was a relatively more metal rich ISM. These stars had less time to migrate and as a result remain closer to the midplane of the disk. This complex co-dependence of radial migration, birth location, and metallicity gradient evolution then gives rise to a vertical metallicity gradient in the solar neighborhood.

2.5.2 Thin/Thick Disk Transition

We turn our attention now to a particular region within the solar cylinder: $|z| = 0.5-1.0$ kpc, $R = 7-9$ kpc. This region in the simulation is analogous to the thin–thick disk "transition zone" considered by I08: within this volume a roughly equal number of thin and thick disk stars is expected (see bottom left panel, Figure 2.6). The transition region within the MW simulation occurs in approximately the same place as in the data (0.75 kpc versus ~ 1 kpc) which allows us to draw a direct comparison to the slice analyzed in I08. We show here that all the trends observed in the SDSS data can be explained by a continuous distribution rather than two distinct populations.

In Figure 2.9 we show the distribution of observable properties as a function of age within this slice of the simulation. The top left panel of Figure 2.9 shows the distribution of ages in this thin volume slice: the region is well populated ($\sim$30,000 star particles) and predominantly old (36% older than 7 Gyr, 63% older than 5 Gyr). The remaining panels in Figure 2.9 illustrate probability densities of formation radius, metallicity, and rotational velocity versus age. In all cases, the distributions do not suggest distinct populations. For the given $|z|$ slice, stars older than about 4 Gyr are both numerous and formed significantly

interior to their present location (top right panel). These stars also show a rotational velocity lag of $\sim$20 km s^{-1}, as shown in the bottom left panel. The oldest stars, those with ages ≥ 8 Gyr, have significantly lower metallicities than younger stars (bottom right panel). And as noted previously, the oldest stars formed at a range of interior radii, when the ISM metallicity was low and had a steep radial gradient. These effects drive the behavior of various observables, as discussed next.

2.5.3 Rotational Velocity vs. Metallicity

We have shown in section §2.5.1 that the MW simulation yields vertical trends in metallicity and rotational velocity similar to those found in SDSS observations presented in I08 & B10. SDSS data also revealed a surprising lack of strong correlation between V_ϕ and [Fe/H], contrary to the expectations based on a traditional two-disk model (see Appendix 2.10 for a discussion of an observational claim that a weak correlation does exist for $-1 <$[Fe/H]< -0.5). In the top left panel of Figure 2.10, we show V_ϕ vs. [Fe/H] for the vertical slice considered above ($|z| = 0.5 - 1.0$ kpc) corresponding to the transition between the thick and thin disk in the simulation. The MW simulation also yields a lack of strong correlation between these quantities: although both rotational velocity and metallicity show robust vertical gradients, when stars are selected from a thin z slice, the correlation between velocity and metallicity is much weaker.

We can understand why there is no strong correlation between V_ϕ and [Fe/H] if we consider the thin slice as occupied by an age ensemble that was brought together by radial migration. In this light, we can decompose the sample by age to see how the behavior of each population is modified with time (see top left panel of Figure 2.9 for the age sub-samples considered).

The top right panel of Figure 2.10 shows a strong correlation between rotational velocity and metallicity exists for young stars; the gradient is -71 km s^{-1} dex^{-1} (more metal-rich young stars rotate more slowly). The young stars constitute a small fraction of the overall population in the selected volume (10%) and, as the top right and bottom right panels of Figure 2.9 illustrate, young stars have correlated metallicity and formation radius. Thus if

a young star has a metallicity different than the surrounding ISM, it must originate from somewhere other than the solar cylinder and be at or near perigalacticon (if $R_g \geq 9$ kpc, where R_g is the radius of the stellar guiding center) or at or near apogalacticon (if $R_g \leq 7$ kpc); consequently, it will either lead or lag the local standard of rest (LSR).

For increasingly older age bins, the gradient diminishes and ultimately fades away. The bottom left and right panels of Figure 2.10 show V_ϕ vs. [Fe/H] for intermediate (4 Gyr $\leq$ Age $\leq$ 6 Gyr) and old (8 Gyr $\leq$ Age $\leq$ 10 Gyr) populations respectively. The intermediate age stars constitute 24% of the stellar population in the thin slice and retain a slight gradient $= -19$ km s^{-1} dex^{-1}. The oldest stars make up 21% of the stellar population and show a nearly flat/slightly positive slope of 8 km s^{-1} dex^{-1}.

The peak in the distribution of intermediate and oldest age star particles is offset to progressively lower metallicity and rotational velocity. The metallicity of intermediate age stars is in the range $-0.5 <$ [Fe/H] < 0.5 while that of old stars is $-1.0 <$ [Fe/H] < 0.0. We can think of these three age bins as dominating different portions of the overall V_ϕ vs. [Fe/H] space, with the peak of intermediate and old stars being perpendicular to the correlation for young stars.

The mean peak value of the oldest stars is [Fe/H]$= -0.5$, $V_\phi = -210$ km s^{-1}; this is significantly lower than the mean peak value of the full age sample [Fe/H]$= -0.1$, $V_\phi = -225$ km s^{-1}. The full age sample's mean peak value matches the intermediate age values, which is in turn lower than the mean peak value of the youngest stars [Fe/H]$= -0.05$, $V_\phi = -245$ km s^{-1}. When the entire population is considered as a whole, the correlation becomes much weaker.

Why does the V_ϕ-[Fe/H] gradient diminish with increasing age? To understand this, we return to Figure 2.9 and recall that most of the stars within this thin cut are intermediate to old age, and they did not form within 7 kpc $\leq R \leq 9$ kpc. A range of formation radii corresponds to a range of formation environments; this maps to a range of metallicities for stars of a given old age bin. At the same time, depending on a star's formation location and subsequent migration and scattering off the disk substructure, it can end up with a range of possible rotational velocities (see bottom left panel, Figure 2.9). Hence, even a single old age bin samples a wide range of formation environments and metallicities, in addition to a

wide rage of rotational velocities resulting from unique dynamical histories, which are not directly correlated.

We stress the significant difference between these results and the traditional two-disk interpretation: in the latter case a correlation between V_ϕ and [Fe/H] is expected in an older, metal poor, thick disk population. In contrast, here we find that a trend is present in the young stars but absent in the older stars. The trend in the young stars can be easily understood as arising from epicyclic motions of stars with their birth radii imprinted into their metallicities. As migration moves the guiding centers of stars, this metallicity encoding is erased, and the correlation between V_ϕ and [Fe/H] disappears.

2.5.4 Geneva Copenhagen Survey

As we demonstrated above, we can understand why there is no strong correlation between V_ϕ and [Fe/H] when we decompose the sample by age. Older populations have had more time to radially mix; thus in the older age bins the expected trend is much weaker. That is, the evolution of the trends shown in Figure 2.10 is a unique signature of radial mixing taking place in the disk.

We can verify whether this is the case in the solar neighborhood by utilizing observational data taken from the Geneva-Copenhagen Survey (GCS) (Holmberg et al., 2009). The GCS samples a wide range of stellar ages and is reasonably well populated with old stars to make qualitative comparisons to the MW simulation in the plane of the disk. Because stellar age estimates are fairly uncertain, we compare only the lowest and the highest thirds of the GCS distribution. While what we have shown in Figure 2.10 is the relationship at 0.5-1 kpc above the plane, these trends evolve in the same way as a function of age in the mid-plane.

We have selected the non-binary stars from the GCS and repeated the analysis we presented above. Figure 2.11 shows the results: the top panel shows that there is no net trend when the sample is considered as a whole. Splitting the sample into two broad age bins (0-3 Gyr and 6-15 Gyr) yields a trend only in the young stars – the correlation is absent for the older stars. The evolution of the observed V_ϕ vs. [Fe/H] trend in the GCS sample therefore matches our expectations based on the simulation and suggests that the stellar

populations in the solar neighborhood have been influenced by radial mixing.

2.6 Observational Decomposition

We now turn our attention to assigning thin or thick disk membership in a manner analogous to observational studies, i.e. either based on kinematics or metallicity. We find that classifying stars as members of the thin or thick disk by either velocity or metallicity leads to an apparent separation in the other property, as observed.

2.6.1 Membership Based on Kinematic Criteria

One of the observational differences between *kinematically selected* thin and thick disk stars is that the latter have higher abundance of α elements at a given [Fe/H] (Bensby et al., 2005; Feltzing, 2006, and references therein). This difference is often interpreted as evidence for different formation histories. Our simulations include a calculation of the oxygen abundance following the prescription by Raiteri et al. (1999); given that SNII mostly yield oxygen (Hoffman et al., 1999), we use oxygen as a proxy for all α elements. Because metal yields are not precisely known, the absolute values for [α/Fe] within the MW simulation does not match the Milky Way. However, we believe the relative differences in [α/Fe] to be qualitatively accurate; thus the MW simulation gives a good qualitative perspective on distributions in [α/Fe] space within the solar cylinder.

The top left panel of Figure 2.12 shows the overall dependence of [α/Fe] on [Fe/H] for $R = 7 - 9$ kpc, $|z| = 0.0 - 0.3$ kpc (*i.e.* the "solar neighborhood")[2]. A similar behavior is seen for the stars at $|z| \sim 1$ kpc in agreement with Bensby et al. (2005). When the same sample is separated by age, distinct portions of the parameter space are covered. In particular, at low [Fe/H], old stars show an enhancement of [α/Fe] relative to young stars.

Locally, observed thick disk stars are selected kinematically, rather than by age (Prochaska et al., 2000; Reddy et al., 2003, 2006; Allende Prieto et al., 2004). We reproduce the qualitative behavior of observations by following similar steps with the MW simulation. The

[2]Note that the low-[α/Fe], low-metallicity stars are not observed, and are here likely a result of the fact that our gas is initialized with zero metallicity

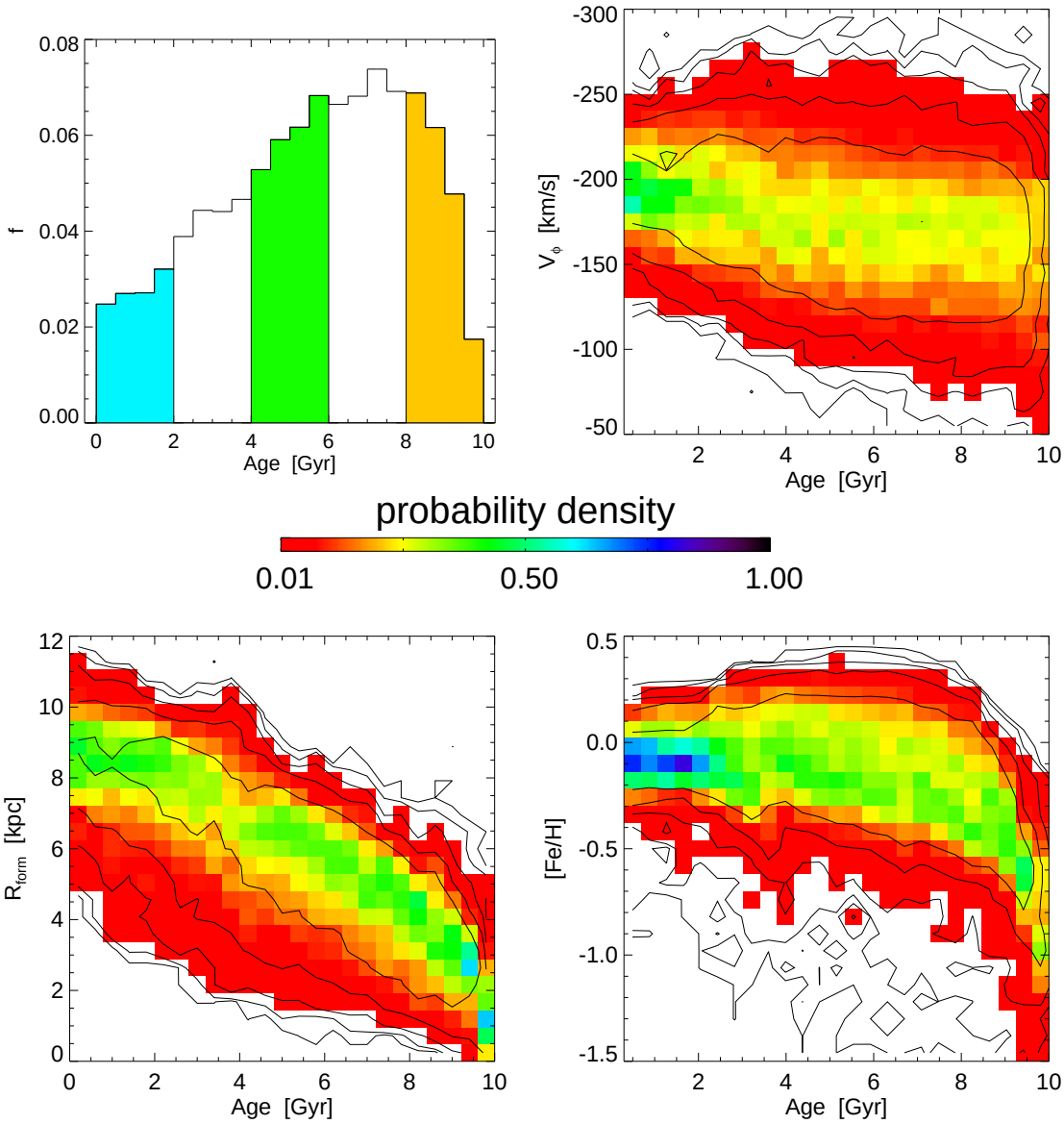

Figure 2.9 Top left: histogram of stellar ages for subset of data from within thin slice spanning $|z| = 0.5 - 1.0$ kpc, $R = 7 - 9$ kpc; shaded regions correspond to age slices considered in Figure 2.10. The remaining three panels illustrate probability density maps with logarithmically spaced contours overplotted; here each column sums to 1. Clockwise from top right: formation radius, metallicity, and rotational velocity as a function of age. Note, the bottom left panel is the same considered in the top right panel in Figure 2.2.

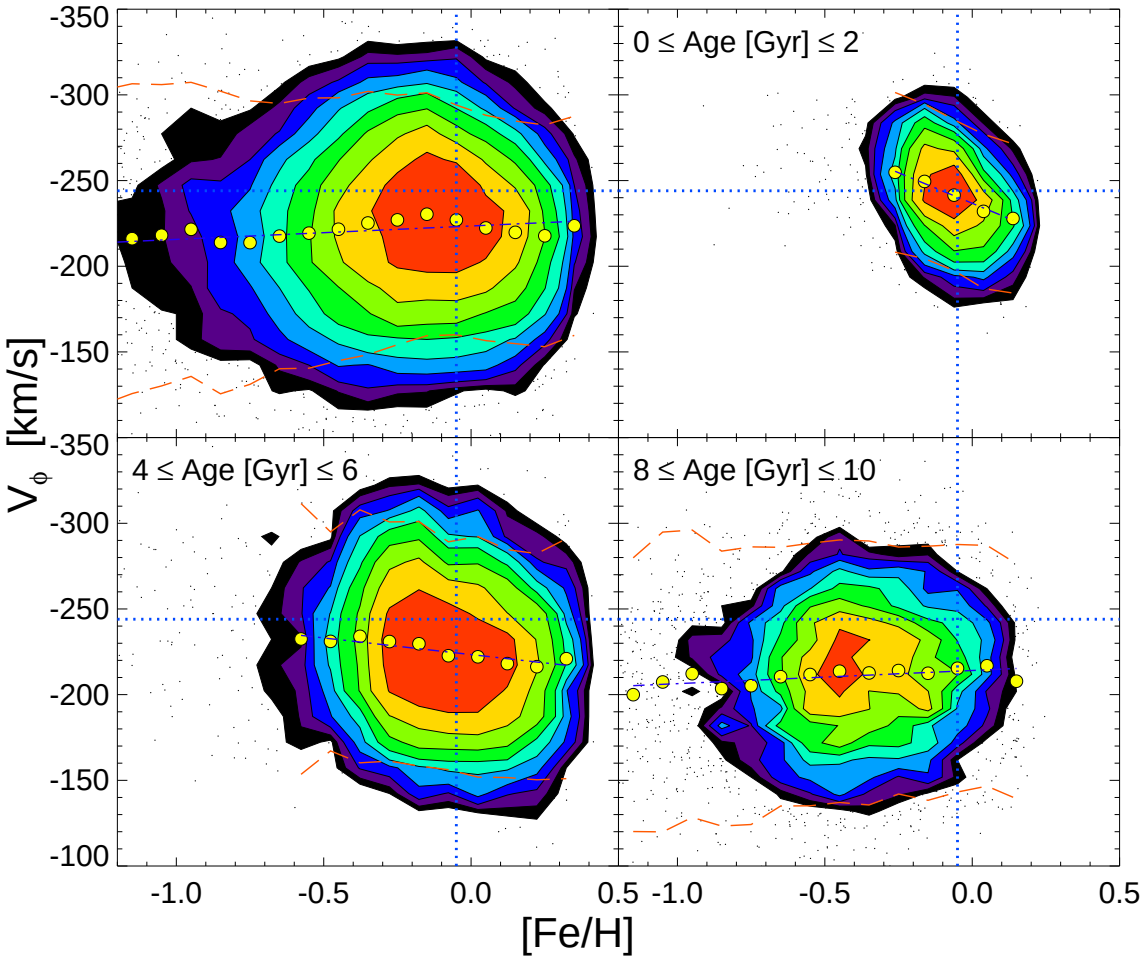

Figure 2.10 Decomposition of rotational velocity vs. metallicity by age. Top left figure, rotational velocity vs. metallicity for all stars within thin slice $|z| = 0.5 - 1.0$ kpc, $R = 7 - 9$ kpc. Rotational velocity and metallicity are not correlated. Top right, bottom left, and bottom right panels show stars with ages 1, 5, 9 Gyr ± 1 Gyr respectively. Overplotted for reference with dotted blue lines is the mean rotational velocity and mean metallicity of the gas within the MW simulation's solar cylinder. As the top left panel of Figure 2.9 illustrates, the youngest stars are a small fraction of the overall mass distribution; however, these stars show a clear trend of lower metallicity at higher rotational speed. This trend diminishes and eventually disappears for increasingly older stars.

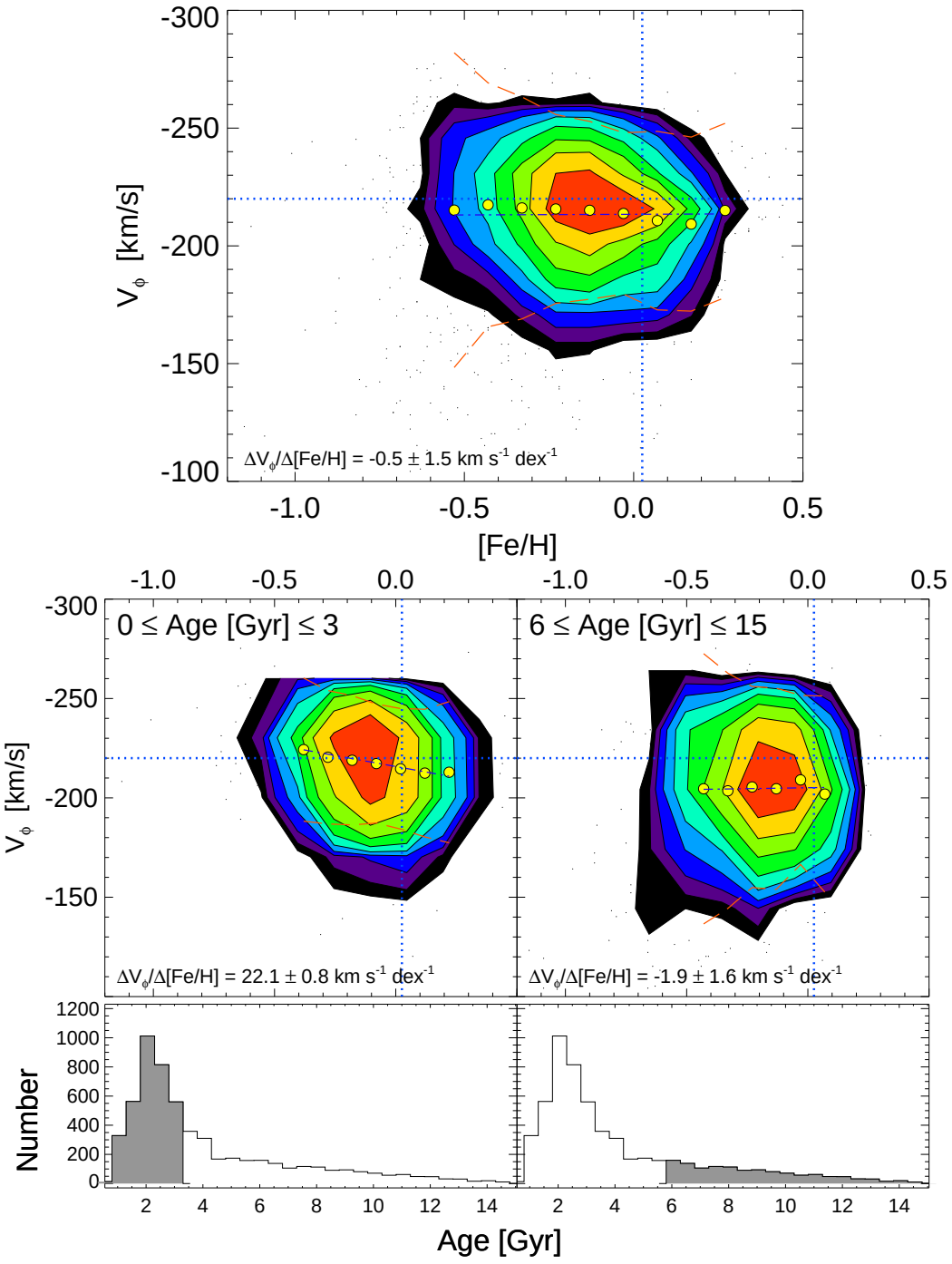

Figure 2.11 V_ϕ vs. [Fe/H] for stars from the Geneva Copenhagen Survey (GCS). We have repeated the analysis we presented in Figure 2.10 for all GCS stars flagged as non-binary. Top panel: when the sample is considered as a whole (5740 stars), there is no discernible trend. Middle row: the sample split into two broad age bins: Age = 0-3 Gyr (3114 stars) and Age = 6-15 Gyr (1227 stars). Left middle panel, the young stars show a trend, while in the right middle panel, the old stars are not correlated. This result agrees with the prediction from the MW simulation and hints at a history of radial mixing in the solar neighborhood. Bottom panels: histogram of overall age distribution, with shaded region corresponding to the data sampled in the panel above it.

top right panel in Figure 2.12 shows a Toomre diagram for simulated stars, with selection cuts motivated by Nissen & Schuster (2009). The bottom left panel shows that these kinematically-selected thin and thick disk stars from the solar neighborhood show similar bifurcation of [α/Fe] vs. [Fe/H] behavior as young and old subsamples shown in top left panel. In the bottom right panel, stars from just the shaded [Fe/H] cut in the bottom left plot are examined.

Stars falling within the kinematically selected thick disk region have a higher fraction of old stars relative to the overall population. These old stars are α-enhanced as they formed in the interior of the disk and radially migrated to their present location. Thus kinematically dividing the stars locally yields a sample that is older and α-enhanced. Although the simulation and the data are not in detailed quantitative agreement, these qualitative results imply that the differences in [α/Fe] vs. [Fe/H] for kinematically selected thin and thick disk stars may be another consequence of mixing effects that result from radial migration.

2.6.2 Membership Based on [α/Fe] Criteria

Although not as commonly done, it is equally plausible to take the converse approach; we can assign membership to the thin and thick disk based on an [α/Fe] cut and then study the kinematic and [Fe/H] distributions that result (Navarro et al., 2010; Lee et al., 2010). Here we follow the technique outlined by Lee et al. (2010), who chemically divided the Galactic disks using SDSS SEGUE-1 data; we select star particles within $R = 7 - 11$ kpc, $|z| = 0.3 - 2.0$ kpc and split them so that stars with [α/Fe] ≥ -0.1 are assigned thick disk membership.

Assigning membership based on [α/Fe] effectively divides the disk into two populations: old stars and young-intermediate age stars, as can be seen clearly in the top left panel of Figure 2.13 (see also Schönrich (2010); Haywood (2008)). Why is this the case? Star particles are born α-enhanced if they form in a region with a high local SFR and little SNIa pollution. Since most old stars originated near the center of the disk, and that region is where the SFR was high, these stars are naturally α-enhanced.

We compare our results to three trends discussed in Lee et al. 2010: the radial metallicity

gradient, distribution in V_ϕ and distribution in [Fe/H], which we show clockwise from top right in Figure 2.13. The top right panel illustrates the best fit radial metallicity gradients as derived from the mass weighted mean value of [Fe/H]. Cutting by [α/Fe] results in no trend (slope $\sim$0 kpc dex^{-1}) in the thick disk and a negative trend in the thin disk (slope ~-0.2 kpc dex^{-1}); this is similar to the thick disk slope = 0 kpc dex^{-1} and thin disk slope = -0.3 kpc dex^{-1} observed by Lee et al. (2010). The bottom right panel illustrates the cumulative V_ϕ distributions that result for the MW simulation when stars are separated by [α/Fe]: the thin and thick disk trends are offset by $\sim$22 km s^{-1}, which is qualitatively similar to, if quantitatively smaller than, the $\sim$50 km s^{-1} offset found by Lee et al. (2010). Finally the bottom left panel shows the cumulative [Fe/H] distributions; we find the thin and thick disk trends offset by $\sim$0.35 dex, not dissimilar from the observed $\sim$0.4 dex offset (Lee et al., 2010).

Therefore, by adopting a kinematic or [α/Fe] selection criteria used by observers, we are able to reproduce an apparent separation in the other property, despite the fact that there are no distinct populations in the model galaxy.

2.7 Comparison with Previous Work on Radial Migration

Recently, Schönrich & Binney (2009a,b) investigated how radial migration and chemical evolution shape the solar neighborhood, by incorporating for the first time a prescription for radial migration in a semi-analytic model of Galactic chemical evolution. Their model represented a disk in which star formation commenced at all radii simultaneously (*i.e.* without inside-out growth), with radially varying star formation rates set to yield a disk with an appropriate scale length. The guiding center radii of the stars in their model changed (*i.e.* stars migrated radially) according to a parametrized probabilistic prescription whose normalization was left as a free parameter in the model. The vertical structure of their disk was determined based on the assumption that locally coeval stars comprise an isothermal population with a velocity dispersion given by observational constraints. Because stars migrating from the inner disk retain their velocity dispersions but encounter a lower restoring potential in the outer disk, they populate the disk away from the plane. Hence, Schönrich & Binney (2009b) showed that a thickened component is a natural consequence of radial

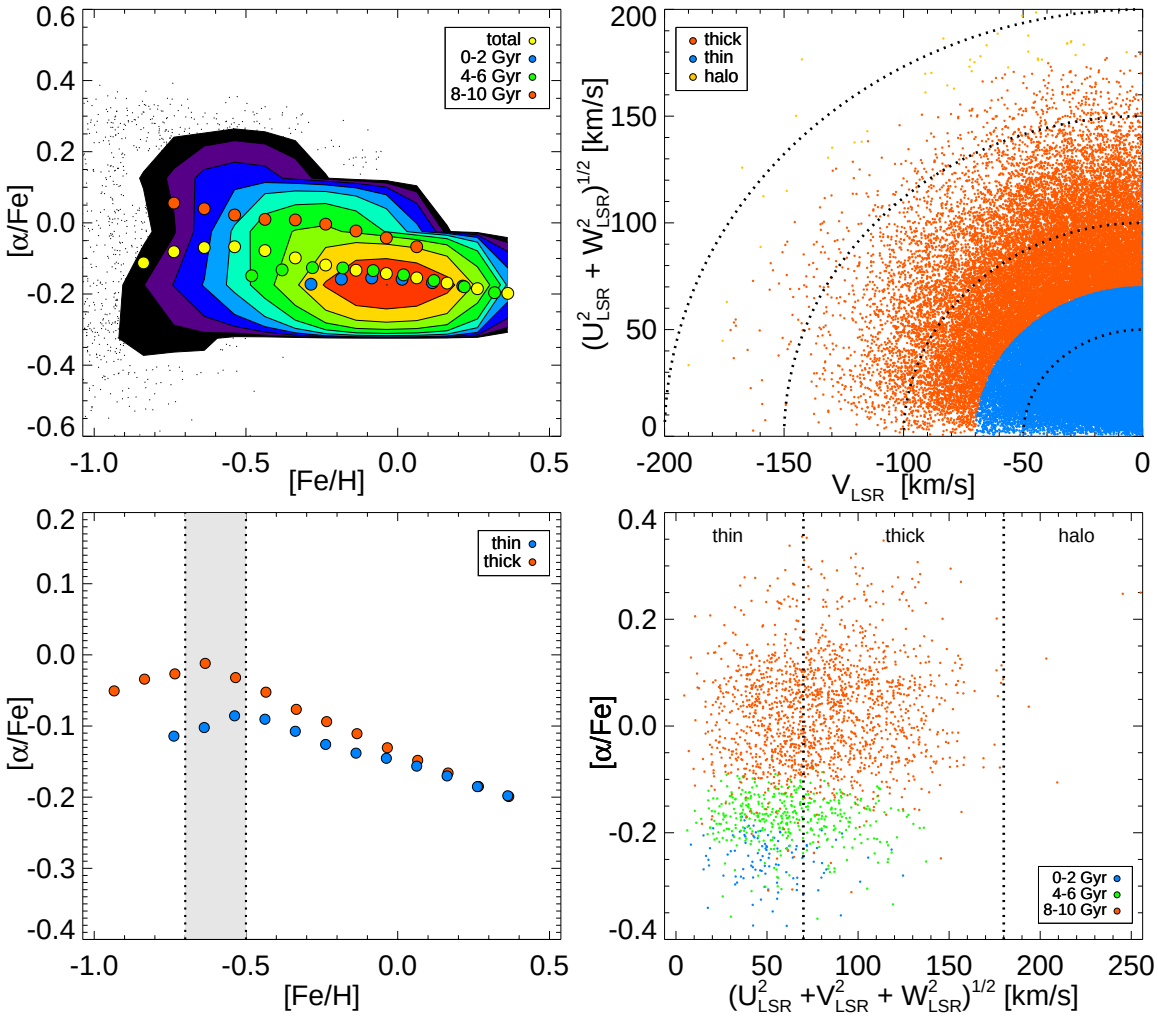

Figure 2.12 Results of a simple kinematic cut on the local sample: $R = 7 - 9$ kpc, $|z| = 0.0 - 0.3$ kpc. Top left: Distribution of [α/Fe] for the entire local sample. The distribution is continuous, not bimodal. The mean [α/Fe] for [Fe/H] bins, shown in yellow, qualitatively matches observational data (Bensby et al., 2005). When the sample is decomposed by age, the weighted mean value of old stars is clearly α-enhanced relative to the younger populations. Top right: Toomre diagram. Stars with $V_{LSR} \geq -70$ km/s are assigned thin disk membership, while stars with $-150 \leq V_{LSR} < -70$ km/s are considered thick disk. All other stars are assigned halo membership in agreement with Nissen & Schuster (2009). Bottom left: the resulting weighted mean distributions for the thin and thick disk populations. The thick disk is α-enhanced relative to the thin disk at low [Fe/H]. Bottom right: stars from just the shaded [Fe/H] cut in the bottom left plot. Stars falling within the "thick" disk zone have a higher fraction of old stars relative to the overall population. These old stars are α-enhanced. Thus kinematically dividing the stars locally biases the sample to an older, α-enhanced population.

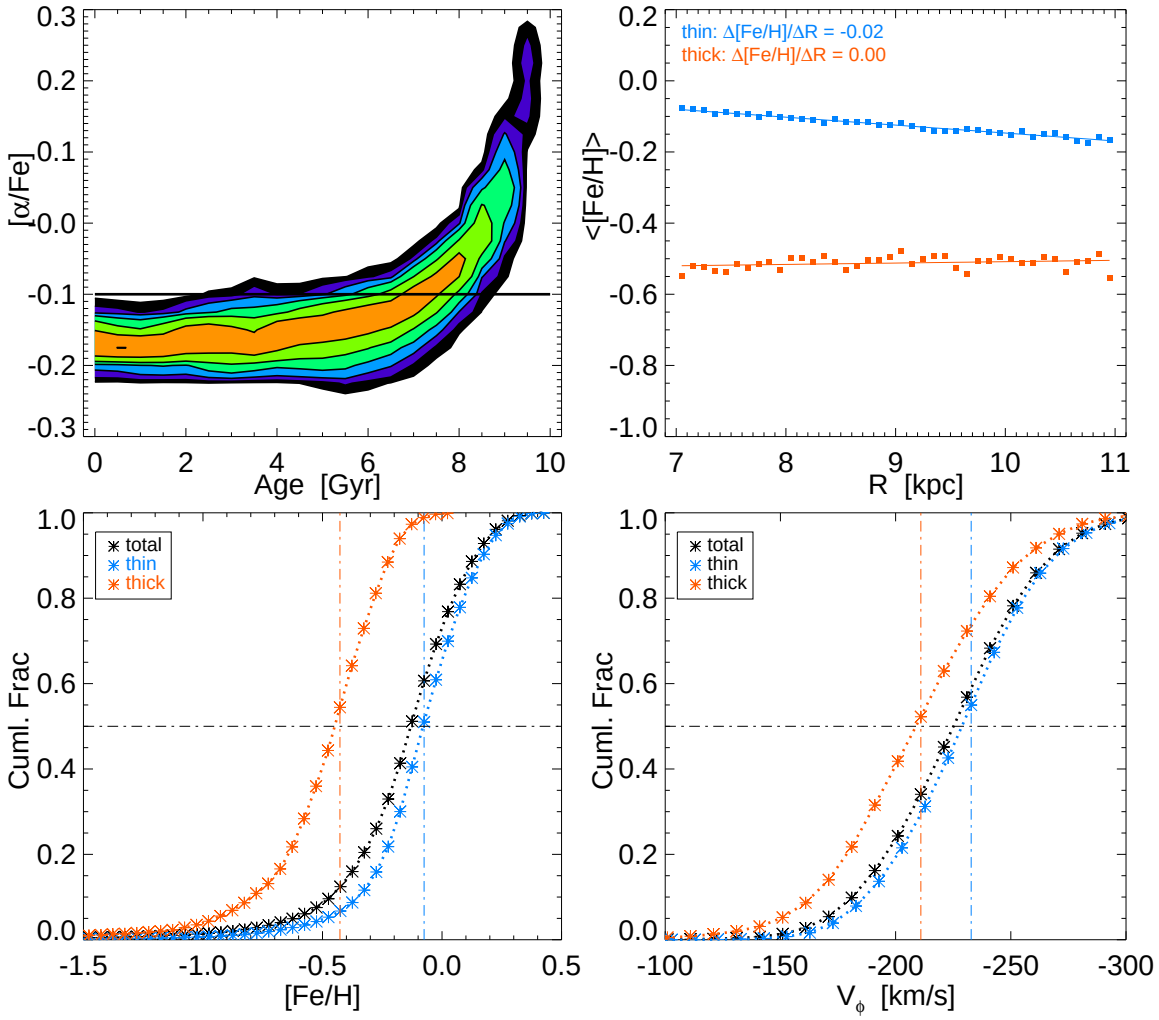

Figure 2.13 Thin and thick disk membership assigned based on [α/Fe]; the sample includes star particles within $R = 7 - 11$ kpc, $|z| = 0.3 - 2.0$ kpc. Top left: mass-weighted contour plot of [α/Fe] *vs.* Age in logarithmically spaced bins (low to medium to high: black to green to orange). Overplotted for reference is the dividing line [α/Fe] $= -0.1$; stars with [α/Fe] ≥ -0.1 are considered α-enhanced and are assigned thick disk membership. Clearly the majority of these stars are quite old. Stars with [α/Fe] < -0.1 are considered thin disk members and sample a wide range of ages. Counterclockwise from top right to bottom left: resulting thin and thick disk trends. Notably, the thick disk stars are metal-poor with no gradient in R and lag the rotation of the thin disk stars. Despite the appearance of these trends here, there is no distinct thick disk population in the MW simulation.

migration, and by fitting the model they also reproduced many of the canonical features of the thick disk (*i.e.* enhanced [α/Fe] ratios, older ages, lower metallicities, rotational lag), similar to what we have shown in the previous Section.

It is therefore reassuring that our results presented here agree qualitatively with those of Schönrich & Binney (2009b), given that our modeling methods are entirely different, and that our model was not specifically tuned to the Galaxy. However, we also find subtle yet crucial differences. Figure 4 of Schönrich & Binney (2009b) shows that due to radial mixing, a population that shares the same average rotational velocity can show immense variations in its chemical composition. The top left panel of Figure 2.14 shows that our model also yields stellar populations with the similar average rotational velocities but very different chemistry. However, we note the contours of mean V_ϕ in this plane have a different orientation in our simulation compared to those shown in Fig. 4 of Schönrich & Binney (2009b), even though the age structure is very similar; at fixed [Fe/H] age increases monotonically with rising [α/Fe] (middle panel of Figure 2.14 and Figure 5 of Schönrich & Binney 2009b).

A hint of a reason for this discrepancy is provided by scrutinizing the metal-rich end of these figures. In our model, the [α/Fe]-deficient metal-rich population originated in the interior of the disk (see the bottom left panel of Figure 2.14) and has migrated to the present radius without very much heating. This is apparent from the fact that the mean V_ϕ for this population is only very slightly lagging the LSR ($\sim$$-240$ km s^{-1}). On the other hand, in the model of Schönrich & Binney (2009b), that same population shows considerable lag from the LSR. This discrepancy implies that there are qualitative differences in the treatment of radial mixing between their prescription and our simulation.

The differences in the velocity structure in this plane must also be a result of the assumption in the Schönrich & Binney model that the entire disk begins forming stars at once with a peak in star formation occurring $\sim$10 Gyr ago everywhere. In our model, it is impossible to have an old metal poor star which formed at the solar radius - *all* of these stars must have migrated to their present position because the solar neighborhood in our simulation does not exist $\sim$9 Gyr ago.

In an observational study, Haywood (2008) argued that the existing solar neighborhood samples (*e.g.* the GCS) show signatures of radial mixing as proposed by Sellwood & Binney

(2002). In our sample shown in Figure 2.14, the metal-poor, low [α/Fe] stars have high velocities and young ages, and are at or near perigalactic passage from the outer disk into the solar neighborhood sample. This is consistent with the arguments put forth by Haywood (2008) as observational evidence of radial mixing. However, we point out that the large velocities of this tail in the distribution signify that their orbits have merely been heated, and these stars have not migrated via the corotation scattering mechanism over any significant distance. Instead, it is the presence of significantly metal-enriched stars on kinematically cool orbits that should be considered as clear evidence of migration.

2.8 Model Tests for Upcoming Surveys

We have demonstrated that we can understand the observed V_ϕ, [Fe/H], and [α/Fe] distributions as a consequence of radial migration effects; the significance of these effects became clear when we decomposed the MW simulation within the solar cylinder by age. Unfortunately age is not easily accessible observationally. However, α is a directly measurable quantity and, as we have shown, for the oldest stars, α-enhancement is a reasonable proxy for age (see top left panel of Figure 2.13, as well as Schönrich 2010; Haywood 2008). Thus we now reassess the relationship between V_ϕ and [Fe/H] by decomposing Figure 2.10 in cuts of [α/Fe] so that we present testable model results for upcoming observational surveys.

Figure 2.15 shows V_ϕ *vs.* [Fe/H] for the "transition zone" considered in Section 2.5 ($|z| = 0.5 - 1.0$ kpc, $R = 7 - 9$ kpc), as split by two broad bins in [α/Fe]. Below each V_ϕ *vs.* [Fe/H] plot is a histogram of the ages represented in the given bin. In the right panel, the high [α/Fe] sample contains exclusively old stars (99% older than 7 Gyr); the corresponding V_ϕ *vs.* [Fe/H] figure shows a weak positive trend between the quantities (best fit slope $\sim -14\,\mathrm{km\,s^{-1}\,dex^{-1}}$ for $-0.8 <$[Fe/H]< 0; when the fit is restricted to [Fe/H]< -0.5, the slope is steeper and more consistent with the results from Spagna et al. (2010)). In contrast, the low [α/Fe] bin, shown in the left panel, has few old stars (5% older than 7 Gyr) while sampling young to intermediate aged stars relatively equally (22% between 0 and 2 Gyr old, and 31% between 4 and 6 Gyr old). Here there is a strong negative trend between V_ϕ and [Fe/H], with an overall best-fit value of $\sim 25\,\mathrm{km\,s^{-1}\,dex^{-1}}$. We note that this [$\alpha$/Fe] decomposition works equally well in the midplane as in the "transition zone."

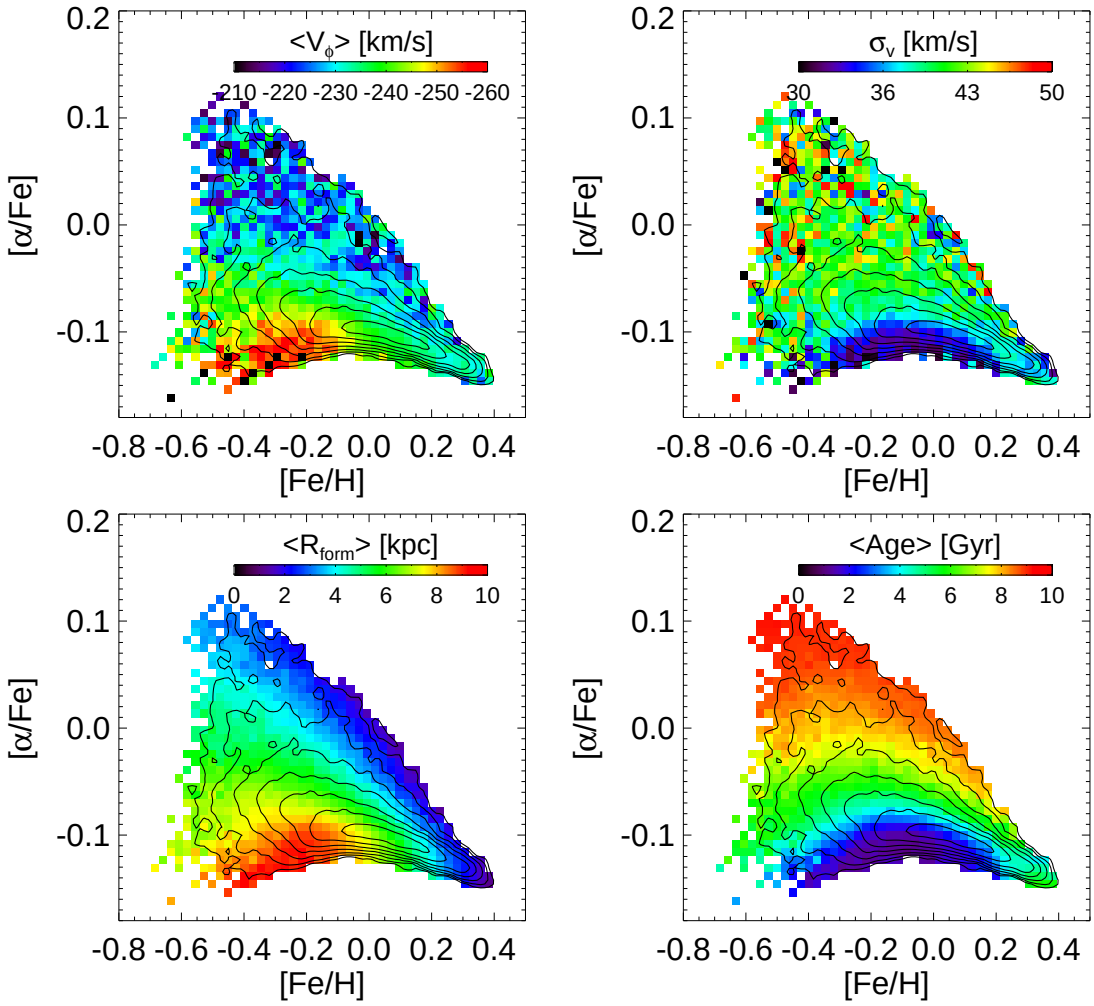

Figure 2.14 The panels clockwise from top left show distributions of mean V_ϕ, age, σ_V, and R_{form} in the [α/Fe] vs. [Fe/H] plane for particles in the midplane ($|z| < 0.3$ kpc) at the solar radius ($7 < R$ [kpc] < 9). The black contours are logarithmically spaced and indicate mass density, while the colors correspond to the mean of the specified quantity. Only cells containing at least 10 particles are shown.

For the low [α/Fe] cut, we have fit the mass-weighted mean values with a single linear fit; however it is equally plausible to fit two lines here, one at -0.6 dex $\leq$ [Fe/H] ≤ -0.2 dex and the other at -0.2 dex $\leq$ [Fe/H] ≤ 0.4 dex. In that case, the linear fit to low [Fe/H] shows no trend while the linear fit to high [Fe/H] shows a strong trend. Notably, the portion spanning low [Fe/H] is dominated by the intermediate aged stars while the portion spanning high [Fe/H] is dominated by a younger population. This "knee" is a persistent feature; when the upper limit on this [α/Fe] cut is lowered, fewer intermediate age stars are sampled, and the knee in the trend shifts to lower [Fe/H]. Note, the trend is evident here because on average the stars in this [Fe/H] space have experienced less radial mixing than older stars within the same spatial volume. Thus, it is possible to recover this signature of radial mixing even in the absence of age estimates, but with knowledge of [α/Fe], [Fe/H], and V_ϕ for an unbiased population of stars located out of the midplane.

We also reconsider here the gradient in V_ϕ as a function of distance from the midplane, as shown by Figure 2.16. As with Figure 2.15, we decompose V_ϕ by cuts in [α/Fe]; we find that each subsample displays a similar slope (9 *vs.* 11 $\mathrm{km\,s^{-1}\,kpc^{-1}}$). When the full sample is considered, the slope is larger (18 $\mathrm{km\,s^{-1}\,kpc^{-1}}$) because, in addition to the intrinsic slope, there is also transition from thin disk to thick disk, with the latter having a velocity lag of 19 $\mathrm{km\,s^{-1}}$. Thus, we suggest that if radial migration is significant within the solar cylinder, observational data divided by cuts in [α/Fe] should show similar slopes in V_ϕ *vs.* $|z|$, but the mean values in the midplane should be shifted relative to each other.

To date, [α/Fe] measurements have only been accessible for small targeted samples; our initial comparison with a compilation of all currently available data is particularly encouraging (Navarro et al., 2010). We note current work, like that of the SDSS SEGUE collaboration, aims to obtain a large, well-calibrated [α/Fe] data set. We eagerly anticipate the application of cuts on [α/Fe] to an unbiased population of stars that fall within the region considered by I08 or indeed any large sample within the solar cylinder; such an analysis would further elucidate whether radial mixing has played an important role in shaping the distribution of the Milky Way stars over time.

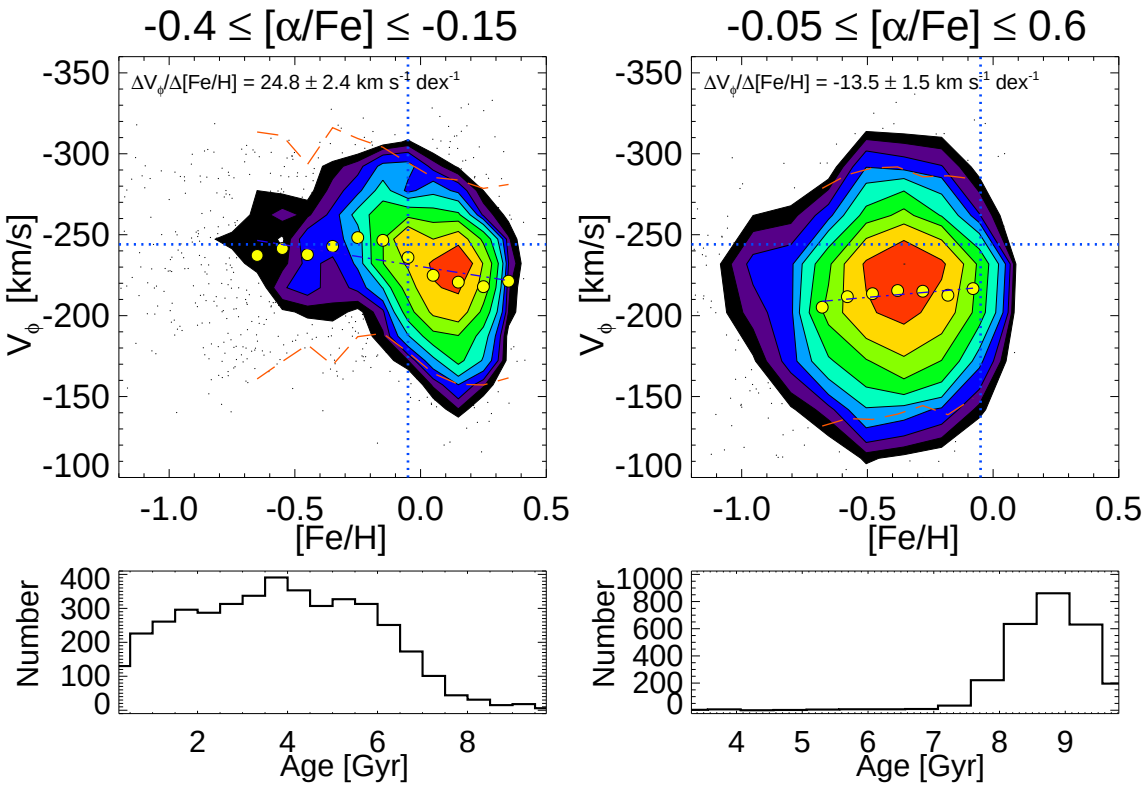

Figure 2.15 V_ϕ vs. [Fe/H] for two broad bins of [α/Fe] for the volume spanning $|z| = 0.5-1.0$ kpc, $R = 7-9$ kpc. Top left panel: $-0.4 \leq$ [α/Fe]≤ -0.15. Note the knee in the distribution at ~ -0.2 dex. Bottom left panel: the distribution of ages sampled by this [α/Fe] cut. Top and bottom right panel: analogous to the left panel but for $-0.05 \leq$ [α/Fe]≤ 0.6. Note the histogram contains only stars older than 7 Gyr old and there is a slight trend in the V_ϕ vs. [Fe/H] figure. This is a clear indication of the importance of radial migration in this volume.

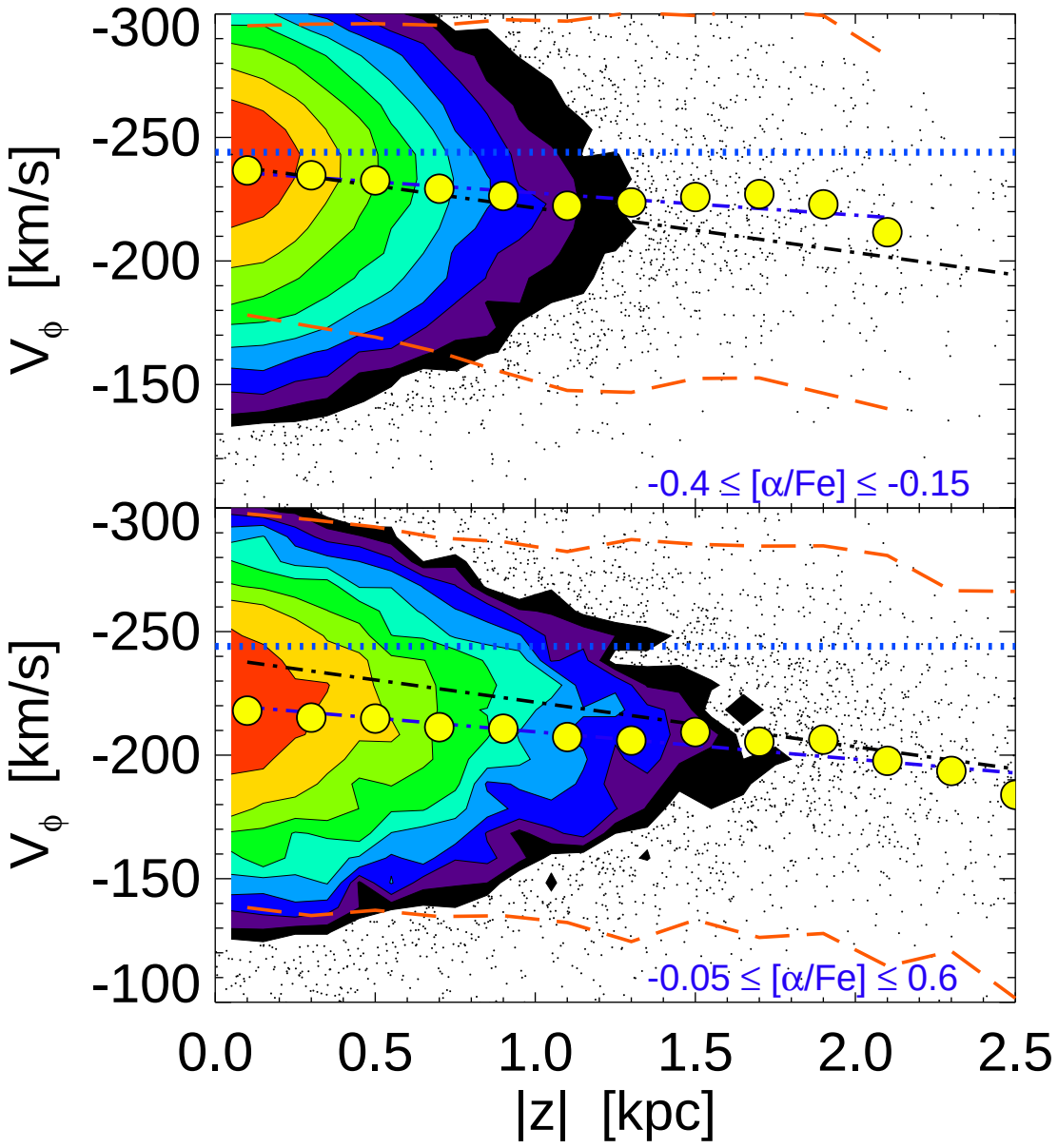

Figure 2.16 V_ϕ vs. $|z|$ within the solar cylinder, $R = 7 - 9$ kpc, represented in a similar fashion to the middle panel of Figure 2.8 but now separated by [α/Fe]. Top panel: Star particles with $-0.4 \leq$ [α/Fe] ≤ -0.15; the mean V_ϕ in the midplane is -237 km s^{-1} with a best fit slope of 9 km s^{-1} kpc^{-1}. Bottom panel: analogous to the top panel, but for $-0.05 \leq$ [α/Fe]$\leq$ 0.6; the mean V_ϕ value in the midplane is -218 km s^{-1} with a best fit slope of 11 km s^{-1} kpc^{-1}. Overplotted in black is the best fit for the overall sample, which has a slope of 18 km s^{-1} kpc^{-1}. We find that when stars are separated by [α/Fe], the gradient is smaller and similar for each subsample despite being shifted by a relative offset.

2.9 Conclusions

We have used an N–body model, designed to mimic the quiescent formation and evolution of a Milky Way–type galactic disk (Roškar et al. 2008ab), to interpret recent SDSS-based observational constraints on the structure of the Milky Way disk. While not a detailed model of the Milky Way, it produces good qualitative agreement with the data and sheds new light on the origin and evolution of the observed disk structure. Of particular importance is the role of radial migration in mixing stars born throughout the disk into the solar neighborhood.

The properties of the Roškar et al. model for the overall spatial, metallicity and kinematic distributions of the Milky Way stars are in qualitative agreement with the SDSS data (Jurić et al. 2008; Ivezić et al. 2008; Bond et al. 2010). While there are quantitative differences in the spatial gradients of these distributions, as well as in their detailed behavior, even this qualitative agreement is remarkable because the simulation was not fine-tuned to match the Milky Way. Not only does the model reproduce the observed change of slope in the counts of disk stars as a function of distance from the Galactic plane (the original motivation for introducing a separate thick disk component), but it also predicts gradients in metallicity and rotational velocity.

The robust qualitative agreements between the data and model predictions motivate the use of model quantities inaccessible to observations, such as the stellar age and the ISM metallicity at the time and position of stellar birth, to interpret recent SDSS results. In particular, the relationship between the metallicity and rotational velocity at $\sim$1 kpc from the Galactic plane can be understood as due to complex interplay between the ISM metallicity at the time and position of stellar birth, and the subsequent secular evolution largely driven by spiral arms.

No *a priori* assumptions about the disk's structure are incorporated in the model and the disk evolves entirely in isolation – yet it reproduces the main observational results which for years have motivated decomposition of the disk into two presumably distinct components. The absence of mergers in this model implies that they are not required to explain the overall disk structure. And while merger remnants are detected within the Milky Way disk (e.g. J08), their influence is apparently well localized. Moreover, even if a primordial thick

disk is present, having formed via accretion/external heating, it is likely to be substantially polluted by migrating disk stars.

The same mixing effects are likely responsible for the observed differences in α element abundance between *kinematically selected* thin and thick disk stars. By adopting kinematic selection criteria used by observers, we are able to reproduce distinctive [α/Fe] vs. [Fe/H] trends similar to those seen in the data, despite the fact that there are no distinct populations in the model galaxy. We find that cutting on [α/Fe] is to a very good approximation to an age cut, particularly for the α-enhanced population; moreover, separating stars into very old and not-so-old components gives rise to all the observed correlations.

We look forward to the improved data derived from the emerging generation of surveys such as SEGUE (Rockosi et al., 2009) and APOGEE (Majewski et al., 2010). Key to garnering a deeper understanding of the importance of radial migration in the Milky Way evolution is gathering both precise age determinations and detailed chemical compositions. We are optimistic that this study will lead to further observational and theoretical work.

2.10 Conflicting Observational Claims

Recently, Spagna et al. (2010) found that the rotational velocity for disk stars is correlated with metallicity for $-1 <$ [Fe/H] < -0.5 at $1 \text{ kpc} < z < 3 \text{ kpc}$ (and no correlation for[Fe/H]> -0.5). Notably, they found a gradient within $40 - 50 \text{ km s}^{-1} \text{ dex}^{-1}$, such that more metal-poor stars rotate more slowly. Their claim is in conflict with several other observational studies (Carollo et al., 2010, I08, B10).

We reconsider the Spagna et al. (2010) findings using SDSS DR7 data to try to understand the differences between these observational findings. We note that a direct comparison between I08 and Spagna et al. (2010) is non-trivial as Spagna et al. (2010) use their own proper motion measurements based on the GSC-II catalog and do not provide a comparison to the Munn et al. (2004) proper motions on a star-by-star basis. Additionally, their color selection is more generous ($0.0 < g-r < 0.9$) than previous studies ($0.2 < g-r < 0.6$, I08). This more generous selection lets in BHB stars, as well as red stars where [Fe/H] reliability decreases. Despite differences in selection criteria, we can reproduce Spagna et al. (2010) results when using the SDSS *spectroscopic* sample (see top panel, Figure 2.17).

While the top panel of Figure 2.17 only considers a narrow bin of $z = 1.0 - 1.5$ kpc, we find the best fit lines are reproducible in other bins as well. Notably, the median V_ϕ as a function of [Fe/H] closely follows the Spagna et al. (2010) result. We also reproduce a bimodal distribution of stars in the metallicity direction, with modes at [Fe/H]~ -0.65 and [Fe/H] ~ -0.4 (see Section 3.2, Spagna et al., 2010).

However, we detect no V_ϕ — [Fe/H] correlation when we consider a complete sample selected in the meridional plane ($l \sim 0\,^\circ$ or $l \sim 180\,^\circ$), where proper motion alone suffices to measure rotational velocity (see bottom panel, Figure 2.17). This sample is essentially complete in selected color-distance limits and thus not subject to strong selection effects present in the SDSS spectroscopic sample. This sample shows negligible dependence of the median V_ϕ on [Fe/H] for [Fe/H]> -1.0 (one can also see the bias due to halo stars for [Fe/H]< -1.0). We note that the slope of the V_ϕ vs. [Fe/H] relation for the spectroscopic sample decreases when using photometric [Fe/H] instead of spectroscopic [Fe/H] (as well as corresponding distance and V_ϕ) to about 20 $\mathrm{km\,s^{-1}\,dex^{-1}}$(from 40-50 $\mathrm{km\,s^{-1}\,dex^{-1}}$). This change in the V_ϕ vs. [Fe/H] slope indicates that it might be possible that the relation does have some slope which is masked by systematic errors in the photometric metallicity estimator; however, even if so, such a slope must be smaller than that implied by the spectroscopic subsample.

It is possible that the Spagna et al. (2010) results are caused by selection biases in the SDSS spectroscopic sample. Notably, when we fit two Gaussians (one for the disk and halo) to the V_ϕ and [Fe/H] distributions, about 45% of the spectroscopic sample are halo stars (consistent with Spagna et al. (2010) within $\sim 5\%$ errors), while halo stars make up only 8% of the complete sample. And when we compare the two panels in Figure 2.17 we are using exactly the same volume and exactly the same measurements: the only difference between the samples is that the spectroscopic sample includes only $\sim 2\%$ of all the stars, with the selection probability about 10 times higher for halo stars than for disk stars. On the other hand, ongoing work with SDSS G dwarf sample suggests that photometric metallicity errors may cause flattening of the V_ϕ vs. [Fe/H] (Y.S. Lee, private communication). Irrespective of the resolution of this puzzle, we note that even if the correlation is as strong as suggested by Spagna et al. (2010), the drop in rotational velocity is only $\sim$20 $\mathrm{km\,s^{-1}}$ between [Fe/H]$=-1$

and [Fe/H]=−0.5.

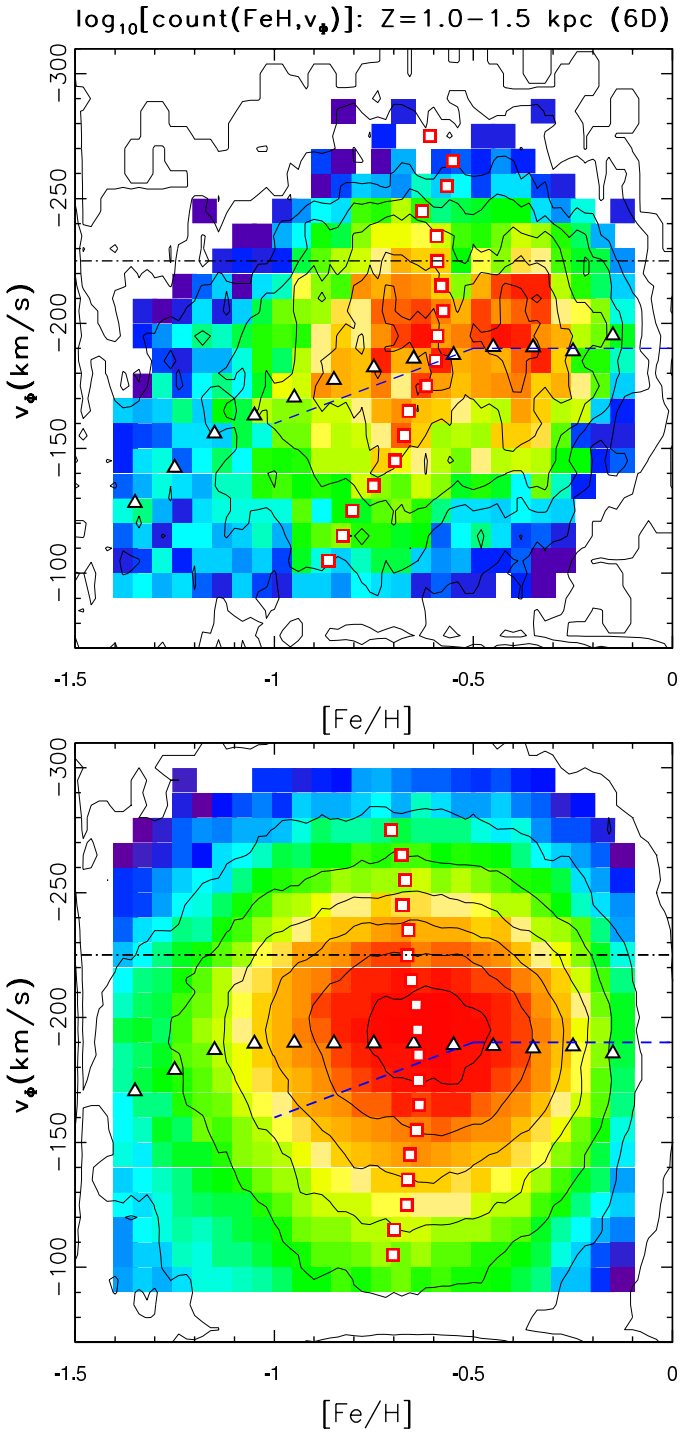

Figure 2.17 Top panel: $\sim 16,000$ stars selected from SDSS DR7 spectroscopic sample with $g-r=0.2-0.6$ from $z=1.0-1.5$ kpc. The stellar number density is shown as the color-coded map (low to high: blue to red) and by the contours. Triangles are the median V_ϕ for bins of [Fe/H], and squares are the median [Fe/H] for bins of V_ϕ. Spagna et al. (2010) results are overplotted with a dashed blue line for reference. Bottom panel: Analogous to plot in top panel but for full photometric sample: $\sim 124,000$ stars with $g-r=0.2-0.6$ and $z=1.0-1.5$ kpc, selected from the meridional plane defined by $l\sim 0^\circ$ or $l\sim 180^\circ$ (See Section 3.2 in Bond et al. 2010).

Chapter 3

MAPPING THE MILKY WAY DARK MATTER HALO WITH THE SLOAN DIGITAL SKY SURVEY

Portions of this chapter have been published as Loebman et al. 2012, ApJL, 758, L23, and are reproduced by permission of the AAS.

3.1 Chapter Summary

We present detailed evidence for a dark matter halo in the Milky Way (MW) that was derived using the number density distribution and kinematics of halo stars measured by the Sloan Digital Sky Survey (SDSS) to heliocentric distances exceeding ∼10 kpc and galactocentric distances of ∼20 kpc. Our analysis is based on Jeans equations and the morphology of implied two-dimensional acceleration maps, rather than the local solar neighborhood normalization of the total mass as done in previous studies. Conclusions about the existence of dark matter based on the classical Oort limit and rotation curves are based on similar assumptions about underlying physics, but here they are extended to a large two-dimensional volume of the Galaxy, instead of being limited to a solitary plane. Our Jeans equations approach is thoroughly tested using a mock catalog based on a cosmologically derived N–body+SPH simulation of a MW-like galaxy, and the known acceleration (gradient of gravitational potential) is successfully recovered. The same simulation is also used to quantify the relative contributions of visible and dark matter to the total acceleration. The stellar acceleration maps constructed using Jeans equations and SDSS-based observational constraints reveal that, in a Newtonian framework, the implied gravitational potential cannot be explained by visible matter alone: the gravitational force experienced by stars at galactocentric distances of ∼20 kpc is as much as three times larger than what can be attributed to purely visible matter. We utilize an analytic method for estimating the MW dark matter halo axis ratio and find that the SDSS data implies an oblate halo with an axis ratio $q_{DM} = 0.47 \pm 0.14$ (where the errors are statistical errors without systematic effects)

within the same distance range. These techniques can be used to map the MW dark matter halo with a much better fidelity with Gaia, and to much larger galactocentric distances with upcoming deep optical surveys, such as LSST.

3.2 Introduction

The nature of dark matter is one of the most fundamental questions in physical sciences today: determining the make-up of dark matter and its spatial distribution has important implications for fields ranging from theories of galaxy formation and evolution to particle physics and cosmology. While the gravitational arguments for the existence of dark matter are well established (Rubin et al., 1980; Spergel et al., 2003; Markevitch et al., 2004), its most basic properties are still disturbingly ambiguous. We can address fundamental questions about dark matter's properties by examining the shape of dark matter structure within and around our Galaxy. For example, the axial ratios of dark matter distribution can place strong constraints on the proposed type of dark matter particle (Tremaine & Gunn, 1979).

A myriad of techniques (Bahcall, 1984; Banerjee & Jog, 2011; Lux et al., 2012) – from tidal streams (Johnston et al., 1999) to Jeans equations (Loebman et al., 2012) – have been used to explore the Milky Way's (MW) dark matter distribution. In particular, applying Jeans equations to MW stars to infer the underlying mass distribution has a long and solid theoretical foundation (Jeans, 1915; Oort, 1932).

3.2.1 Jeans Equations as a Tool for Estimating Stellar Acceleration

While it is hard to measure stellar acceleration for individual stars (the black hole region in the Galactic center being an exception), which would directly constrain the gravitational potential, it is possible to estimate it statistically from stellar kinematics using Jeans equations. Jeans equations follow from the collisionless Boltzmann equation; for detailed derivation see Binney & Tremaine (1987). Using cylindrical coordinates and assuming an axisymmetric and steady-state system, the gradient of the potential in the radial (R) and vertical (Z) directions can be expressed in terms of observable quantities: the stellar number density distribution, ν, the mean azimuthal (rotational) velocity $\overline{v_\phi}$, and four velocity dispersions, $\sigma_{\phi\phi}$, σ_{RR}, σ_{ZZ}, and σ_{RZ} (all six quantities as functions of R and Z), as

$$-\frac{\partial\Phi}{\partial R} = a_R = \sigma_{RR}^2 \times \frac{1}{\nu} \times \frac{\partial\nu}{\partial R} + \frac{\partial\sigma_{RR}^2}{\partial R} + \sigma_{RZ}^2 \times \frac{1}{\nu} \times \frac{\partial\nu}{\partial Z} + \frac{\partial\sigma_{RZ}^2}{\partial Z} + \frac{\sigma_{RR}^2}{R} - \frac{\sigma_{\phi\phi}^2}{R} - \frac{\overline{v_\phi}^2}{R}, \quad (3.1)$$

and

$$-\frac{\partial\Phi}{\partial Z} = a_Z = \sigma_{RZ}^2 \times \frac{1}{\nu} \times \frac{\partial\nu}{\partial R} + \frac{\partial\sigma_{RZ}^2}{\partial R} + \sigma_{ZZ}^2 \times \frac{1}{\nu} \times \frac{\partial\nu}{\partial Z} + \frac{\partial\sigma_{ZZ}^2}{\partial Z} + \frac{\sigma_{RZ}^2}{R}. \quad (3.2)$$

Given accelerations $a_R(R,Z)$ and $a_Z(R,Z)$, *i.e.* the gradient of the gravitational potential, dark matter contributions to the potential can be estimated after accounting for contributions from visible matter. We note that although we call the term $-\partial\Phi/\partial R$ "acceleration" a_R for notational simplicity, it is only one component of the true R acceleration (that is, the time derivative of the velocity component in the R direction): $dv_R/dt = -\partial\Phi/\partial R + \overline{v_\phi}^2/R$. As we demonstrate later (see Figure 3.11), the second term is negligible for halo stars because the halo rotation is not significant (but we never make this assumption explicitly and carry all the terms throughout our analysis). Of course, in case of Z component, $dv_Z/dt = -\partial\Phi/\partial Z$.

Traditionally, Galactic studies utilizing Jeans equations were limited by data to the solar neighborhood (within ∼150 pc, *e.g.* Kapteyn, 1922; Oort, 1960; Bahcall, 1984). The main conclusion drawn from local studies is that dark matter contributes a small (of the order 10%) but significantly detected fraction of gravitational mass in the solar neighborhood (corresponding to about 0.01 $M_\odot$ pc^{-3}, or 0.38 GeV cm^{-3}, Kuijken & Gilmore, 1989; Creze et al., 1998; Holmberg & Flynn, 2000).

Several groups have extended these studies to a few kpc from the plane of the disk (Kuijken & Gilmore, 1991; Siebert et al., 2003; Holmberg & Flynn, 2004; Smith et al., 2012; Bovy et al., 2012). Recently, Garbari et al. (2012) used a sample of 2000 K dwarf stars that extend to 1 kpc above the plane of the disk and estimated the local dark matter density distribution $\rho_{DM} = (0.022 \pm 0.015)\,M_\odot$ pc^{-3}. Using kinematic data for ∼400 thick disk stars at distances of a few kpc from the Galactic plane from Moni Bidin et al. (2012), Bovy & Tremaine (2012) estimated $\rho_{DM} = (0.008 \pm 0.002)\,M_\odot$ pc^{-3}. Note that this remarkably small quoted error implies a statistically significant dynamical detection of dark matter in the solar neighborhood.

It has been difficult to extend these measurements to distances beyond a few kpc from the solar neighborhood (van der Marel, 1991). In a study of radial velocities of ∼2,500 blue horizontal branch stars at distances from ∼5 to 85 kpc from the Galactic center, Samurović & Lalović (2011) concluded that the Newtonian model without dark matter cannot fit the observed velocity dispersion profile. They also tested various MOND models and concluded that these fit the data as well.

Loebman et al. (2012) presented a brief research note which applied the Jeans equation technique to SDSS observations of Galactic halo stars; here we present a more detailed analysis and discussion of this technique and motivate its future application in the era of Gaia and LSST. In §3.3, we describe the simulation employed in this work to test the Jeans equations approach, as well as a code for generating mock samples of Galactic populations trained on SDSS data. The simulation-based tests, as well as application of the Jeans method to SDSS data are presented in §3.4. An analytic method for estimating the shape of the MW dark matter halo is tested using the adopted N–body simulation and applied to SDSS data in §3.5. We summarize and discuss our results in §3.6.

3.3 Background

Here we utilize a novel application of Jeans equations made possible by the Sloan Digital Sky Survey[1] data (York et al., 2000, hereafter SDSS). Due to substantial sky coverage and accurate multi-color photometry to faint limits, the stellar number density distribution and stellar kinematics in the Galactic SDSS data set were mapped out using numerous main sequence stars detected to galactocentric distances of ∼20 kpc (Jurić et al., 2008; Ivezić et al., 2008a; Bond et al., 2010). The extent of these maps is sufficiently large that it is possible to investigate stellar acceleration via Jeans equations. The key issue in applying this form of Jeans equations is determining the various spatial derivatives of the velocity dispersions (see Equations 3.1 and 3.2); they are hard, if not impossible, to reliably constrain using only the local solar neighborhood data. However, these spatial derivatives can be directly measured using SDSS data.

[1] www.sdss.org

We address here the following main questions:

- Given that both observations of the MW and modern N–body simulations do not support a simple steady-state picture (e.g. due to mergers), nor a perfect cylindrical symmetry, is it indeed possible to recover the known gravitational potential in a N–body simulation by simply applying Jeans equations to simulated stellar number density distribution and kinematic data?

- If so, are the stellar acceleration maps derived from SDSS data consistent with expectations based only on visible matter?

- If not, what are the differences in the morphology of stellar acceleration maps due to the inclusion of a dark matter component and what can be inferred about its distribution?

In this section we describe the background information and tools needed to investigate these questions, and we then provide answers in the following section.

3.3.1 N–body+SPH Simulation

To test the Jeans equation approach, we apply our analysis tools to a simulation with *known* stellar accelerations, velocities and stellar spatial (number density) distribution. We use a cosmologically derived (WMAP3, Spergel et al., 2003) Milky Way–mass galaxy evolved for 13.7 Gyr using the parallel N–body+SPH code GASOLINE (Wadsley et al., 2004), which contains realistic gas, cooling and stellar feedback (Stinson et al., 2006; Shen et al., 2009; Christensen et al., 2012). We track the galaxy's formation and evolution using the zoomed-in volume renormalization technique (Katz & White, 1993; Brooks et al., 2011; Pontzen et al., 2008; Governato et al., 2012). Our simulated galaxy includes a stellar halo, which is built up primarily during the merging process in a ΛCDM cosmology (*e.g.* Bullock & Johnston, 2005; Zolotov et al., 2009).

GASOLINE simultaneously calculates the potential and the acceleration that particles feel; force calculations are consistent with other state-of-the-art cosmological gas-dynamical

codes (Power et al., 2003; Scannapieco et al., 2012). The typical RMS acceleration error is $\sim$ 0.2% (Wadsley et al., 2004). Full 6D phase space (x, y, z, v_x, v_y, v_z) and mass information is also tracked.

At the end of the simulation, the average star particle mass is ~ 5800 $M_\odot$ and the dark matter particle mass is 1.3×10^5 $M_\odot$, with the minimum gas smoothing and dark matter softening length of 173 pc. At redshift of zero, the simulated galaxy has a virial radius of 227 kpc and a virial mass of 6.8×10^{11} $M_\odot$, of this, 7% is in gas, 6% is in stars, and 87% is in dark matter. The dark matter to baryon mass ratio in a region corresponding to solar neighborhood is 36%. A total of 4.6×10^6 dark matter, 2.1×10^6 gas and 7.4×10^6 star particles are within the virial radius at redshift of zero. The simulated galaxy is *approximately* rotationally symmetric (a total enclosed matter axis ratio $b : a > 0.9$ within 100 kpc, and a stellar matter axis ratio $b : a > 0.95$ at R=10 kpc), has a R-band disk scale length of $\sim$3.1 kpc and corresponding bulge to disk ratio of 0.33 (Jonsson, 2006), and maximum circular velocity of $\sim$235 km/s. These structural parameters are within 10% of those measured for the Milky Way (for example, Xue et al., 2008, find that the virial mass of the Milky Way's dark matter halo is in the range 8–13 $\times$ 10^{11} $M_\odot$, see Table 3.1 for details).

For reference, Figure 3.1 gives a visual perspective of N-body simulation used throughout this chapter. Figure 3.1 shows a top-down and edge-on view of the stellar particle distribution at $Z = 0$ when visualized on a logarithmic scale. The edge-on view has yellow lines overplotted to indicate the region selected in our analysis to mimic the SDSS volume. Also plotted is the number of stellar particles within the selected SDSS volume when binned in 1.0 kpc x 1.0 kpc R-Z bins. This panel illustrates that *our high resolution simulation has enough stellar particles (at least 100 per bin) to conduct a statistical analysis in a synthetic SDSS volume.*

3.3.1.1 The Spatial Distribution of Mass in the Simulated Galaxy

Many of the plots throughout this paper show a total or mean quantity mapped into rectilinear bins in R-Z space within $0 \leq$ R/kpc ≤ 20 and $0 \leq$ Z/kpc ≤ 10. This perspective

	Milky Way	N–body Simulation
Virial Radius (kpc)	200[a]	227
Virial Mass ($M_\odot$)	1.0×10^{12}[b,c]	6.8×10^{11}
R-band Disk Scale Length (kpc)	3.6[d]	3.1
Maximum Circular Velocity (km/s)	220[e]	235

Table 3.1 A comparison of various structural parameters between the Milky Way and the adopted N–body Simulation

References. —

a Boylan-Kolchin et al. (2011)

b Xue et al. (2008)

c Klypin et al. (2002)

d Jurić et al. (2008)

e Xue et al. (2008)

gives a sense of two dimensional distribution of a quantity throughout the SDSS volume. Figure 3.2 provides an example of this for four relevant quantities within the N–body simulation: total, dark matter, visible, and stellar halo mass density. The SDSS footprint within the simulation (shown here in red) is always overplotted for reference. The top left panel of Figure 3.2 shows the total mass density, including gas, dark matter and stars. To the right of this panel is the dark matter density distribution. The significance of dark matter relative to the gas and stars is not constant, yet the majority of the total mass density within the SDSS footprint is clearly from dark matter. The bottom two panels illustrate the distribution of visible matter. The bottom panel on the left of Figure 3.2 shows the mass density of all gas and stars within the N–body simulation. Two striking structural features stand out within this total visible matter density map: the bulge (R $\leq$ 5 kpc, Z $\leq$ 4 kpc) and disk (5 kpc $\leq$ R $\leq$ 20 kpc, Z $\leq$ 2 kpc). These structures are not significantly sampled by the SDSS volume within the simulation. The bottom right-hand panel of Figure 3.2 shows the stellar halo mass density within the simulation. Note that the majority of the

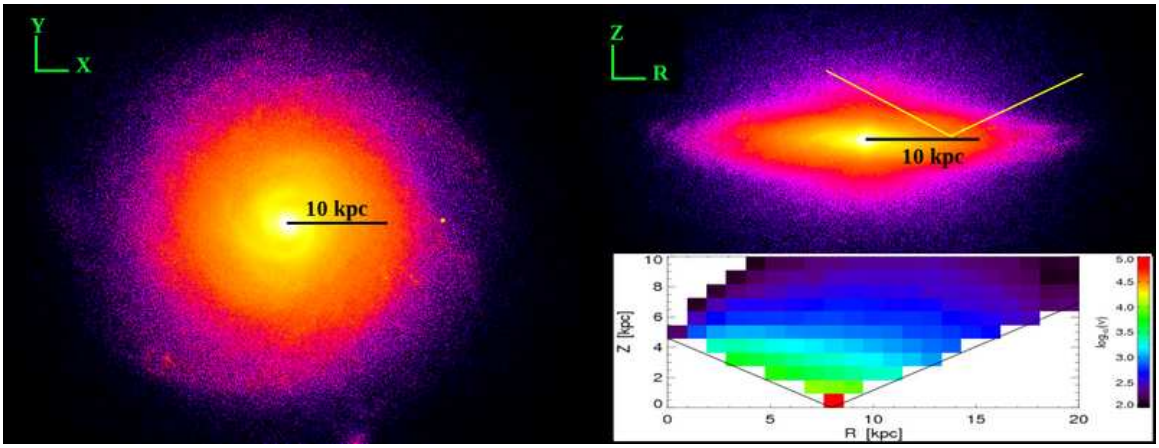

Figure 3.1 (Left) top down view of the stellar particle distribution (shown on a logarithmic scale) at $Z = 0$ of the adopted simulated MW–like galaxy. (Top right) edge-on view of the same stellar particle distribution. The yellow lines indicate the region selected in our analysis to mimic the SDSS volume. (Bottom right) the number of stellar particles within the selected SDSS volume when binned in 1.0 kpc x 1.0 kpc R-Z bins; this high resolution simulation has enough stellar particles (at least 100 per bin) to conduct a statistical analysis in the volume probed by SDSS.

visible mass within the SDSS footprint is from the stellar halo.

3.3.1.2 Tests of Axial Symmetry

Before we project mean quantities in the R-Z spatial grid or use the axisymmetric form of Jeans equation, we motivate the application of these techniques by illustrating the simulation's ϕ symmetry. The top panel of Figure 3.3 shows the major to semi-major axis ratio (b/a) of dark matter and halo star particles across the SDSS footprint within the simulation. Axis ratios of the particle distribution are determined following the iterative technique outline in §4.2 of Roškar et al. (2010) which identifies isodensity contours. This procedure is analogous to that used in Katz (1991), though it uses differential shells (in increments of 0.5 kpc) instead of cumulative shells following Debattista et al. (2008). For both dark matter particles and stellar halo particles, the b/a axis ratio is always greater than or equal to 0.8 and less than 1.0, indicating the distributions are nearly but not completely axisymmetric in the ϕ direction. At the virial radius, the b/a axis ratio for all particles is 0.91. The bottom panel of Figure 3.3 is analogous to the top panel but for the major to minor axis (c/a).

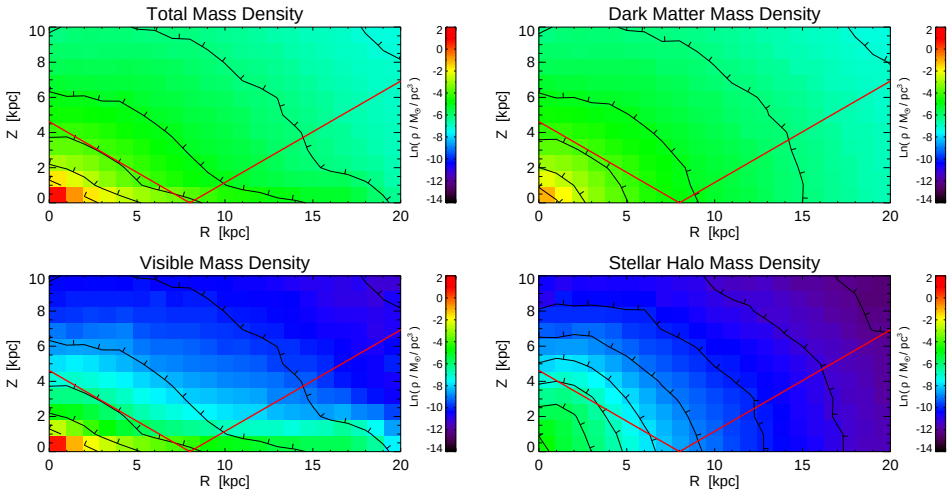

Figure 3.2 The azimuthally averaged mass density maps of four relevant quantities within the N–body simulation: total, dark matter, visible, and stellar halo mass. The displayed dynamic range is the same in all panels for easy comparison. Overplotted are logarithmically spaced isodensity contours; contour tick marks correspond to the direction of decreasing density. Also overplotted in red is the SDSS footprint within the simulation. (Top left) The total mass density (gas, dark matter and stars) within R $\leq$ 20 kpc and Z $\leq$ 10 kpc of the center of the N–body simulated galaxy. (Top right) The dark matter density within the simulation. The majority of the total mass density within the SDSS footprint is from the dark matter. (Bottom left) The mass density of all visible matter (gas and stars) within the N–body simulation. The bulge (R $\leq$ 5 kpc, Z $\leq$ 4 kpc) and disk (5 kpc $\leq$ R $\leq$ 20 kpc, Z $\leq$ 2 kpc) structure are evident within this distribution. (Bottom right) The stellar halo mass density within the simulation. The majority of the visible mass within the SDSS footprint is from the stellar halo.

The c/a axis ratio is a measure of the departure from spherical symmetry for axisymmetric shells. A c/a axis ratio of 1 is a perfectly spherical mass distribution; $c/a < 1$ indicates that the distribution is flattened (oblate) in the same sense as the stellar disk. At the virial radius, the c/a axis ratio for all particles is 0.74. As the bottom panel of Figure 3.3 shows, in this N–body simulation, both the dark matter and stellar distributions are oblate, and the dark matter c/a axis ratio does not vary significantly over the entire SDSS volume.

3.3.1.3 The Acceleration Maps for a Simulated Galaxy

One final thing to consider before applying Jeans equation to the simulation: what do the true accelerations look like for the simulation? The top panel of Figure 3.4 shows the mean

component of the acceleration in the Z direction projected into the R-Z grid; here, the acceleration of each particle was calculated using the force from all the particles in the entire simulation. For comparison, the middle panel shows an analogous map, but here, the acceleration of each star and gas particle was calculated using only the contributions from other star and gas particles (that is, the contribution from the dark matter was not included). As evident, there are substantial differences in the morphology of the two maps; the bottom panel shows the ratio of the top and middle panel. This panel demonstrates that *the effect of dark matter on the acceleration in the Z direction increases quickly away from the plane of the disk and towards the outer parts of the galaxy*; for example, the ratio of accelerations is doubled by R=8 kpc and Z=6 kpc. These distances are probed by SDSS – hence these results suggest that the effect of dark matter on stellar acceleration may be uncovered in SDSS data, and that stellar populations in the halo are more sensitive to the existence of dark matter than disk stars.

Along the same lines, the top panel of Figure 3.5 illustrates the mean component of the acceleration in the R direction when the force of all the particles (gas, dark matter and stars) in the simulation is considered, while the middle panel shows the mean component when the force of just gas and star particles are considered. The bottom panel shows a ratio of the top panel to the middle panel; the effects of dark matter are easily discernible; for example, the ratio of accelerations is doubled by R=8 kpc and Z=4 kpc.

3.3.2 SDSS-based Mock Catalogs: galfast

When constraining the Galactic potential via Jeans equations with SDSS (or any other survey) data, several preliminary analysis steps are required:

1. In order to quantify the stellar number density distribution as a function of coordinates R and Z (ν in Equations 3.1 and 3.2), appropriate stellar population needs to be selected (e.g. halo stars), distances to stars estimated, and observational selection function accounted for. In addition, the assumption of cylindrical symmetry must be tested, and the impact of local substructure (e.g. stellar streams) quantified.

2. In order to quantify the four velocity dispersions and the mean azimuthal velocity

as functions of coordinates R and Z, complex kinematics (proper motion and radial velocity measurements) are needed and require substantial analysis. For example, the error dependence for the radial velocity components and the error dependence for the tangential velocity components are fundamentally different as a function of distance. Notably, the tangential velocity components are computed as the product of distance and proper motion measurements, and these errors carry their own hidden dependence on distance. Proper motion errors increase for faint stars, and more distant stars are generally fainter than closer one.

These tasks are far from trivial, but fortunately they have already been undertaken and published.

3.3.2.1 The Stellar Number Density Distribution for Halo Stars

Jurić et al. (2008, henceforth J08) have accomplished the first task of quantifying the stellar number density distribution for both disk and halo components. They showed that the stellar number density distribution, $\nu(R, Z, \phi)$, can be well described (apart from local overdensities) as a sum of two cylindrically symmetric components

$$\nu(R, Z, \phi) = \nu_D(R, Z) + \nu_H(R, Z). \tag{3.3}$$

The disk component can be modeled as a sum of two exponential disks (see their Equations 22 and 23), while the halo component requires an oblate bi-axial (cylindrically symmetric) power-law model

$$\nu_H(R, Z) = \nu_D(R_\odot, 0)\, \epsilon_H \left(\frac{R_\odot^2}{R^2 + (Z/q_H)^2} \right)^{n_H/2}, \tag{3.4}$$

Here $\nu_D(R_\odot, 0)$ is the local solar neighborhood density of tracer stars, and ϵ_H measures the local fractional contribution of halo stars. The number count normalization, $\nu_D(R_\odot, 0)$, reflects how tracer stars are selected, and is related to the local luminosity function. Since the overall normalization of $\nu(R, Z)$ in Equations 3.1 and 3.2 cancels out, $\nu_D(R_\odot, 0)$ is not of further interest in this context.

J08 obtained best-fit MW parameters using SDSS data, after accounting for selection effects and masking regions with prominent substructure; their results are listed for both disk and halo components in their Table 10 (second column). For completeness, they obtained $\epsilon_H = 0.0051$, $q_H = 0.64$, and $n_H = 2.77$, with estimated uncertainties of 25%, $\lesssim$0.1, and $\lesssim$0.2, respectively. We note that the best-fit values for q_H and n_H are covariant – the more symmetric halos correspond to larger n_H, see their Figure 22. They also tested for cylindrical symmetry (see their Figure 11) and could not reject their best-fit axisymmetric number counts model.

Ivezić et al. (2008a, henceforth I08) studied the metallicity distribution of disk and halo stars and, of direct relevance to this work, demonstrated that the multi-component (i.e. disk and halo) decomposition of $\nu(R, Z)$ from Equation 3.3 is not a case of over-fitting; instead, a fairly simple selection, $[Fe/H] = -1$, clearly separates disk and halo components (see their Figures 5 and 9) and justifies the decomposition model from Equation 3.3.

3.3.2.2 The Kinematic Behavior of Halo Stars

Bond et al. (2010, henceforth B10) performed a detailed analysis of available kinematic data for SDSS stellar sample: radial velocities from SDSS spectroscopic survey and proper motions obtained by comparing SDSS astrometry and Palomar Observatory Sky Survey astrometry (Munn et al., 2004) from ∼50 years earlier. Their main result of interest to this work is clear demonstration (see their Figures 12 and 13) that the velocity ellipsoid for halo stars is invariant in spherical coordinates within the volume probed by SDSS data (galactocentric distances of $\lesssim$20 kpc). The very complex behavior of measured proper motions (see their Figure 14) and radial velocities (see their Figure 15) on the sky can be explained with a simple triaxial velocity ellipsoid that is invariant in spherical coordinates, σ_{rr}=141 km s^{-1}, $\sigma_{\phi\phi}$=85 km s^{-1}, and $\sigma_{\theta\theta}$=75 km s^{-1}, with uncertainties of about 5 km s^{-1}. Note, their leading sources of uncertainty are distance scale errors, uncertain correction to the local standard of rest, and systematic errors in radial-velocity and proper-motion measurements; see their section 5.3 for details.

3.3.3 The galfast Code

The best-fit $\nu_H(R, Z)$ from J08, and the best-fit velocity ellipsoid for halo stars from B10, could be inserted analytically into Equations 3.1 and 3.2 to compute a_R and a_Z. These analytic results would include proper accounting for SDSS selection effects and for Galactic substructure. Nevertheless, this would not be an optimal analysis procedure for at least two reasons: i) the information about finite stellar counts, and resulting counting noise, and volume edge effects, would be lost; and ii) the analysis of N–body simulations would still have to be performed using numerical derivatives of the "observed" velocity ellipsoid, and thus the results would be based on two different computational methods.

Instead, we choose to use a mock catalog of SDSS stars generated by the code *galfast*. This Monte Carlo code is based on the best-fit parameterizations of the distributions of stellar number density, metallicity and kinematics constrained by the SDSS data mentioned above. It produces catalogs with the same behavior of observables (such as counts, magnitudes, colors, proper motions, radial velocity) as seen in SDSS data, *except that there are no effects of substructure*, and selection effects are easily accounted for (e.g., one can generate a mock catalog for the whole Galaxy, and then apply exactly the same selection criteria to this mock catalog and to N–body simulation). The code also generates appropriate error distributions of all measured quantities.

We note that there are no hidden inputs, such as star-formation history, age-metallicity relation, etc., included in *galfast* – it is simply a sophisticated Monte Carlo generator designed to produce a snapshot of the current sky with the stellar content consistent with SDSS observations.

Using *galfast*, we generate a flux-limited catalog with $14 < r < 21$ and mimic the SDSS sky footprint by only considering high Galactic latitudes ($|b| > 30°$). The catalog lists true positions, absolute magnitudes, velocities and metallicity, as well as corresponding simulated SDSS observations convolved with measurement errors.

We treat this mock catalog as we would treat any catalog downloaded from the SDSS Data Release site. We correct the magnitudes in each filter for interstellar dust extinction and select a halo-like sample using a color cut $0.25 < g - r < 0.35$. The only instance where

we use the "truth" provided in the mock catalog is when rejecting stars with $M_r < 4$ to minimize contamination by giants (in a real sample, one could envision obtaining a spectrum for each star to accomplish the same step). The resulting sample of 0.61 million stars is dominated by low-metallicity main sequence F stars, with kinematics commensurate with a halo-dominated sample.

3.3.4 Numerical Procedures

We process our mock catalog from *galfast* and our mock catalog from our adopted N–body simulation in *exactly the same way, using the same code*: for a set of stars with given three-dimensional positions and three-dimensional velocities, we first determine the density, $\nu(R, Z)$, and the five kinematic quantities utilized in Equations 3.1 and 3.2, and then compute a_R and a_Z.

The computation of the number density, mean azimuthal velocity and velocity dispersions is done for each bin in the R-Z plane. We set the bin width to be 1 kpc, and we require at least 100 stellar particles per bin to minimize the shot noise. All quantities are computed using weights proportional to the mass of each stellar particle (assumed constant in case of *galfast* catalogs).

To estimate the gradients required in Equations 3.1 and 3.2 (*i.e.* the spatial gradients of the moments and the stellar mass density) we use a parametric technique: we fit a second-order polynomial in R and Z to values from the bin being processed and its 8 adjacent neighbors (using IDL fitting routine MPFIT2DFUN), and determine R and Z gradients by taking analytic derivative of the best fit. This method filters numerical (counting) noise to some extent and produces smoother maps (with values closer to the truth in case of *galfast* catalogs, where we know that velocity dispersion gradients in spherical coordinates are vanishing by construction). We exclude edge pixels (bins) from further analysis because the parametric results are not as robust due to smaller number of adjacent pixels.

The *galfast* catalogs provide a strong test of our algorithms; we must recover the density and kinematics trends that *galfast* used to generate them. In case of N–body simulations, we have an additional test: if all algorithms are correctly implemented, *and* if all assumptions

that go into derivation of Jeans equations are not too incorrect, then we ought to be able to reproduce true a_R and a_Z, that are known from direct force calculations. These two analysis steps are described in the next section.

3.4 Results

In this section we first test the Jeans equations approach using a realistic MW-like simulated galaxy with known stellar accelerations from force computations. The simulated galaxy is not perfectly axisymmetric, nor is it in a steady-state, and the comparison of known accelerations and those computed by Jeans equations provides a quantitative assessment of both systematic and random errors inherent in this method. After quantifying these errors, we apply the same methodology to *galfast* catalogs and demonstrate the evidence for the existence of dark matter in the Milky Way halo.

3.4.1 Tests of the Jeans Equations Method Using Simulations

To quantify acceleration errors in the Jeans equations method, we use an N–body simulation, with positions, velocities, and accelerations for 7.3 million stellar particles within the virial radius. To maintain identical selection effects as with the SDSS data, we only use simulation data within SDSS footprint; this region contains 220,000 stellar particles; their distribution is shown in Figure 3.6. We include all the star particles from this region in our analysis (that is, there is no specific selection of "halo stars"); however, we exclude results within 1 kpc of the plane of the disk to minimize the influence of disk stars and their strong gradients in all relevant quantities.

Our data is binned in 1 kpc square R-Z pixels; we also investigated smaller bin sizes, down to twice the force softening length (346 parsec). Because the particle number density decreases fast with galactocentric radius, the adopted size of 1 kpc is a "sweet spot" that allowed us to spatially resolve gradients in the acceleration map, while simultaneously having enough stellar particles per bin for counting errors to remain small ($\sim$10%).

The top panel of Figure 3.7 shows the a_Z acceleration map generated by applying Jeans equations to particles from the N–body simulation in the region that mimics the SDSS volume. An overall gradient is easily discernible, with the magnitude of the acceleration

decreasing with increased radius (R). The true acceleration map (shown in the top panel of Figure 3.4) displays the same behavior; the bottom panel shows a ratio of the top panel and mean true acceleration. As evident, Jeans equations reproduce the true a_Z map quite well: for the entire SDSS volume, the mean value of a_Z^{Jeans}/a_Z^{True} is 1.05 with a dispersion[2] $\sigma_G = 0.18$. When we consider a column of data that is unaffected by the bulge in the simulation ($7 \leq$ R/kpc ≤ 9) we find that σ_G drops to 0.15, with a mean of 1.08.

Figure 3.8 shows an analogous set of maps for acceleration in R direction, a_R. The mean value of the ratio a_R^{Jeans}/a_R^{True} for the entire SDSS volume has a mean value of 1.02 with σ_G of 0.13. When the map is subselected to include data within $7 \leq$ R/kpc ≤ 9, the mean value drops to 0.99 with $\sigma_G = 0.12$. We note that we tested for the effects of non-axisymmetry on these results by making 8 slices in ϕ of 90 degrees offset by 45 degrees. We found that the mean acceleration within these slices varied by around 10%.

We conclude from this analysis of the N–body simulation that even in a non-steady state system with deviations from axial symmetry, *Jeans equations can still recover meaningful average accelerations; within a given bin, an individual acceleration value has expected random error below 20%, with a bias below 10%.* As we show next, this performance is sufficient to uncover strong evidence for the existence of dark matter in the MW halo.

3.4.2 Application of the Jeans Equations Method to SDSS Data

In this section we apply Jeans equations to a catalog of stars from SDSS volume generated using *galfast*. We first assess the relative significance of each term in Jeans equations as a function of R and Z to understand the global distribution of a_Z^{SDSS} and a_R^{SDSS}, the components of the acceleration in the Z and R directions implied by SDSS data. We compare the resulting a_Z^{SDSS} and a_R^{SDSS} maps to the maps generated using the N–body simulation; we inspect the morphology of the acceleration maps to draw conclusions about the presence of dark matter within the SDSS Galactic volume.

---

[2]Instead of using the classically defined standard deviation, which is sensitive to non-Gaussian outliers, we use the interquartile range of the distribution to estimate the dispersion. The interquartile range is normalized to obtain a standard deviation in case of Gaussian distribution, $\sigma_G = 0.7413\,(q_{75} - q_{25})$, where q_{25} and q_{75} are the 25% and 75% quartiles.

3.4.2.1 The Construction of the Acceleration Maps

We first examine the spatial distribution of stars with $M_r \geq 4$ and $0.25 < g - r < 0.35$ (top left panel in Figure 3.9). A selection function correction has been applied to compensate for the varying range of the axial (ϕ) angle sampled by SDSS Galactic data; the computed distribution is a good match to the analytic model used by *galfast* and verifies that the binning algorithm and the selection function correction are correctly implemented.

Figure 3.9 also shows velocity distribution moments σ^2_{RZ}, σ^2_{RR}, $<V_\phi>^2$, $\sigma^2_{\phi\phi}$, and σ^2_{ZZ}. The strong variation with R and Z seen for σ^2_{RZ}, σ^2_{RR}, and σ^2_{ZZ} is due to the use of cylindrical coordinate system. We have verified that analogous estimates performed in spherical coordinate system reproduce the spatially invariant velocity ellipsoid used by *galfast* to within numerical noise.

The spatial derivatives of these terms are used in Equations 3.1 and 3.2 to compute a_Z^{SDSS} and a_R^{SDSS}; they are illustrated in Figures 3.10 and Figures 3.11, together with the main result of our analysis, a_Z^{SDSS} and a_R^{SDSS} maps shown in the top left panel in each figure. In each figure, other panels show all the additive terms from Equations 3.1 and 3.2. Note that different terms have varying contributions towards the final acceleration maps. All terms contributing to acceleration maps show smooth global behavior, with only a small number of pixels deviating from the overall trends.

3.4.2.2 The Interpretation of the Acceleration Maps

Now that we have maps for a_Z^{SDSS} and a_R^{SDSS}, we consider what they tell us about the underlying distribution of matter within the SDSS volume. To assess this, we again draw upon our N–body simulation to predict what behavior we would expect when the dark matter contribution is and is not included.

Recall the top panels of Figures 3.4 and 3.5, which shows the map of a_Z^{Full} and a_R^{Full} from N–body simulation. In this case, the acceleration of each particle was calculated using the force from all the particles in the entire simulation. For comparison, the middle panels of these two figures show analogous maps, but there the acceleration was calculated without including dark matter contribution.

Similarly, the middle and bottom panels of Figures 3.12 and 3.13 show the ratio of the a_Z^{SDSS} and a_R^{SDSS} map to the simulation's a_Z^{Full} and a_Z^{Baryon} and a_R^{Full} and a_R^{Baryon} maps respectively. As easily discernible, the acceleration maps derived from SDSS data are much more similar to the model-based acceleration maps that *include* contributions from both baryons and dark matter. *At large galactocentric distances, the observed acceleration is as much as a factor of three to four stronger than what can be accounted for without dark matter contribution!*

A pixel-by-pixel comparison of the acceleration ratio maps from Figures 3.12 and 3.13 is shown in Figure 3.14: the top panel shows the results for a_Z, while the bottom panel shows the results for a_R. Here it is easy to see that the observed maps are much better matched by the model maps that include dark matter. The fact that the *shape* of the observed acceleration maps are better matched when dark matter is included is seen as a much narrower histogram in both panels.

Therefore, by generating acceleration maps using SDSS data and comparing these maps to expectations from an N–body simulation, we have demonstrated that a model containing dark matter is a much better fit to observations than the model that contains baryonic matter alone.

3.5 Analytic Estimate of the Axis Ratio for the Dark Matter Halo

As we have just shown in the preceding section, there is a strong indication of the presence of non-visible matter that contributes to the gravitational potential within the SDSS volume. We have reached this conclusion by comparing the morphology of acceleration maps produced using N–body simulation data to acceleration maps produced by applying Jeans equations to *galfast* catalog. Since the resulting acceleration maps are two–dimensional, we can also estimate the shape of the dark matter halo within the SDSS volume. To do this properly, including a quantitative understanding of uncertainties, we would ideally use a large suite of simulated cosmologically derived MW-like galaxies. Simulations that produce acceleration maps consistent with SDSS data would sample the allowed set of dark matter halo geometry. Such a suite of simulations should sample the full range of non-steady state and non-axisymmetric conditions and thus allow the systematic assessment of the signifi-

cance of these deviations on the error associated with the application of Jeans equations. Although computationally expensive, it is likely that in the not-to-distant future, such a suite of high resolution simulations will exist. In the meantime, we can still approximately estimate the axis ratio for the dark matter distribution within the SDSS volume by applying a simplified analytic approach that requires as input only the axis ratio for the stellar distribution and the information about stellar velocity ellipsoid.

The method we use was developed by van der Marel (1991, henceforth V91) and considers the global flattening and kinematics of the Galactic halo using Jeans equations. V91's analysis makes the assumption that both stellar and dark matter distributions (but not the potential!) can be described by power-law ellipsoids (such as given by Equation 3.4), and that stellar velocity ellipsoid is aligned with either cylindrical coordinates or spherical coordinates. In addition, the method assumes that the stellar system is in approximate hydrostatic equilibrium in order to apply Jeans equations. V91's method finds a potential that self-consistently solves the $\hat{Z}$ and $\hat{R}$ components of Jeans equations. Under these assumptions, V91 derives relationships between the axis ratio of the dark matter halo, q_{DM}, and the axis ratio of the stellar halo, q_H, the power-law index for the stellar halo, n_H, and stellar velocity dispersion. Assuming that velocity ellipsoid is invariant in spherical coordinates (see below for further discussion), V91 gives an implicit formula for q_{DM}

$$F(q_{DM}) = \frac{1 + (\sigma^2_{\phi\phi}/\sigma^2_{\theta\theta}) + (n_H - 2)\,(\sigma^2_{rr}/\sigma^2_{\theta\theta})}{(n_H/q^2_H) + (n_H - 2)\,\left(\sigma^2_{rr}/\sigma^2_{\theta\theta} - 1\right)} \tag{3.5}$$

where (σ_{rr}, $\sigma_{\phi\phi}$, $\sigma_{\theta\theta}$) describe the velocity ellipsoid in spherical coordinates, and

$$F(q_{DM}) = \frac{q_{DM}}{\sqrt{1 - q^2_{DM}}}\ \arctan\left[\sqrt{\frac{1 - q^2_{DM}}{q^2_{DM}}}\right], \tag{3.6}$$

is valid for $0 < q_{DM} < 1$ (for larger values of q_{DM} see Appendix in V91). Therefore, given n_H and q_H from J08 and (σ_{rr}, $\sigma_{\phi\phi}$, $\sigma_{\theta\theta}$) from B10, q_{DM} can be readily computed. However, it is not obvious what the uncertainty of this estimate would be given that the assumptions made when deriving these expressions are not entirely correct for the real MW.

To test how well this method works for a realistic system that deviates from the assumed behavior, we first apply it to our N–body simulation and estimate the uncertainty in the

derived q_{DM}. We expect the halo to be more oblate in the inner regions as it has been adiabatically deformed by the baryonic disk (Blumenthal et al., 1986; Gustafsson et al., 2006). Once we confirm the validity of this technique on the N–body simulation, we then apply the method to SDSS data and derive the implied axis ratio for the dark distribution in the MW halo.

3.5.1 Test of the Analytic Method Using the N–body Simulation

One of the assumptions built into the V91 method is that the stellar and dark matter distributions can be described by power-law ellipsoids. As we outlined in Section 3.3.1, the axis ratio c/a (equal to q_H or q_{DM}, depending on the type of particles considered) for N–body simulation varies for both stellar and dark matter particles within the probed volume (see Figure 3.3) and thus this assumption is not strictly obeyed. We first discuss in more detail how we estimated q_H and q_{DM} for the N–body simulation, then we discuss the behavior of the velocity ellipsoid for stellar particles, and we finally apply the V91 method.

3.5.1.1 The Global Ellipsoidal Power-law Fits to the Particle Distribution

For this exercise, we use only the stellar particles determined to be "halo stars" by a specific energy and angular momentum cut ($E_{tot} > -1.43e+05$ km^2 s^{-2}; $J_z/J_{circ} < 0.37$) (Governato et al., 2009; Scannapieco et al., 2012). By number, halo stars account for 8% of the overall stellar distribution; we used all the star particles (not just the halo stars) in our earlier Jeans equation analysis to avoid small number statistics when star particles are binned in both R and Z space. Here, we want to avoid the impact of disk stars when estimating q_H. In addition, we only use stars with galactocentric distances in the range 5.5 kpc $\leq r \leq$ 36.0 kpc (where here, r, is the radius in a spherical coordinate system) to avoid contamination by bulge stars. Within this volume, the stellar axis ratio (see Figure 3.3) determined in concentric shells using the technique outlined in §4.2 of Roškar et al. (2010) varies in the range 0.65–0.91. The variation of the dark matter axis ratio is smaller and in the range 0.67–0.75.

To apply the V91 method, we need to estimate the "global" values of q_H and q_{DM}, as well

as the best-fit power-law indices, n_H and n_{DM}. Of course, we also need to assess if a single global power-law fit is a *reasonable* approximation to the distributions of particles within the relevant volume. For each type of particle, we create a grid of (q,n) pairs. For a given (q,n) pair, we compute the normalization constant for the model given by Equation 3.4, and then evaluate how well it agrees with the "data" by computing the scatter (using σ_G) of residuals, $\delta = \log(\rho^{Simulation}) - \log(\rho^{Model})$. The step size for the (q,n) pairs is 0.01 for both q and n, and the best-fit pair is chosen as the one which minimizes σ_G. The results of this minimization for both stellar and dark matter particles are shown in Figure 3.15.

We obtained the best-fit values $n_H = 3.63$, $q_H = 0.79$ and $n_{DM} = 2.49$, $q_{DM} = 0.74$ for the stellar and dark matter halo, respectively. These q values are within the ranges shown in Figure 3.3 and are in some sense the average of the values presented there. The quality of fits can be gauged from the minimum values of σ_G, 0.08 and 0.02 for the stellar and dark matter halo, respectively. Therefore, the variation of the particle density is captured by the models given by Equation 3.4 with a fractional scatter of 20% and 5%. Given the large dynamic range of the overall density variation, which exceeds two orders of magnitude (see Figure 3.2), this small scatter implies that the ellipsoidal power-law model provides reasonable approximations for both the stellar and dark matter halo.

3.5.1.2 The Velocity Ellipsoid for the Stellar Particles

The relationship between q_H and q_{DM} can be estimated using the V91 method only in two limiting kinematic cases: when the stellar velocity ellipsoid is aligned with either a cylindrical coordinate system, or aligned with a spherical coordinate system. To determine which case, if any, describes the N–body simulation, we examine the variation of the angle α (determined using a robust estimator for bi-variate Gaussian distribution[3]) between the radial coordinate axis and the principal axis of the velocity ellipsoid. Figure 3.16 demonstrates that the velocity ellipsoid of the stellar particles from the N–body simulation is nearly invariant in spherical coordinates (it is encouraging that the same behavior is seen in the SDSS data).

---

[3]To compute angle α, we adapted to IDL the `astroML` python code publicly available at http://www.astroml.org/book_figures/chapter3/fig_robust_pca.html

The velocity dispersion in spherical coordinates for the stellar particles within SDSS volume is (σ_{rr}, $\sigma_{\phi\phi}$, $\sigma_{\theta\theta}$) = (129.5, 60.1, 70.2) km s^{-1}. When the entire simulation volume is considered (that is, all halo stars within the virial radius), we obtain (σ_{rr}, $\sigma_{\phi\phi}$, $\sigma_{\theta\theta}$) = (146.0, 65.2, 90.3) km s^{-1}.

3.5.1.3 Application of the V91 Method to the N–body Simulation

We consider both the velocity dispersion ellipsoids determined above, and together with $n_H = 3.63$ and $q_H = 0.79$, we estimate q_{DM}^{V91} using Equation 3.5. The true value, determined directly from the simulated dark matter particle distribution, is $q_{DM} = 0.74$. Our results are illustrated in Figure 3.17.

The position corresponding to ($q_H = 0.79$, $q_{DM} = 0.74$) is marked by the black star. In case of perfect agreement, the line computed with Equation 3.5 would pass through this point. Indeed, the predicted value, $q_{DM}^{V91} = 0.66$, is biased low by less than 0.1. This is satisfactory performance given the two main sources of uncertainty: the distributions of stellar and dark matter particles in N–body simulation are not perfectly fit by ellipsoidal power-law model (the red star in the figure shows the mean values of q_H and q_{DM} from Figure 3.3, and the blue ellipse illustrates their dispersion), and the stellar velocity ellipsoid varies with sampling volume (compare thin and thick lines).

We conclude that the V91 method can be used to estimate q_{DM} with a systematic uncertainty on the order 0.1.

3.5.2 Analytic Estimate of the Dark Matter Axis Ratio for the Halo Using SDSS Data

As we demonstrated in the previous section, V91's analytic formalism can recover q_{DM} for the N–body simulation with a systematic error on the order 0.1. Here we apply V91's technique to the stellar halo data from the SDSS volume. B10 finds the metal-poor stellar velocity ellipsoid is well aligned with spherical coordinates throughout the SDSS volume, and therefore we use again Equation 3.5. We adopt $n_H = 2.77 \pm 0.2$ and $q_H = 0.64 \pm 0.1$ from J08, and (σ_{rr}, $\sigma_{\phi\phi}$, $\sigma_{\theta\theta}$)=(141, 85, 75) km s^{-1}, with uncertainties of 5 km s^{-1}, from B10.

In Figure 3.18, we show the relationship between q_H and q_{DM} as V91 did in his Figure 1, but here we have plotted these lines with the updated kinematic values from SDSS. For a given value of q_H on the solid line, we illustrate the allowable q_{DM} values generated by the 1σ range of best-fit kinematics. We bracket the errors associated with the kinematic measurements by considering two bounding cases: the kinematic errors being completely uncorrelated and completely correlated. We find the completely uncorrelated errors produce the largest range in q_{DM}; we adopt these errors to conservatively consider the largest range of plausible q_{DM} values. This range of values is shaded between the bounding dashed lines, with the upper dashed line corresponding to the curve generated using $\sigma_r = 146\,\mathrm{km\,s^{-1}}$, $\sigma_\theta = 70\,\mathrm{km\,s^{-1}}$, and $\sigma_\phi = 90\,\mathrm{km\,s^{-1}}$, and the bottom dashed line corresponding to the curve generated using $\sigma_r = 136\,\mathrm{km\,s^{-1}}$, $\sigma_\theta = 80\,\mathrm{km\,s^{-1}}$, and $\sigma_\phi = 80\,\mathrm{km\,s^{-1}}$.

Applying the best-fit SDSS value of q_H to the line generated from the best fit kinematics yields $q_{DM} = 0.47$. Propagating in quadrature the error associated with both the uncorrelated kinematics and the fit for q_H yields a 1σ range for q_{DM} of 0.14. Thus, using V91's analytic relationship between q_{DM} and stellar halo properties, with current best stellar axis ratio and kinematic constraints drawn from SDSS MW data, produces $q_{DM} = 0.47 \pm 0.14$, with a systematic uncertainty of about 0.1.

3.6 Discussion and Conclusions

We demonstrated that the SDSS observations of the MW stellar halo, in particular stellar counts and stellar kinematics, imply the existence of an invisible component that contributes to the gravitational potential. In essence, our conclusions about the existence of dark matter is based on same assumptions and physics as studies of rotation curves and the classical Oort limit, but here our analysis extends the discussion to a large two-dimensional volume of the Galaxy, instead of collapsing the analysis to a single plane.

Our results are derived using Jeans equations, which estimate stellar acceleration statistically from the observed spatial variation of stellar counts and stellar kinematics (Equations 1 and 2). The application of this method to galactocentric distance of up 20 kpc, sampled with numerous main sequence stars, was made possible by substantial SDSS sky coverage and accurate multi-color photometry to faint limits.

Using a modern cosmologically derived N–body simulation, designed to mimic the formation and evolution of a MW–like galaxy, we showed that the Jeans Equations method can uncover true accelerations despite deviations from a steady-state system with cylindrical symmetry: this method recovered average per-bin accelerations with random errors below 20% and a bias below 10%.

When applied to SDSS data, via mock catalogs generated by *galfast*, this method produced two-dimensional acceleration maps that, when combined with simulations, exceed expected accelerations based on visible matter alone by as much as a factor of three. Compared to the expected bias in the method ($< 10\%$), this discrepancy represents strong evidence for another matter component that contributes to the gravitational potential. When the simulation-based acceleration maps include a dark matter component, they are capable of explaining the spatial variation of the observed acceleration maps. This strong evidence for a dark matter component is not sensitive to the overall dark matter to baryon *normalization*, which can be considered as a fine-tuning model parameter, but is robustly derived from the *shape* of the observed acceleration maps.

Due to the lack of a large suite of N–body simulations, the method presented here does not provide errors for the total estimate of dark matter in the Milky Way; however, it does provide an expanded view of the distribution of dark matter beyond the solar neighborhood. Significantly, it allows us to consider how the distribution of dark matter varies both radially and vertically in the context of a large, observationally motivated data set. Given a large number of simulations with different dark matter halo properties, it will be possible to estimate the allowed range of the dark matter to baryon normalization ratio, as well as the uniqueness of the shape of MW dark matter halo implied by SDSS observations.

In the absence of a suite of N–body simulations, we approximately estimated the shape of dark matter halo using the method proposed by van der Marel (1991, V91). V91 showed that for an oblate distribution of dark matter it is possible to derive the dark matter axis ratio from the measured values of the stellar halo axis ratio and the velocity ellipsoid (via an application of Jeans equations; see his Equations 1 and 21 and Figure 1). We tested the validity of V91's approach applied to a non-steady-state, non-axisymmetric system by utilizing the N–body simulation. We generated an analytic fit to the simulation's stellar

halo axis ratio and recovered the known dark matter axis ratio using V91's technique. We then applied the same technique to SDSS measurements of the stellar halo axis ratio and kinematics, and we estimated that the MW's dark matter halo axis ratio is $q_{DM} = 0.47 \pm 0.14$. Compared to the SDSS stellar halo axis ratio, $q_H = 0.64 \pm 0.1$, the dark matter halo appears slightly more oblate. However, the quoted errors are only statistical and we cannot exclude systematic errors as large as 0.1. For example, V91's technique does not account for the contribution of disk stars to the gravitational potential. Within the galactocentric distances analyzed here, this contribution is expected to be minor; however, it is plausible that it might bias q_{DM} to a somewhat smaller value.

We note that there is a considerable range of MW dark matter halo axis ratios presented in the literature. A number of techniques have been used and the uncertainties are rarely reported; the axis ratios within the literature ranges from >0.7 at the low end (Ibata et al., 2001) to 5/3 at the high end (Helmi, 2004). Sometimes, triaxial models are incorporated, such as by Law & Majewski (2010) who used observations of Sgr tidal stream and N–body modeling to conclude that the MW has a triaxial dark matter halo that is nearly an oblate ellipsoid whose minor axis is contained within the Galactic disk plane. However, the simulations of Debattista et al. (2013) find that the MW disk is very unlikely to be in an intermediate orientation. Intriguingly, they find that the disk could persist off one of the principal planes of the potential. Lux et al. (2012) used satellite galaxies to find the MW dark matter halo is oblate, while Banerjee & Jog (2011) used observations of HI and claimed variation of axis ratio, with the halo increasingly prolate at large distances. We note that there is no consistent distinction in the literature between the axis ratio for iso-potential surfaces and the axis ratio for density distribution, which are generally different. Our values, based on V91's method, correspond to the axis ratio for the *dark matter density distribution*. In papers cited above, the axis ratio corresponds to the *potential* and is expected to be somewhat larger than q_{DM} reported here.

3.6.1 The Range of Validity of Our Results

Both stellar count and kinematics data from SDSS, on which our analysis is based, extend to no more than about 20 kpc from the Galactic center. Therefore, our results are limited in validity to the same volume of Galaxy and should not be extrapolated beyond this limit.

There are already strong indications that the stellar halo model from J08, given by Equation 3.4, cannot be extrapolated beyond galactocentric distance of about 30 kpc. Sesar et al. (2011) found, using main sequence stars detected by the Canada-France-Hawaii Telescope Legacy Survey (CFHTLS) in about 170 deg^2 of sky, that the halo stellar number-density profile becomes steeper at Galactocentric distances greater than ∼28 kpc, with the power-law index changing from $n = 2.62 \pm 0.04$ to $n = 3.8 \pm 0.1$. They measured the oblateness of the stellar halo to be $q_H = 0.70 \pm 0.01$ (statistical error only), and they detected no evidence of the oblateness changing across the range of distances probed. Deason et al. (2011) explored similar issues, using a sample of ∼20,000 BHB and blue straggler stars detected by SDSS over 14,000 deg^2 of sky, and obtained almost identical results to those from Sesar et al. (2011). Their best fitting model has an inner power-law index of $n = 2.3$ and an outer index of $n = 4.6$, with the transition occurring at ∼27 kpc, and a constant stellar halo flattening of $q_H = 0.6$. In addition, the distributions of RR Lyrae stars from the SEKBO survey (Keller et al., 2008), and of RR Lyrae stars from SDSS Stripe 82 data (Watkins et al., 2009; Sesar et al., 2010), indicate a steeper density profile beyond 30 kpc.

Similarly, the finding by B10 that the velocity ellipsoid for halo stars is invariant in spherical coordinates cannot be valid beyond about 30 kpc from the Galactic center. Brown et al. (2010) used the Hypervelocity Star survey data to measure the halo radial-velocity dispersion out to 75 kpc. They obtained results in statistical agreement with similar studies by Battaglia et al. (2005) and Xue et al. (2008), which they summarized as: "the Milky Way radial-velocity dispersion drops from $\sigma = 110$ km s^{-1} at $R_{gc} = 15$ kpc to $\sigma = 85$ km s^{-1} at $R_{gc} = 80$ kpc." (here R_{gc} is the Galactocentric radius R in our work here). It is hard to quantitatively and robustly estimate what this gradient implies for the underlying potential because the velocity dispersion in two orthogonal directions at distances beyond 30 kpc has not been measured yet; these measurements will likely have to wait for Gaia and

LSST surveys (see below).

In addition to the data limitations, simulations have their own caveats. We have demonstrated using an N–body simulation that the Jeans Equations method can recover the true stellar acceleration with a bias below 10%. However, the validity of this conclusion is crucially dependent on the similarity between the simulated galaxy and the MW. We showed that the simulated galaxy is similar to the MW in many important ways, such as the overall distribution of halo stars and their kinematics. Nevertheless, there are other untested aspects that might be important and perhaps are biasing our measurements of the dark matter halo properties. For example, Schlaufman et al. (2009, 2011) have shown, using data from the SDSS SEGUE spectroscopic survey, that about 10% of the halo stars within ∼20 kpc from the Sun cluster kinematically on very small spatial scales (typical radial-velocity dispersion is ∼20 km s^{-1}). It remains to be seen whether simulated galaxies also include this effect, and how it affects the performance of the Jeans equations method. In a recent related work, Cooper et al. (2011) analyzed a large number of state-of-the-art models for the stellar halo and found that, for the inner halo, the models predict stronger clustering than observed, suggesting the existence of a smooth component not currently included in simulations.

3.6.2 Future Work

It is possible to go beyond Jeans equations to use stellar kinematics to probe the full phase space distribution of stars. And, as Valluri et al. (2012) recently demonstrated, stellar orbits can be used to determine not only the shape of the inner halo, but the global shape of the Galactic halo. The Valluri et al. (2012) orbital spectral analysis method provides a strong complementary tool to the technique presented here for constraining the potential of the Milky Way halo and its stellar distribution function.

The full potential of this method will be reached by upcoming next-generation surveys, such as Gaia (Perryman, 2002) and LSST (Ivezić et al., 2008b). Gaia will provide measurements of distances and kinematics with a similar faint flux limit as SDSS, but with much smaller errors. LSST will obtain photometric and kinematic measurements of comparable

accuracy to those of Gaia at Gaia's faint limit, and extend them deeper by about 5 mag. With LSST, it will be possible to extend this study to about 10 times larger distance limit than possible today with SDSS data (Ivezić et al., 2012).

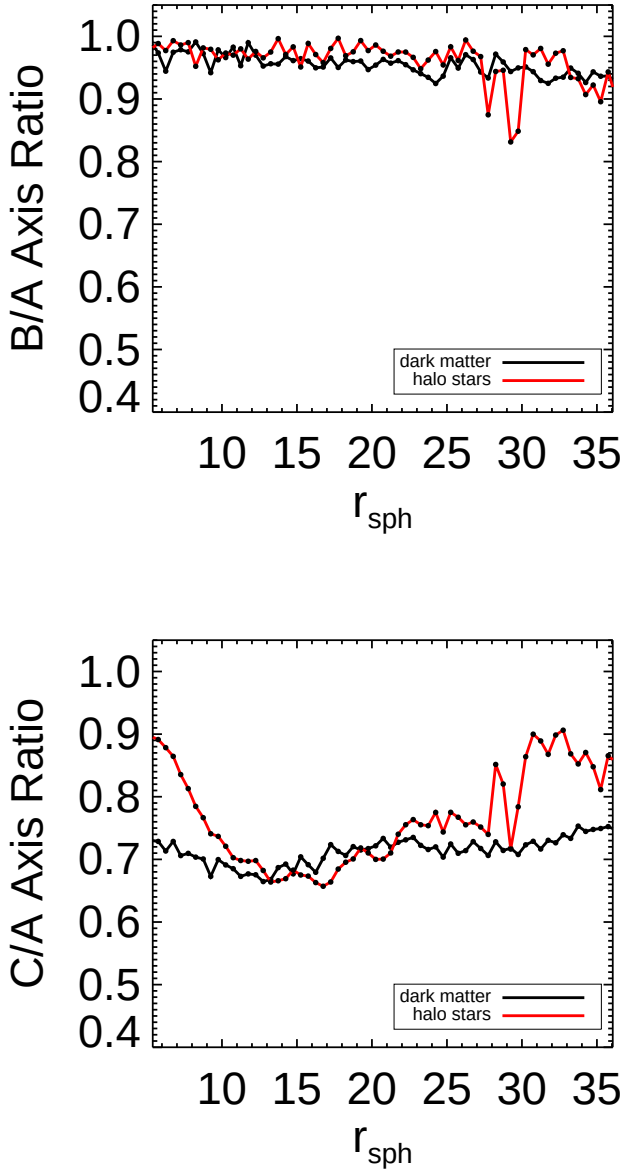

Figure 3.3 (Top) The semi-minor to semi-major axis ratio in the equatorial plane (b/a) of dark matter and halo star particles across the SDSS volume within the simulation. In both cases, the b/a axis ratio is always greater than or equal to 0.8 and less than 1.0, indicating the distributions are nearly but not completely axisymmetric in the ϕ direction. (Bottom) An analogous figure to the top panel but for the ratio of the semi-minor axis perpendicular to the equatorial plane and the semi-major axis (c/a). Both the dark matter and stellar distributions are oblate, and the dark matter c/a axis ratio does not vary significantly within the SDSS volume.

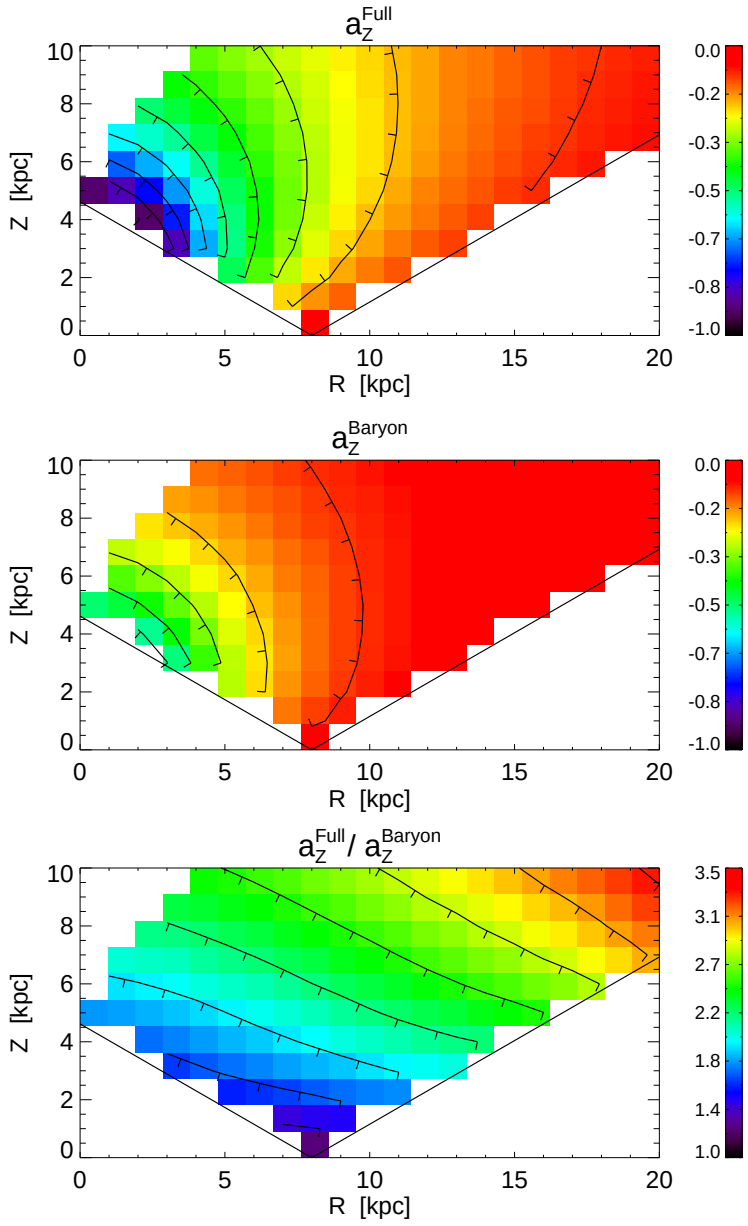

Figure 3.4 A comparison of the acceleration in the Z direction from the N–body simulation when all contributions are included (star, gas, and dark matter particles; top panel) to the result without dark matter (middle panel). The maps are limited to the volume explored by SDSS data, and the acceleration is expressed in units of 2.9×10^{-13} km s^{-2}. The ratio of the two maps is shown in the bottom panel. The importance of the dark matter increases with the distance from the origin; at the edge of the volume probed by SDSS ($R \sim 20$ kpc, $Z \sim 10$ kpc), the total acceleration in the analyzed simulation is about 3 times larger than contribution from the visible matter.

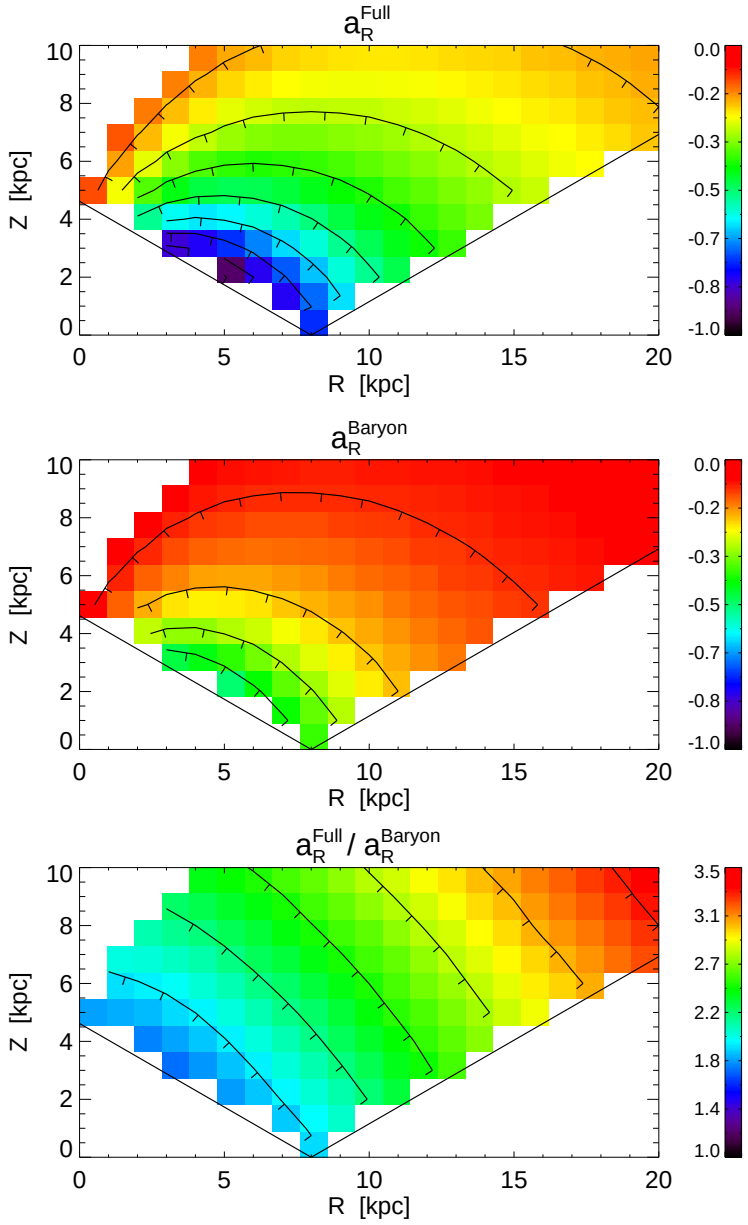

Figure 3.5 An analogous figure to Figure 3.4, except that the component of the acceleration in the R direction is shown. The acceleration is expressed in units of 2.3×10^{-13} km s^{-2}. Similar, to the acceleration map in the Z direction shown in Figure 3.4, the importance of the dark matter increases with the galactocentric distance.

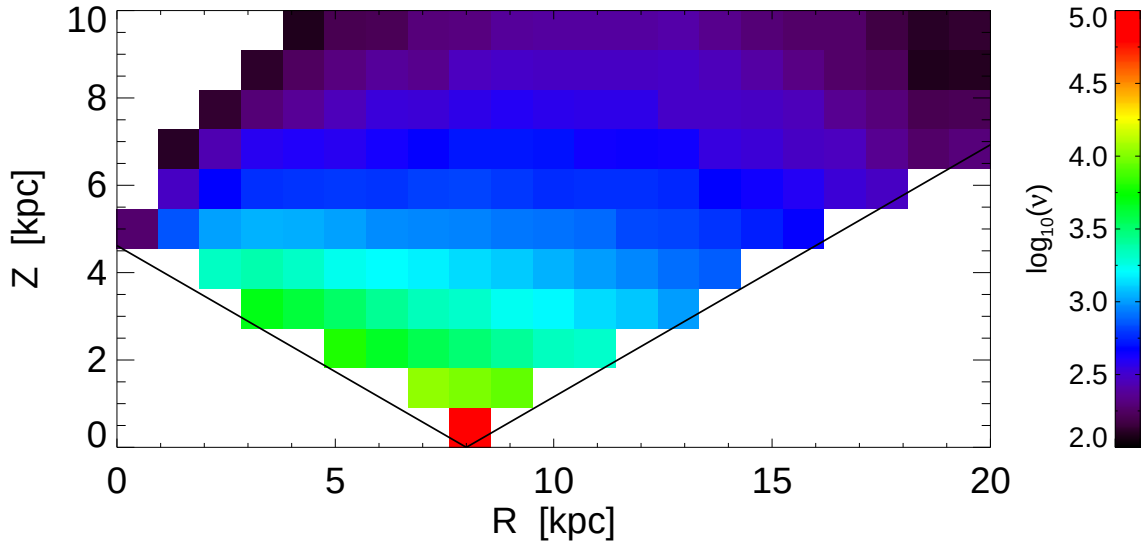

Figure 3.6 The number counts of stellar particles from the N–body simulation restricted to the volume probed by SDSS. Stellar particles have been binned in 1 kpc x 1 kpc R-Z bins and only bins with at least 100 particles are shown and used in our analysis. In addition, edge pixels are subsequently excluded from the Jeans equation analysis due to less reliable count gradient estimation.

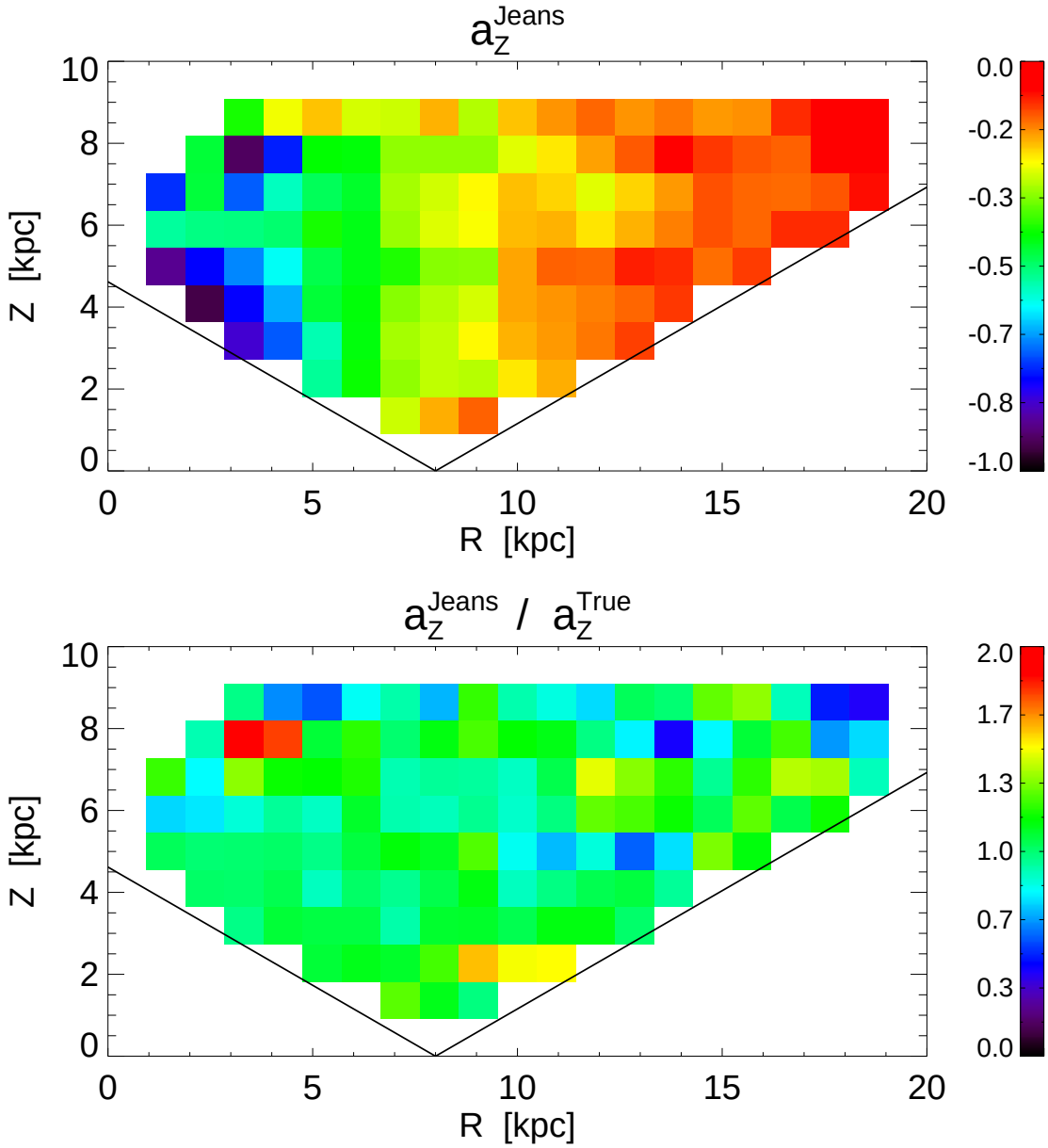

Figure 3.7 (Top) The acceleration in the Z direction for stellar particles from N–body simulation, derived using Equation 3.2 and expressed in units of 2.9×10^{-13} km s^{-2}. (Bottom) The ratio of the top panel and the true acceleration map known from force computations (top panel of Figure 3.4). The Jeans equations approach successfully reproduces the true acceleration map with a bias below ∼10%. The maps are spatially limited to the volume explored by SDSS data.

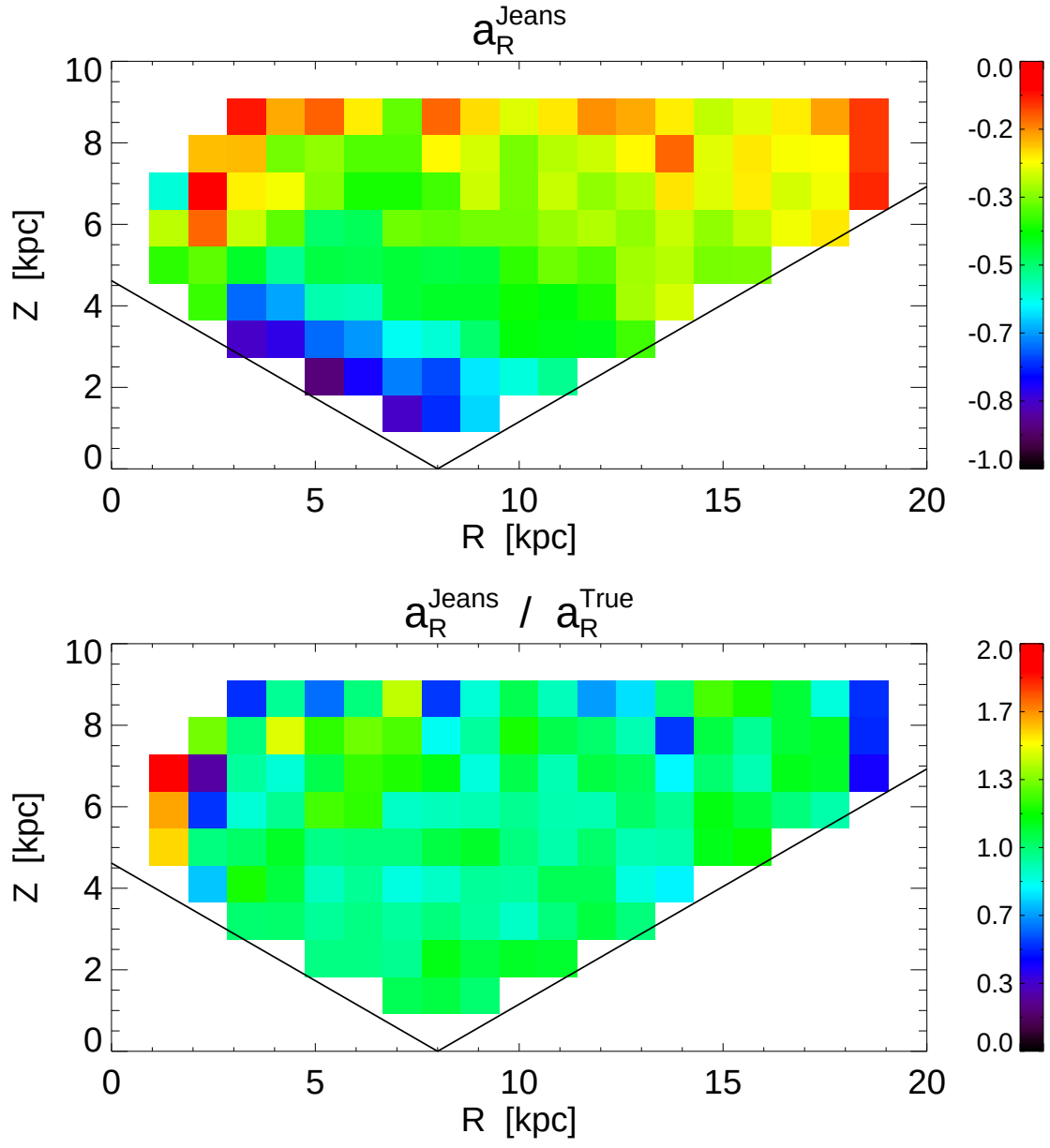

Figure 3.8 Analogous to Figure 3.7, except that the acceleration in the R direction, derived using Equation 3.1, is shown and expressed in units of 2.3×10^{-13} $\mathrm{km\,s^{-2}}$.

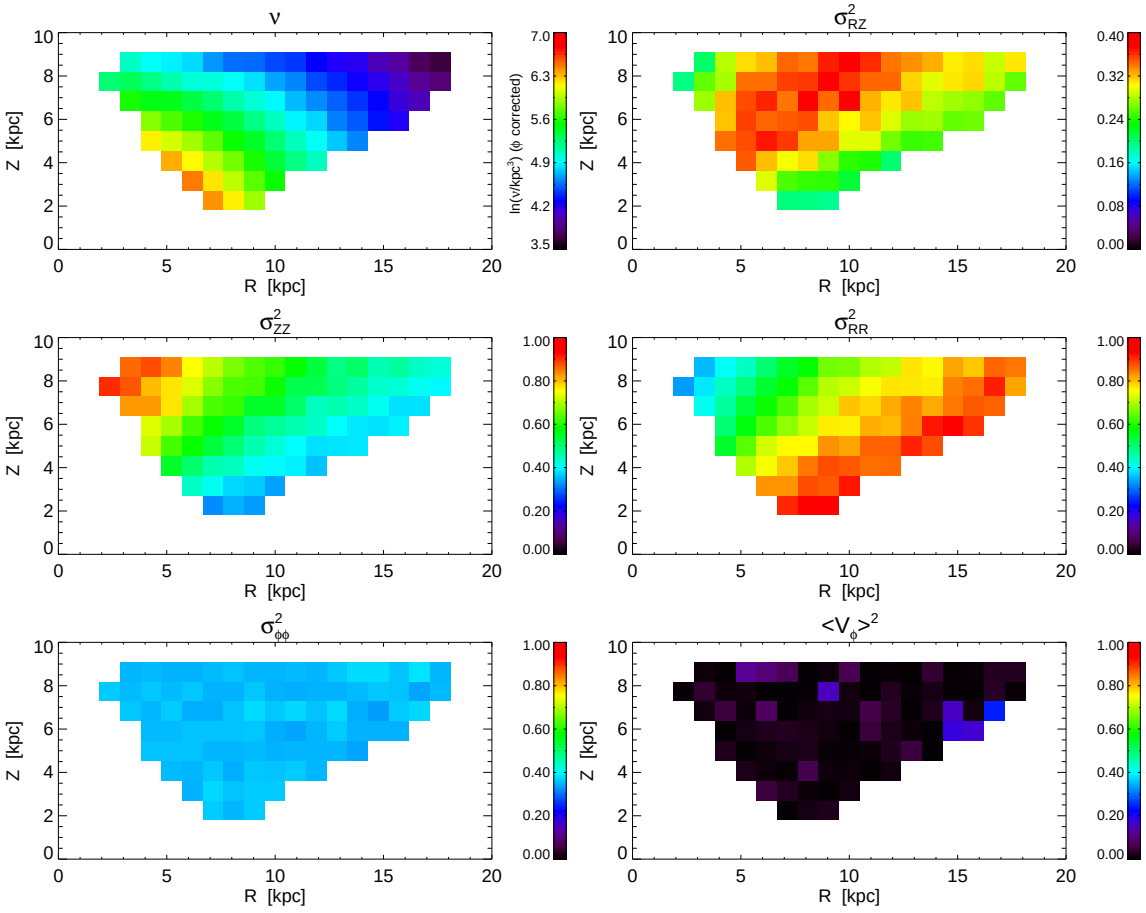

Figure 3.9 (Top left) Stellar number density map for halo stars in the SDSS footprint generated using *galfast*. This panel is logarithmically scaled, while all other panels are shown on a linear scale and re-normalized by 2×10^4 km^2 s^{-2} to enable comparison of relative contributions of terms from Equations 1 and 2 to accelerations a_Z and a_R. Each respective term is listed at the top of each panel.

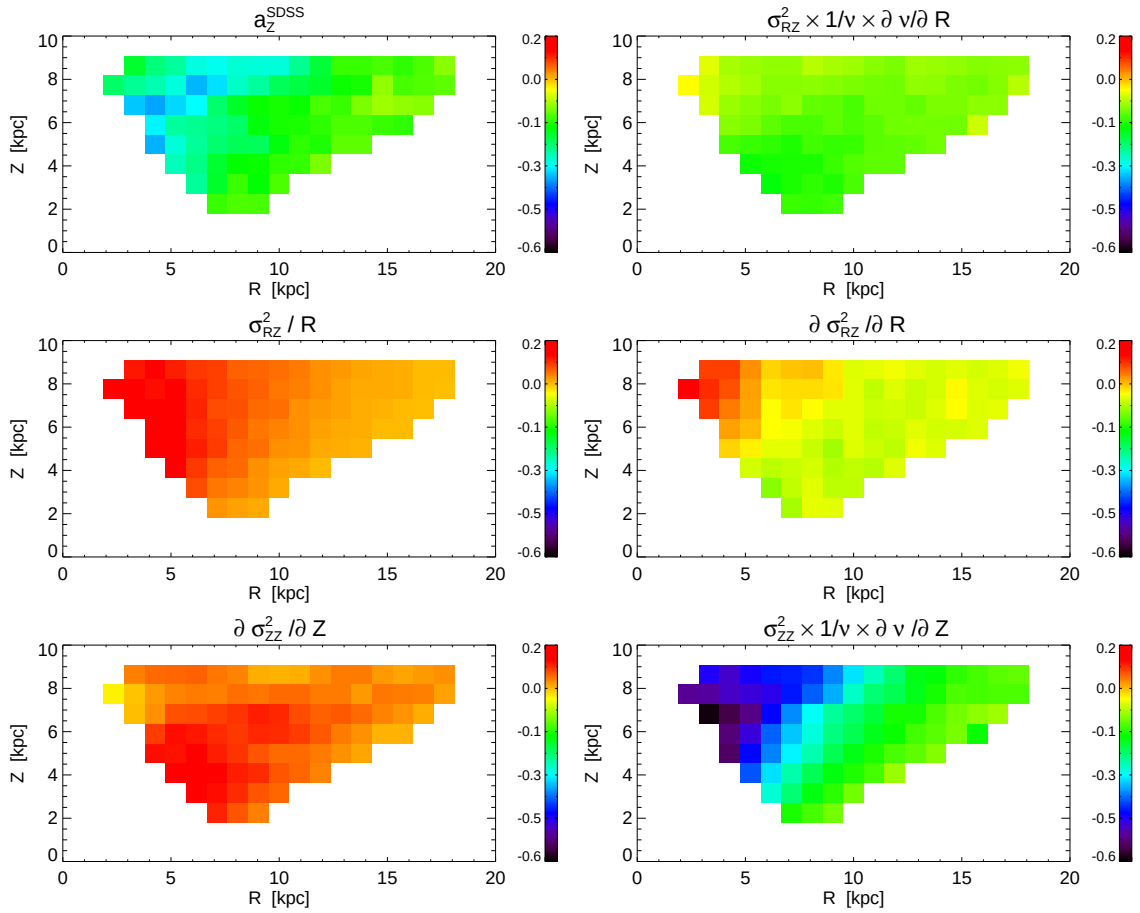

Figure 3.10 *Galfast* a_Z^{SDSS} map, expressed in units of 2.9×10^{-13} km s^{-2}, and its constituent terms from Equation 3.2. Note that the scale is the same in all panels for easy comparison. Terms are ordered clockwise from top right to middle left and add to equal a_Z^{SDSS}, shown in the top left panel. Each panel is labeled with the term it corresponds to.

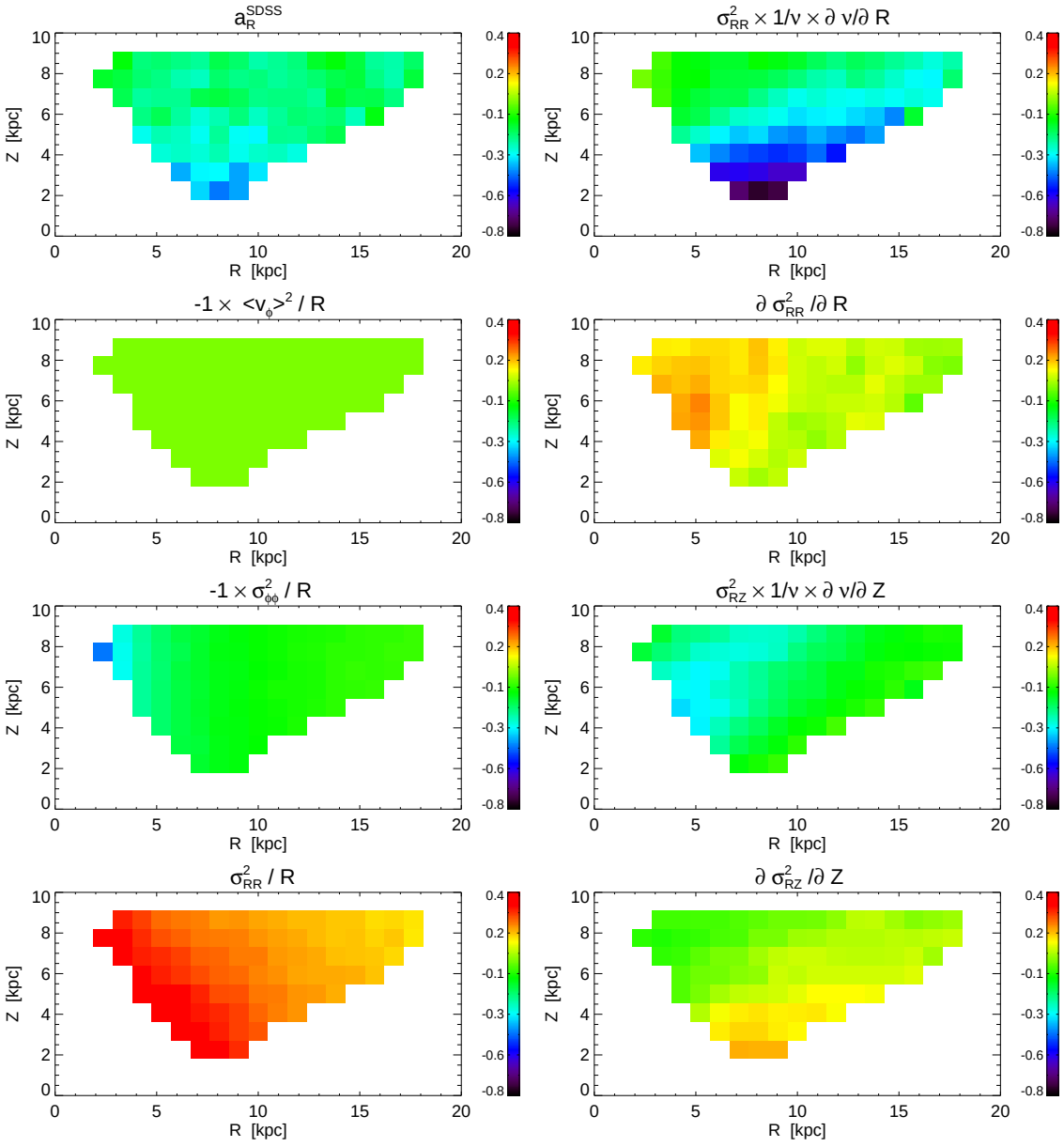

Figure 3.11 Analogous to Figure 3.10 but for a_R^{SDSS} and the constituent terms in Equation 3.1. Each panel is expressed in units of 2.3×10^{-13} km s^{-2}. The constituent terms are labeled and ordered clockwise from top right to upper-middle left and add to form a_R^{SDSS}, shown in the top left panel.

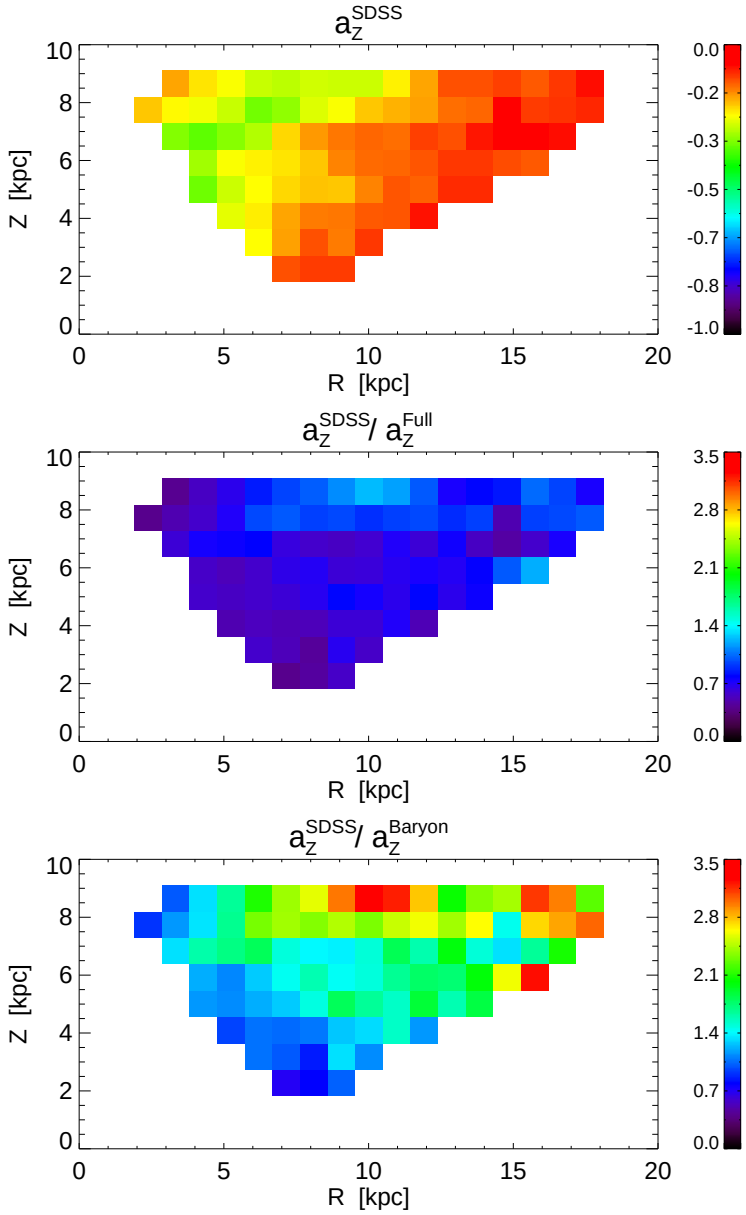

Figure 3.12 Results of applying Jeans Equations to the SDSS observations simulated using *galfast*. The top panel shows a map of acceleration in the Z direction expressed in units of 2.9×10^{-13} km s^{-2} (same as the top left panel in Figure 3.10, except for different scaling). The middle and bottom panels show the ratio of the map from the top panel and the two model-based maps shown in the top two panels in Figure 3.4.

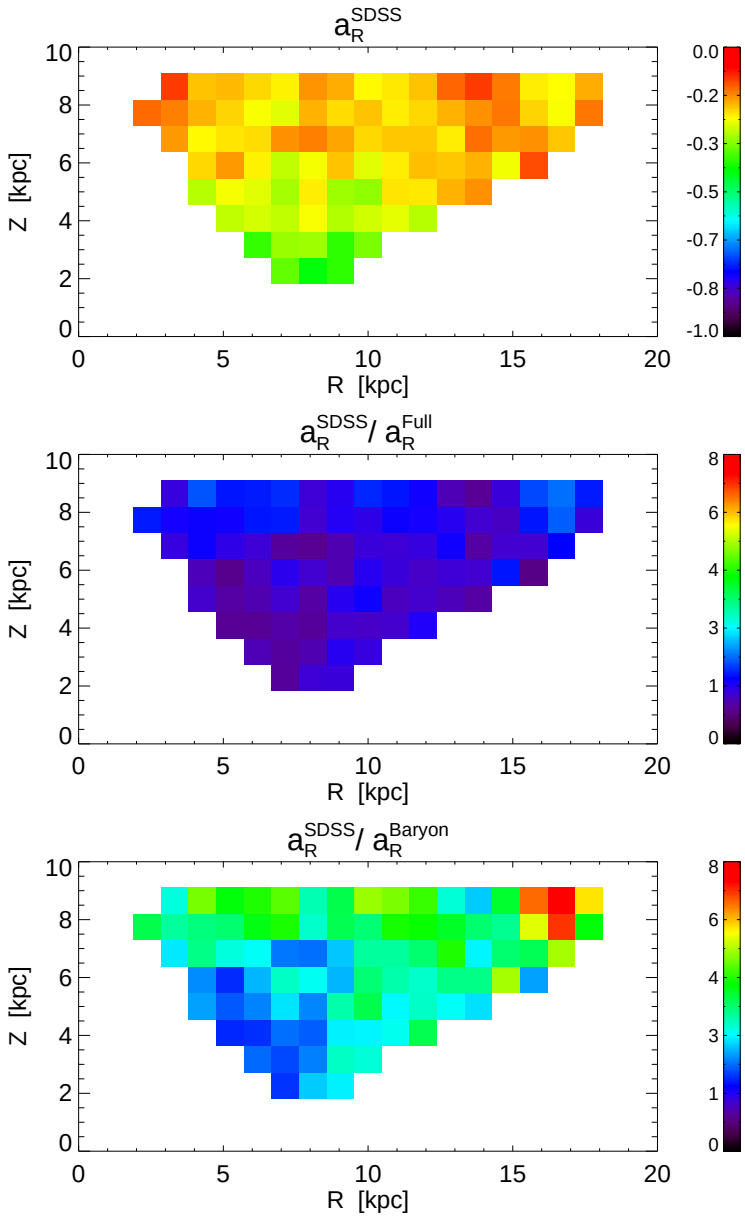

Figure 3.13 Analogous to Figure 3.12, but for the component of the acceleration in the R direction, expressed in units of 2.3×10^{-13} $\mathrm{km\,s^{-2}}$.

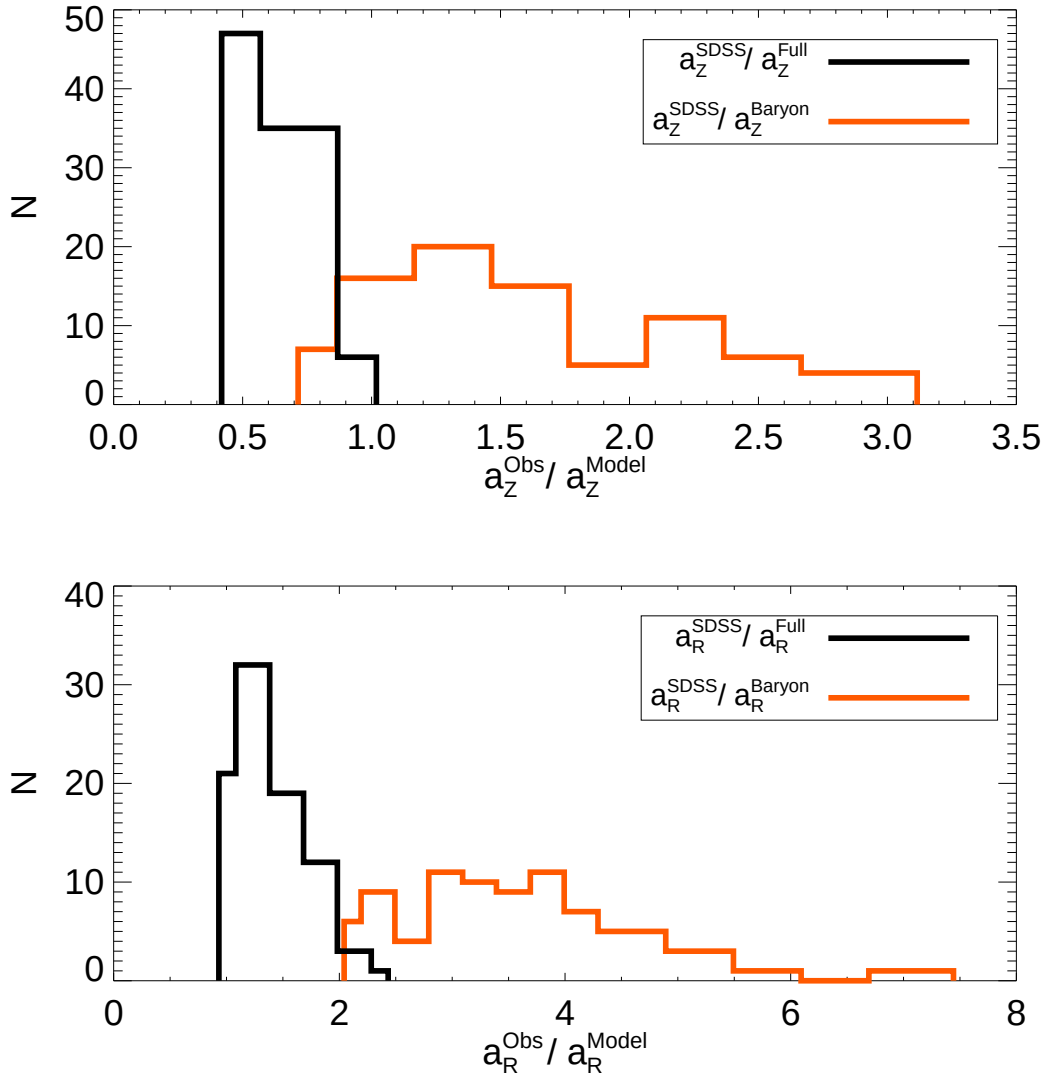

Figure 3.14 A pixel-by-pixel comparison of the acceleration values implied by SDSS data and the two model predictions that include (black lines) and do not include (orange lines) contributions from dark matter. The top panel corresponds to the a_Z^{SDSS} maps shown in Figure 3.12 and the bottom panel to a_R^{SDSS} acceleration maps shown in Figure 3.13. The model-based acceleration maps that include the dark matter contribution provide significantly better description of acceleration maps derived from SDSS data.

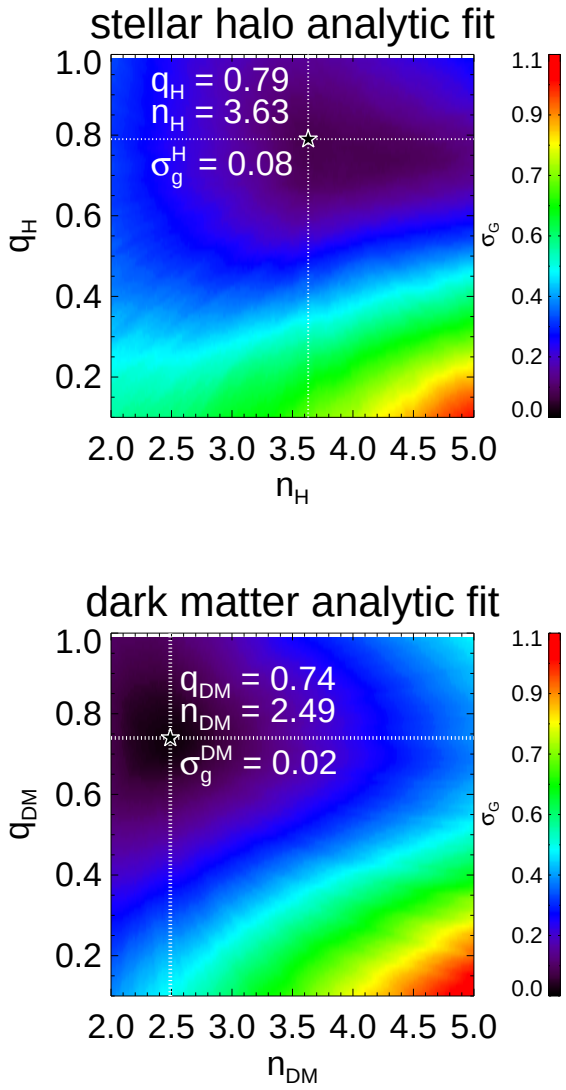

Figure 3.15 Determination of the best-fit parameters for the ellipsoidal power-law fits to distributions of stellar particles (top panel) and dark matter particles (bottom panel) in the adopted N–body simulation within 5.5 kpc $\leq r_{spherical} \leq$ 36.0 kpc. The plots show the scatter between measured and fitted values for a grid of power-law indices (n_H and n_{DM}) and major-to-minor axis ratios (q_H and q_{DM}) using robust estimator σ_G (the interquartile range normalized to correspond to standard deviation in the case of a Gaussian distribution). The best-fit parameters are $n_H = 3.63$, $q_H = 0.79$ and $n_{DM} = 2.49$, $q_{DM} = 0.74$ for the stellar and dark matter halo, respectively.

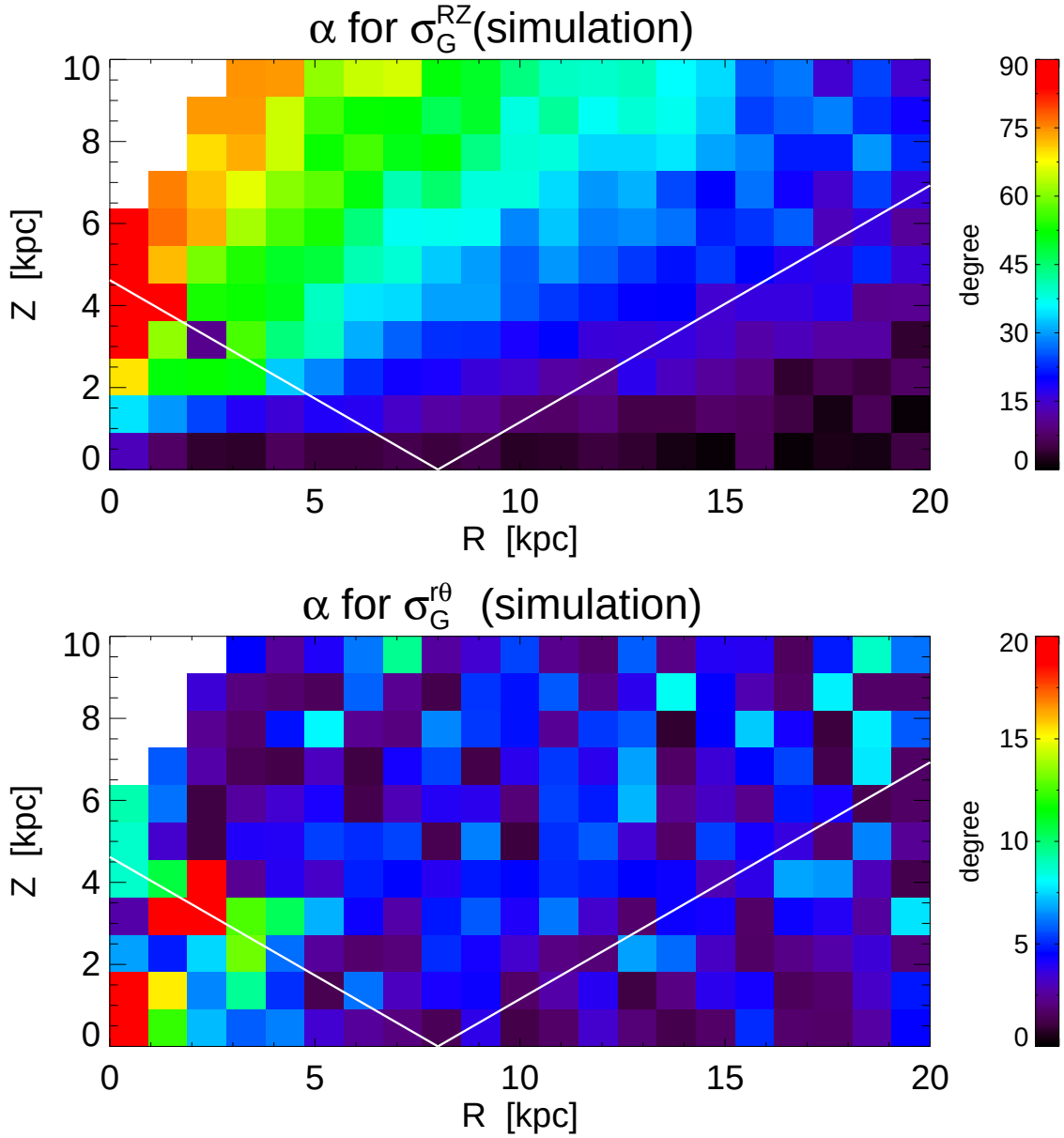

Figure 3.16 (Top): The angle α between the R axis and the semi-major axis of the velocity ellipsoid (V_R, V_Z) in cylindrical coordinates for stellar particles from N–body simulation. (Bottom): The angle α for (V_r, V_θ) distribution in spherical coordinate system. The α is small and varies little in spherical coordinate system, indicating the stellar halo velocity ellipsoid in N–body simulation is approximately aligned with a spherical coordinate system. The variation of angle α in cylindrical coordinate system is consistent with this conclusion.

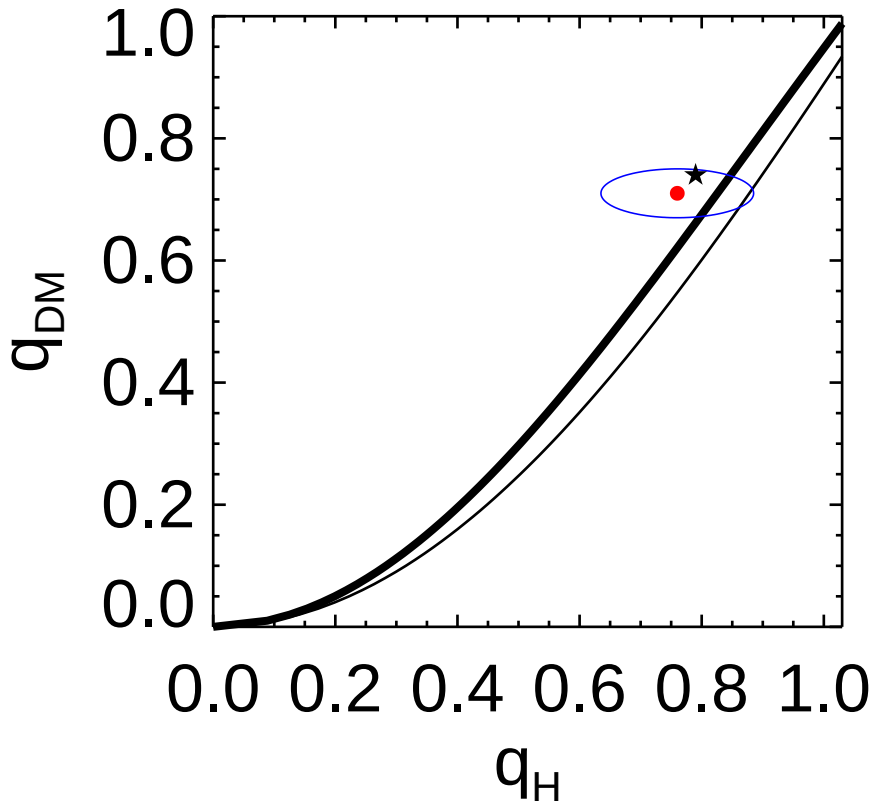

Figure 3.17 An analytic relationship derived by V91 between the stellar axis ratio, q_H, and the dark matter axis ratio, q_{DM}, for the N–body simulation. Thick and thin lines correspond to kinematics for an SDSS-like and full simulation volume, respectively. The blue ellipse encompasses the range of true axis ratios sampled in Figure 3.3. The red dot indicates the mean true axis ratios from Figure 3.3 ($<q>=$ 0.76, $<q_{DM}>=$ 0.71). The black star indicates the best-fit q from the power-law fits to the dark matter and stellar halo distributions (see Figure 3.15), $q_H = 0.74$ and $q_H = 0.79$ respectively. The implied uncertainty in q_{DM} due to deviations from assumed power law is below ∼0.1.

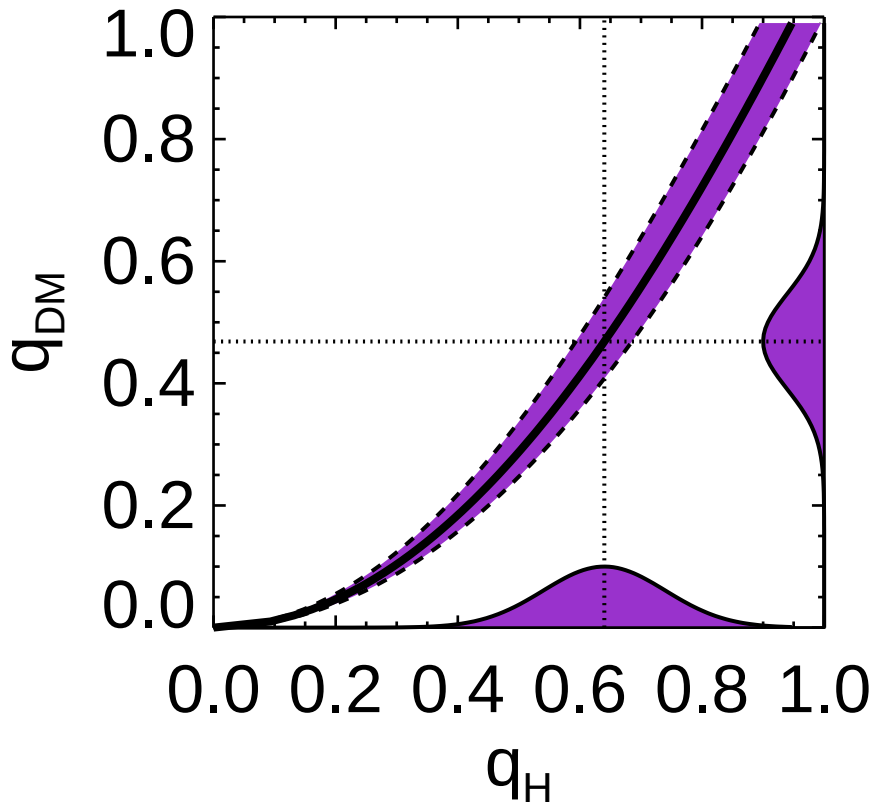

Figure 3.18 The analytic relationship between q_H, the axis ratio of the stellar metal-poor halo, and q_{DM}, the dark matter axis ratio, as predicted by van der Marel (1991) in the case when the velocity ellipsoid is aligned with a spherical coordinate system. The vertical dotted line at $q_H = 0.64$ indicates the most likely value of the axis ratio and its uncertainty ($\sigma = 0.1$, assuming Gaussian distribution), for the MW stellar halo from Jurić et al. (2008). The Gaussian on the y-axis shows the allowable q_{DM} given the error in q_H and the largest plausible error associated with the kinematic measurements. From this, we find $q_{DM} = 0.47 \pm 0.1$ within SDSS MW stellar volume. Per Figure 3.17, the systematic error of this estimate is $\sim$0.1

Chapter 4

CONCLUSION AND FUTURE WORK

I summarize here the main findings of this thesis and briefly overview a few more recent related results from the literature.

4.1 Properties of the Thin/Thick Disk System

In this thesis, I looked at structural, chemical and kinematic trends within the disk of an isolated N–body simulation. This simulation was evolved for 10 Gyr using GASOLINE (Wadsley et al., 2004) and contains significant radial migration; trends in this simulation were compared to the MW thin/thick disk system to assess, if, in the simplest of scenario, it is possible to build a physically reasonable thin/thick disk system purely from radial migration. Not only did the simulation produce realistically smooth gradients in kinematics and metallicities away from the plane of the disk within the solar cylinder, but it also reproduced reasonable scale heights and normalizations when fit by a double-component sech^2 model.

Moreover, this simulation succeeds where other models have failed in comparison to the MW: it replicates a lack of correlation between V_ϕ and $[Fe/H]$ in the so-called "transition zone." Within the simulation, this result was driven by the complex interplay between young stars on perigalactic and apogalactic passage and old stars that had experienced a range of migrating events that reassigned their rotational velocity over time.

Along with the work presented in this thesis, there is a rapidly growing body of work that considers the MW thin/thick disk system from a chemical standpoint. Of particular interest is whether α-enhancement should be used to segregate the disk. Moreover, does this segregation demonstrate that the thick disk is a distinct entity formed at an earlier epoch or is it still consistent with a continuously evolving system that is built up primarily through secular processes such as radial migration?

I demonstrated using an N–body simulation that if the disk is divided into two components based on a kinematic cut, the results show an artificial dichotomy in the other observables. With that caveat aside, I showed that when the disk is split using an $[\alpha/Fe]$ cut, it is a very good approximation to an age cut, particularly for the α-enhanced population; moreover, separating stars into very old and not-so-old components gives rise to all the observed correlations seen in the SDSS SEGUE sample (Lee et al., 2010).

4.2 Recent Observational Work on the Thin/Thick Disk System and Radial Migration

Recently, Bovy et al. (2012) used data from the SDSS SEGUE sample to decompose the MW stellar disk into mono-abundance sub-populations as defined in $[\alpha/Fe]$–$[Fe/H]$ space. Bovy et al. (2012) found that the mono-abundance sub-populations are well described by a single-exponential spatial-density profile in both the radial and vertical directions. They conclude the MW has a continuous and monotonic distribution of disk thicknesses rather than a distinct characteristic "thick disk" component; these findings agree with I08's interpretation of the SDSS data and are consistent with the theory that radial migration could have formed the disk system.

On the other hand, Haywood et al. (2013) recently analyzed 11,111 FGK stars from the Adibekyan et al. (2012) solar neighborhood sample and found that based on trends of $[\alpha/Fe]$ and $[Fe/H]$ *vs.* age, radial migration was not the significant mechanism for the creation of the thick and thin disks. Haywood et al. (2013) show there are two distinct regimes of $[\alpha/Fe]$ *vs.* age, which they identify as the epochs of the thick and thin disk formation. They conclude that their data leaves little room for radial migration, either to have contaminated the solar vicinity, or, on a larger scale, to have redistributed stars in significant proportion across the solar annulus.

Still yet another contrasting view about the plausibility of radial migration in the solar neighborhood is presented by Adibekyan et al. (2013), who use the same data as Haywood et al. (2013), but suggest that high α metal rich stars in their sample could most plausible have formed in the inner disk or bulge. They point to results presented in this thesis and Roškar et al. (2013) that show a similar population of stars in the simulated solar

neighborhood arrived there through radial migration.

Therefore, there is still an active and vigorous ongoing debate whether a definitive signature of radial migration exists in the thin/thick disk system.

4.3 The Galactic Dark Matter Halo in Simulations & Observations

In this thesis, I also searched for evidence of dark matter within the SDSS stellar halo by utilizing Jeans equations. Jeans equations provide a means to access the gravitational potential through a statistical estimation of acceleration. Jeans equations utilize the number density distribution and kinematics of stars to produce the gradient of the gravitational potential (*i.e.* the mean acceleration).

Within this thesis, I presented a detailed description of the application of Jeans equations to a cosmologically derived N–body+SPH simulation of a Milky Way-like galaxy. I was able to recover the true accelerations tracked by the simulation through my application of Jeans equations; this recovery was significant because, like the MW, the simulation does not strictly adhere to the criteria in which Jeans equations were derived (*i.e.* the simulation is neither perfectly axisymmetric nor steady-state). I also used the N–body simulation to quantify the relative contributions of visible and dark matter to the total acceleration for a synthetic SDSS volume within the simulation. My analysis revealed that the relative contribution of dark matter to the total acceleration is quite significant, particular in regions away from the bulge and plane of the disk.

I applied the same Jeans equation machinery tested on the cosmologically derived N–body simulation to halo stars measured by SDSS to heliocentric distances exceeding 10 kpc and galactocentric distances of 20 kpc. My analysis produced large two-dimensional acceleration maps; I compared these maps to maps drawn from the N–body simulation to assess if dark matter is necessary to produce the observed acceleration morphology. The stellar acceleration maps constructed using Jeans equations and SDSS-based observational constraints revealed that, in a Newtonian framework, the implied gravitational potential cannot be explained by visible matter alone: the gravitational force experienced by stars at galactocentric distances of 20 kpc is as much as three times larger than what can be attributed to visible matter alone.

I also utilized an analytic method developed using Jeans equations and the alignment of the velocity ellipsoid to estimate the MW dark matter halo axis ratio. I first tested this technique on the N–body model and found it successfully recovered the mean dark matter axis ratio within a synthetic SDSS volume. I then applied this technique to the true SDSS stellar halo data and found it implied an oblate halo with axis ratio $q_{DM} = 0.47 \pm 0.14$ (here errors are statistical errors without systematic effects) within the same distance range.

4.4 Future Work

4.4.1 Thick Disks and Radial Migration

I hope to continue to collaborate with Branimar Sesar, Victor Debattista and Rok Roškar to consider what kind of selection bias (if any) can produce the Haywood et al. (2013) results if the disk grows through radial migration.

4.4.2 Constraining the Galactic Potential at a Range of Galactic Radii

The Jeans equation techniques I applied within my thesis can be used to map the dark matter halo with a much better fidelity with Gaia, and to much larger galactocentric distances with upcoming deep optical surveys, such as LSST.

4.4.2.1 Measuring halo shape at small radii with Jeans equations & Schwarzschild modeling.

I will extend my previous work applying Jeans equations to mock SDSS volumes for a suite of cosmologically derived MW–like galaxies. In collaboration with Monica Valluri (U. Michigan), I will use Schwarzschild orbit superposition method (Schwarzschild, 1979) to derive an alternative measurement of the flattening of the dark matter halo's density profile within the same volume.

4.4.2.2 Measuring halo shape at large radii with satellites and tidal debris

The orbits of satellite populations and the existence of tidal debris contain important global information about their host potential. Following the techniques used by Johnston et al.

(1999), Sanders & Binney (2013), and Watkins et al. (2010), I will apply distance, radial velocity and proper motion data from subhalos and stellar streams in the simulations to constrain the halo extent, mass and velocity anisotropy.

BIBLIOGRAPHY

Abadi, M. G., Navarro, J. F., Steinmetz, M., & Eke, V. R. 2003, Astroph. J., 597, 21

Abe, F. et al. 1999, Astron. J., 118, 261

Adibekyan, V. Z., Delgado Mena, E., Sousa, S. G., Santos, N. C., Israelian, G., González Hernández, J. I., Mayor, M., & Hakobyan, A. A. 2012, A&A, 547, A36

Adibekyan, V. Z. et al. 2013, A&A, 554, A44

Allende Prieto, C., Barklem, P. S., Lambert, D. L., & Cunha, K. 2004, VizieR Online Data Catalog, 342, 183

Bahcall, J. N. 1984, Astroph. J., 276, 169

Bahcall, J. N., & Soneira, R. M. 1980, ApJ, 238, L17

Banerjee, A., & Jog, C. J. 2011, ApJ, 732, L8

Battaglia, G., et al. 2005, MNRAS, 364, 433

Bensby, T., Feltzing, S., & Lundström, I. 2003, A&A, 410, 527

Bensby, T., Feltzing, S., Lundström, I., & Ilyin, I. 2005, A&A, 433, 185

Binney, J. 2010, MNRAS, 401, 2318

Binney, J., & Tremaine, S. 1987, Galactic dynamics

Blumenthal, G. R., Faber, S. M., Flores, R., & Primack, J. R. 1986, Astroph. J., 301, 27

Bochanski, J. J., Munn, J. A., Hawley, S. L., West, A. A., Covey, K. R., & Schneider, D. P. 2007, Astron. J., 134, 2418

Bond, N. A. et al. 2010, Astroph. J., 716, 1

Bournaud, F., Elmegreen, B. G., & Martig, M. 2009, ApJ, 707, L1

Bovy, J., Rix, H.-W., & Hogg, D. W. 2012, Astroph. J., 751, 131

Bovy, J., & Tremaine, S. 2012, ArXiv e-prints, 1205.4033

Boylan-Kolchin, M., Besla, G., & Hernquist, L. 2011, MNRAS, 414, 1560

Brewer, M. M. 2004, PhD thesis, The University of North Carolina at Chapel Hill

Brook, C. B., Gibson, B. K., Martel, H., & Kawata, D. 2005, Astroph. J., 630, 298

Brook, C. B., Kawata, D., Gibson, B. K., & Freeman, K. C. 2004, Astroph. J., 612, 894

Brooks, A. M. et al. 2011, Astroph. J., 728, 51

Brown, W. R., Geller, M. J., Kenyon, S. J., & Diaferio, A. 2010, Astron. J., 139, 59

Bullock, J. S., Dekel, A., Kolatt, T. S., Kravtsov, A. V., Klypin, A. A., Porciani, C., & Primack, J. R. 2001, Astroph. J., 555, 240

Bullock, J. S., & Johnston, K. V. 2005, Astroph. J., 635, 931

Burstein, D. 1979, Astroph. J., 234, 829

Buser, R., Rong, J., & Karaali, S. 1999, A&A, 348, 98

Carollo, D. et al. 2010, Astroph. J., 712, 692

Caruana, J. 2009, Dissertation bsc (hons), Department of Physics, University of Malta

Chen, B. et al. 2001, Astroph. J., 553, 184

Chiba, M., & Beers, T. C. 2000, Astron. J., 119, 2843

Christensen, C., Quinn, T., Governato, F., Stilp, A., Shen, S., & Wadsley, J. 2012, ArXiv e-prints, 1205.5567

Cooper, A. P., Cole, S., Frenk, C. S., & Helmi, A. 2011, MNRAS, 1440

Creze, M., Chereul, E., Bienayme, O., & Pichon, C. 1998, A&A, 329, 920

Deason, A. J., Belokurov, V., & Evans, N. W. 2011, MNRAS, 416, 2903

Debattista, V. P., Moore, B., Quinn, T., Kazantzidis, S., Maas, R., Mayer, L., Read, J., & Stadel, J. 2008, Astroph. J., 681, 1076

Debattista, V. P., Roskar, R., Valluri, M., Quinn, T., Moore, B., & Wadsley, J. 2013, ArXiv e-prints

Di Matteo, P., Lehnert, M. D., Qu, Y., & van Driel, W. 2011, A&A, 525, L3+

Dierickx, M., Klement, R. J., Rix, H., & Liu, C. 2010, ArXiv e-prints, 1009.1616

Feltzing, S. 2006, Memorie della Societa Astronomica Italiana, 77, 1103

Feltzing, S., Bensby, T., & Lundström, I. 2003, A&A, 397, L1

Fuhrmann, K. 1998, A&A, 338, 161

Garbari, S., Liu, C., Read, J. I., & Lake, G. 2012, ArXiv e-prints, 1206.0015

Gilmore, G., & Reid, N. 1983, MNRAS, 202, 1025

Gilmore, G., Wyse, R. F. G., & Norris, J. E. 2002, ApJ, 574, L39

Governato, F. et al. 2009, MNRAS, 398, 312

—. 2012, MNRAS, 422, 1231

Gustafsson, M., Fairbairn, M., & Sommer-Larsen, J. 2006, Phys. Rev. D, 74, 123522

Haywood, M. 2008, MNRAS, 388, 1175

Haywood, M., Di Matteo, P., Lehnert, M., Katz, D., & Gomez, A. 2013, ArXiv e-prints

Helmi, A. 2004, ApJ, 610, L97

Hoffman, R. D., Woosley, S. E., Weaver, T. A., Rauscher, T., & Thielemann, F. 1999, Astroph. J., 521, 735

Holmberg, J., & Flynn, C. 2000, MNRAS, 313, 209

—. 2004, MNRAS, 352, 440

Holmberg, J., Nordström, B., & Andersen, J. 2009, A&A, 501, 941

Ibata, R., Lewis, G. F., Irwin, M., Totten, E., & Quinn, T. 2001, Astroph. J., 551, 294

Ivezić, Ž., Beers, T. C., & Jurić, M. 2012, ARA&A, 50, 251

Ivezić, Ž. et al. 2008a, Astroph. J., 684, 287

Ivezić, Ž., Tyson, J. A., Acosta, E., et al. 2008b, ArXiv e-prints, 0805.2366

Jeans, J. H. 1915, MNRAS, 76, 70

Johnston, K. V., Zhao, H., Spergel, D. N., & Hernquist, L. 1999, ApJ, 512, L109

Jones, B. J. T., & Wyse, R. F. G. 1983, A&A, 120, 165

Jonsson, P. 2006, MNRAS, 372, 2

Jurić, M. et al. 2008, Astroph. J., 673, 864

Kapteyn, J. C. 1922, Astroph. J., 55, 302

Katz, N. 1991, Astroph. J., 368, 325

Katz, N., & White, S. D. M. 1993, Astroph. J., 412, 455

Kaufmann, T., Mayer, L., Wadsley, J., Stadel, J., & Moore, B. 2007, MNRAS, 375, 53

Kazantzidis, S., Bullock, J. S., Zentner, A. R., Kravtsov, A. V., & Moustakas, L. A. 2008, Astroph. J., 688, 254

Keller, S. C., Murphy, S., Prior, S., Da Costa, G., & Schmidt, B. 2008, Astroph. J., 678, 851

Klypin, A., Zhao, H., & Somerville, R. S. 2002, Astroph. J., 573, 597

Kuijken, K., & Gilmore, G. 1989, MNRAS, 239, 651

—. 1991, ApJ, 367, L9

Larsen, J. A., & Humphreys, R. M. 2003, Astron. J., 125, 1958

Law, D. R., & Majewski, S. R. 2010, Astroph. J., 714, 229

Lee, Y. S. et al. 2010, in Bulletin of the American Astronomical Society, Vol. 41, Bulletin of the American Astronomical Society, 250–+

Linnaeus, C. 1735, Systema naturae

Loebman, S. et al. 2008, American Institute of Physics Conference Series, 1082, 238

Loebman, S. R., Ivezić, Ž., Quinn, T. R., Governato, F., Brooks, A. M., Christensen, C. R., & Jurić, M. 2012, ApJ, 758, L23

Loebman, S. R., Roškar, R., Debattista, V. P., Ivezić, Ž., Quinn, T. R., & Wadsley, J. 2011, Astroph. J., 737, 8

Lux, H., Read, J. I., Lake, G., & Johnston, K. V. 2012, MNRAS, 424, L16

Majewski, S. R. 1993, ARA&A, 31, 575

Majewski, S. R., Wilson, J. C., Hearty, F., Schiavon, R. R., & Skrutskie, M. F. 2010, in IAU Symposium, Vol. 265, IAU Symposium, ed. K. Cunha, M. Spite, & B. Barbuy, 480–481

Markevitch, M., Gonzalez, A. H., Clowe, D., Vikhlinin, A., Forman, W., Jones, C., Murray, S., & Tucker, W. 2004, Astroph. J., 606, 819

Minchev, I., & Famaey, B. 2010, Astroph. J., 722, 112

Mishenina, T. V., Soubiran, C., Kovtyukh, V. V., & Korotin, S. A. 2004, A&A, 418, 551

Moni Bidin, C., Carraro, G., Mendez, R. A., & Smith, R. 2012, ArXiv e-prints, 1204.3919

Munn, J. A. et al. 2004, Astron. J., 127, 3034

Navarro, J. F., Abadi, M. G., Venn, K. A., & Freeman, K. C. 2010, ArXiv e-prints, 1009.0020

Navarro, J. F., Frenk, C. S., & White, S. D. M. 1997, Astroph. J., 490, 493

Neeser, M. J., Sackett, P. D., De Marchi, G., & Paresce, F. 2002, A&A, 383, 472

Nissen, P. E. 1995, in IAU Symposium, Vol. 164, Stellar Populations, ed. P. C. van der Kruit & G. Gilmore, 109–+

Nissen, P. E., & Schuster, W. J. 2009, in IAU Symposium, Vol. 254, IAU Symposium, ed. J. Andersen, J. Bland-Hawthorn, & B. Nordström, 103–108

Norris, J. E. 1999, Ap&SS, 265, 213

Ojha, D. K. 2001, MNRAS, 322, 426

Oort, J. H. 1932, Bull. Astron. Inst. Netherlands, 6, 249

—. 1960, Bull. Astron. Inst. Netherlands, 15, 45

Parker, J. E., Humphreys, R. M., & Beers, T. C. 2004, Astron. J., 127, 1567

Perryman, M. A. C. 2002, Ap&SS, 280, 1

Pontzen, A. et al. 2008, MNRAS, 390, 1349

Power, C., Navarro, J. F., Jenkins, A., Frenk, C. S., White, S. D. M., Springel, V., Stadel, J., & Quinn, T. 2003, MNRAS, 338, 14

Prochaska, J. X., Naumov, S. O., Carney, B. W., McWilliam, A., & Wolfe, A. M. 2000, Astron. J., 120, 2513

Quinn, P. J., Hernquist, L., & Fullagar, D. P. 1993, Astroph. J., 403, 74

Raiteri, C. M., Villata, M., Gallino, R., Busso, M., & Cravanzola, A. 1999, ApJ, 518, L91

Reddy, B. E., Lambert, D. L., & Allende Prieto, C. 2006, MNRAS, 367, 1329

Reddy, B. E., Tomkin, J., Lambert, D. L., & Allende Prieto, C. 2003, MNRAS, 340, 304

Robin, A. C., Haywood, M., Creze, M., Ojha, D. K., & Bienayme, O. 1996, A&A, 305, 125

Rockosi, C., Beers, T. C., Majewski, S., Schiavon, R., & Eisenstein, D. 2009, in Astronomy, Vol. 2010, astro2010: The Astronomy and Astrophysics Decadal Survey, 14–+

Roškar, R., Debattista, V. P., Brooks, A. M., Quinn, T. R., Brook, C. B., Governato, F., Dalcanton, J. J., & Wadsley, J. 2010, MNRAS, 408, 783

Roškar, R., Debattista, V. P., & Loebman, S. R. 2013, MNRAS

Roškar, R., Debattista, V. P., Quinn, T. R., Stinson, G. S., & Wadsley, J. 2008a, ApJ, 684, L79

Roškar, R., Debattista, V. P., Stinson, G. S., Quinn, T. R., Kaufmann, T., & Wadsley, J. 2008b, ApJ, 675, L65

Rubin, V. C., Ford, W. K. J., & . Thonnard, N. 1980, Astroph. J., 238, 471

Ruchti, G. R. et al. 2010, ArXiv e-prints, 1008.3828

Sales, L. V. et al. 2009, MNRAS, 400, L61

Samurović, S., & Lalović, A. 2011, A&A, 531, A82

Sanders, J. L., & Binney, J. 2013, MNRAS

Scannapieco, C. et al. 2012, MNRAS, 423, 1726

Schlaufman, K. C. et al. 2009, Astroph. J., 703, 2177

Schlaufman, K. C., Rockosi, C. M., Lee, Y. S., Beers, T. C., & Allende Prieto, C. 2011, Astroph. J., 734, 49

Schönrich, R., & Binney, J. 2009a, MNRAS, 396, 203

—. 2009b, MNRAS, 399, 1145

Schönrich, R. A. 2010, Highlights of Astronomy, 15, 185

Schwarzschild, M. 1979, Astroph. J., 232, 236

Sellwood, J. A., & Binney, J. J. 2002, MNRAS, 336, 785

Sesar, B. et al. 2010, Astroph. J., 708, 717

Sesar, B., Ivezić, Ž., & Jurić, M. 2008, Astroph. J., 689, 1244

Sesar, B., Jurić, M., & Ivezić, Ž. 2011, Astroph. J., 731, 4

Shen, S., Wadsley, J., & Stinson, G. 2009, ArXiv e-prints, 0910.5956

Siebert, A., Bienaymé, O., & Soubiran, C. 2003, A&A, 399, 531

Siegel, M. H., Majewski, S. R., Reid, I. N., & Thompson, I. B. 2002, Astroph. J., 578, 151

Smagorinsky, J. 1963, Monthly Weather Review, 91, 99

Smith, M. C., Whiteoak, S. H., & Evans, N. W. 2012, Astroph. J., 746, 181

Soubiran, C., Bienaymé, O., & Siebert, A. 2003, A&A, 398, 141

Spagna, A., Lattanzi, M. G., Re Fiorentin, P., & Smart, R. L. 2010, A&A, 510, L4+

Spergel, D. N. et al. 2003, Astroph. J. Suppl., 148, 175

Spitzer, Jr., L. 1942, Astroph. J., 95, 329

Statler, T. S. 1988, Astroph. J., 331, 71

Steinmetz, M. et al. 2006, Astron. J., 132, 1645

Stinson, G., Seth, A., Katz, N., Wadsley, J., Governato, F., & Quinn, T. 2006, MNRAS, 373, 1074

Tautvaišienė, G., Edvardsson, B., Tuominen, I., & Ilyin, I. 2001, A&A, 380, 578

Tremaine, S., & Gunn, J. E. 1979, Physical Review Letters, 42, 407

Valluri, M., Debattista, V. P., Quinn, T. R., Roškar, R., & Wadsley, J. 2012, MNRAS, 419, 1951

van der Kruit, P. C., & Searle, L. 1981, A&A, 95, 105

van der Marel, R. P. 1991, MNRAS, 248, 515

Villalobos, Á., & Helmi, A. 2008, MNRAS, 391, 1806

Villalobos, Á., Kazantzidis, S., & Helmi, A. 2010, Astroph. J., 718, 314

Wadsley, J. W., Stadel, J., & Quinn, T. 2004, New Astronomy, 9, 137

Wadsley, J. W., Veeravalli, G., & Couchman, H. M. P. 2008, MNRAS, 387, 427

Watkins, L. L., Evans, N. W., & An, J. H. 2010, MNRAS, 406, 264

Watkins, L. L. et al. 2009, MNRAS, 398, 1757

Wilson, M. et al. 2010, ArXiv e-prints, 1009.2052

Wyse, R. F. G., Gilmore, G., Norris, J. E., Wilkinson, M. I., Kleyna, J. T., Koch, A., Evans, N. W., & Grebel, E. K. 2006, ApJ, 639, L13

Xue, X. X. et al. 2008, Astroph. J., 684, 1143

Yoachim, P. 2007, PhD thesis, University of Washington

Yoachim, P., & Dalcanton, J. J. 2005, Astroph. J., 624, 701

—. 2006, Astron. J., 131, 226

York, D. G., et al. 2000, Astron. J., 120, 1579

Zolotov, A., Willman, B., Brooks, A. M., Governato, F., Brook, C. B., Hogg, D. W., Quinn, T., & Stinson, G. 2009, Astroph. J., 702, 1058

VITA

Sarah Loebman completed her undergraduate studies in Asian Studies at Cornell University in 2001. Subsequently, she participated in Americorps VISTA and taught in the Bay Area for two years before deciding to pursue an advanced degree. Sarah conducted research in Astronomy at University of California, Santa Barbara under the supervision of Professors Philip Lubin and Crystal Martin from 2004-2006. Sarah began graduate studies in Astronomy at University of Washington in 2006. During her time there, Sarah participated extensively in educational outreach through her work with the Pre-Major in Astronomy Program (Pre-MAP) and Astronomy for the Sight Impaired (ASI) Project. Sarah's main scientific research at UW was conducted with the N–body shop and Željko Ivezić; through this experience she learned to grapple with a huge amount of real and fake data. To learn better ways to manage her data needs, Sarah spent significant time collaborating with Jeff Gardner and the CSE Database Group to investigate how existing and emerging database technology could be applied in the astrophysical domain. Sarah is deeply interested in the collaborative process and how it pertains to Big Data analysis; she hopes to grow her cross-disciplinary collaborations in the years to come. Sarah completed her doctorate at the University of Washington in 2013.